Proceedings of:

Control of Precisions Systems

2001 Spring Topical Meeting

April 18-20, 2001
Sheraton Rittenhouse Square Hotel
Philadelphia, Pennsylvania

The American Society for Precision Engineering (ASPE) is a multidisciplinary professional and technical society concerned with research and development, design, manufacture and measurement of high accuracy components and systems. ASPE activities encompass relevant aspects of mechanical, electronic, optical and production engineering, physics, chemistry, and computer and materials science. Membership is open to anyone interested in any aspect of precision engineering.

Founded in 1986, ASPE provides a new focus for a diverse but important community. Other professional organizations have covered aspects of precision engineering, always as a sideline to their principal goals. ASPE is based on the core of generic concepts necessary to achieve precision in any application; independent of discipline, ASPE intends to be the focus for precision technology — and to represent all facets from research to application.

ASPE — The American Society for Precision Engineering
301 Glenwood Avenue, Suite 205, Raleigh, NC 27603
P.O. Box 10826, Raleigh, NC 27605
Telephone: (919) 839-8444 Fax (919) 839-8039
Web site: http://www.aspe.net

Preface

This book comprises the proceedings of the 2001 Spring Topical Meeting. The contributions reflect the authors' opinions and are published as presented to ASPE, without change. Their inclusion in this publication does not necessarily constitute endorsement by the ASPE, or its editorial staff.

Individual readers of this book and nonprofit libraries acting for them are permitted to make fair use of the material contained in this book to be used in teaching or research; provided they copy said paper in total, as written by the author. Permission is granted to quote excerpts from the scientific or technical works in this book with proper acknowledgment of the source to include: The author's name, the book name, and the ASPE tag line. Reproduction of figures and tables is likewise permitted from the contents of this book, provided that the same acknowledgment of the same source and content is permitted.

Any other type reproduction, systematic copying or multiple reproduction of any material in this book is expressly prohibited except with the written permission of the ASPE editorial staff, addressed to the Society's headquarters.

ISBN 1-887706-25-9

2001

American Society for Precision Engineering
301 Glenwood Avenue, Suite 205
Raleigh, NC 27603

Printed in the United States of America

2001 Spring Topical Meeting

Contents

Preface ii

Contents iii

Program iv

Foreword v

Technical Paper Index. vi

Technical Papers 3-97

Author Index 99

2001 Spring Topical Meeting

Meeting Schedule

Tuesday, April 17		Wednesday, April 18	Thursday, April 19	Friday, April 20
	8:00	REGISTRATION AND CONTINENTAL BREAKFAST		
	9:00	TECHNICAL SESSION I	TECHNICAL SESSION IV	TECHNICAL SESSION VII
	10:30	BREAK		
	11:00	TECHNICAL SESSION II	TECHNICAL SESSION V	TECHNICAL SESSION VIII
	12:00	LUNCH ON YOUR OWN		
	2:30	TECHNICAL SESSION III	TECHNICAL SESSION VI	
	4:00			
ON-SITE REGISTRATION	4:30	RECEPTION	RECEPTION	
	6:00			
	6:30			

Foreword

The meeting will focus on new developments in feedback as applied to precision systems. We also encourage presentations of a tutorial nature that elaborate principles essential to achieving high performance in precision control systems.

The control of precision systems encompasses a wide range of applications such as motion generation in semiconductor processing and precision machining, e-beam and optical scanning systems, data storage and transmission devices, microscopy, micro-devices, high-resolution sensors, and low-noise electronics. The performance of such instruments, devices, and processes depends intimately upon the innovative application of feedback principles due to the large dynamic range of controlled variables and the sensitivity to effects that might be ignorable in conventional systems.

This conference is intended to promote a broader understanding of the principles and techniques applicable for precision control, to highlight the challenges and achievements unique to our field, to bring together specialists and practitioners from industry, government and academia for the exchange of ideas, and to identify topics for further research.

Chairmen of the 2001 Spring Topical Meeting

Andrew J. Hazelton, *Nikon Research Corporation of America*
David L. Trumper, *Massachusetts Institute of Technology*

2001 Spring Topical Meeting Scholarship Recipients

Corwin T. Hardham, *Stanford University*
Stefan Rakuff, *University of North Carolina at Charlotte*

Technical Paper Index

Session I

Wednesday, April 18, 9:00 a.m. - 10:30 a.m.

Opening Remarks

1. ***Tachometers, Do We Need Them?***
   D. B. DeBra (Stanford University) . . . . . page 3
2. ***Controller Requirements for High-precision Motion Applications***
   C. S. Wilson (Delta Tau Data Systems, Inc.) . . . . . page 9
3. ***Sinusoidal Velocity Profiles for Motion Control***
   V. M. Arelavo (Augen Opticos, S.A.) . . . . . page 13

Session II

Wednesday, April 18, 11:00 a.m. - 12:00 p.m.

1. ***Enhancing Precision Manufacturing Through In-Situ Metrology***
   S. C. Woody, S. T. Smith (University of North Carolina at Charlotte) . . . . . page 17
2. ***Control of a Dynamic Flex-stage***
   P-H. Yang, B. J. Alamo, J. McCoy, G. B. Andeen (Ion Diagnostics, Inc.) . . . . . page 23

Session III

Wednesday, April 18, 2:30 p.m. - 4:00 p.m.

1. ***Dynamics of a High Performance Workpiece Table for Active Control During Precision Grinding***
   Y. Gao, D. Zhang, C. W. Yu (Hong Kong University of Science and Technology) . . . . . page 29
2 ***Lawrence Livermore National Laboratory ULTRA-350 Test Bed***
   D. J. Hopkins, T. A. Wulff, K. Carlisle (Lawrence Livermore National Laboratory) . . . . . page 33
3. ***Lorentz Motor With Stationary Magnets and Coils Applied in a 6-DOF Contactless Motion Stage***
   L. Jabben, P. M. Overschie, H. F. Van Beek (Delft University of Technology), and A. Molenaar (SKF Engineering & Research Centre) . . . . . page 39

Session IV

Thursday, April 19, 9:00 a.m. – 10:30 a.m.

1. ***Quiet Hydraulic Actuators for the Laser Interferometer Gravitational Wave Observatory (LIGO)***
   C. T. Hardham, G. S. Allen, D. B. DeBra, W. Hua, B. T. Lantz, J. G. Nichol (Stanford University) . . . . . page 43
2. ***AC Motor Control in Precision Machines***
   M. K. Liebman, D. L. Trumper (Massachusetts Institute of Technology) . . . . . page 47
3. ***Precision Motor Control Development Using Rapid Control Prototyping Tools***
   E. Hill, R. Venugopal, V. Moudgal (dSPACE, Inc.) . . . . . page 51

Session V

Thursday, April 19, 11:00 a.m. - 12:00 p.m.

1. ***Adapting Feedforward for Active Vibration Isolation Systems****
   P. G. Nelson, E. Kraner (Technical Manufacturing Corporation) . . . . . page 55
2. ***Enhancing Positioning Performance of Lithography Stages Using Smart Structures Technology***
   B. Pletner, H. Dorn (Active Control eXperts (ACX), Inc.) and M. Karpel (Techninon – Israel Institute of Technology) . . . . . page 56

Session VI

Thursday, April 19, 2:30 p.m. - 4:00 p.m.

1. ***High Gain Control for High Performance-Dusting Off the Classics***
   D. E. Schinstock, Z. Wei (The University of Tulsa) . . . . . page 62
2. ***A Six-degree-of-freedom, Piezoelectrically Actuated Translation Stage***
   R. M. Seugling, S. T. Smith (University of North Carolina at Charlotte), R. H. R. Jacobs (Technical University of Eindhoven), L. P. Howard (YAFO Networks, Inc.), and T. LeBrun (National Institute of Standards and Technology) . . . . . page 66
3. ***Methods and Results of Reducing Following Error in the LLNL Large Optic Diamond Turning Machine****
   D. J. Hopkins (Lawrence Livermore National Laboratory) . . . . . page 71

Session VII

Friday, April 20, 9:00 a.m. - 10:30 a.m.

1. ***The Design of the Kolibri DVD-actuator***
   F. G. A. Homburg (Philips Optical Storage) . . . . . page 72
2. ***Submicrometer Friction Compensation Using Variable-gain Sliding Mode Control***
   P. I. Ro (North Caroline State University), and W. Shim (Seagate Technology) . . . . . page 78
3. ***Laminar Flow Actuation on Ultraprecision Stage Positioning***
   H-C. Wu (Western Digital Corporation), and D. B. DeBra (Stanford University) . . . . . page 84

Session VIII

Friday, April 20, 11:00 a.m. – 12:00 p.m.

1. ***Development of a High Bandwidth, High Power Linear Amplifier for a Precision Fast Tool Servo System***
   S. Rakuff, J. F. Cuttino (University of North Carolina at Charlotte), and D. E. Schinstock (The University of Tulsa) . . . . . page 88
2. ***Repetitive Control of a Rotary Fast Tool Servo***
   J. A. Calzaretta, S. J. Ludwick, M. F. Byl, D. L. Trumper (Massachusetts Institute of Technology) . . . . . page 94

* *Extended abstract not available at printing*

Technical Papers

Tachometers, Do We Need Them?

Daniel B. DeBra, AA, Stanford University, CA 94305

Keywords: tachometer, differentiation, digital filtering, precision stage positioning

Introduction

To introduce the numbers that are involved consider a carriage of mass m with a direct forcing control and negligible friction. If one nanometer is the desired rms value of the noise nx that would be contributed by a position sensor one can talk about the equivalent velocity noise that could be allowed from a velocity sensor before it became the principal disturbance. Now compare a proportional plus derivative feedback with one that uses a velocity sensor for an inner loop and the same proportional gain for the outer loop. In both cases consider the velocity gain to be large enough that the natural behavior is critically damped and the roots are at Cp/Cd =100 and Cm/m = 1000 rad/sec. The position sensor noise has unity gain to 1000 rad/sec in the first case while at higher frequencies it is attenuated with a minus one slope. By contrast with the first case the position noise starts to be attenuated at 100 rad/sec and decreases with a minus 2 slope above 1000 rad/sec. Unfortunately there is a new noise source from the velocity sensor. Its gain at low frequencies is Cd/Cp. For the velocity noise nv to be small it must be nv<<nx Cp/Cd = 1e-9*1e2=1e-7 m/sec. Or say the velocity noise should be 0.1 of that then for a capstan drive with radius 1 cm we would need a rotational noise less than 1e-6 rad/sec. This is achievable but is not an inexpensive tachometer. It corresponds to about 5 revolutions per year and represents a high quality instrument that may be larger than the motor on which it is mounted. But even in this primitive case it allows one to attenuate the noise from the position sensor above the Cp/Cd frequency. The response of the system to a disturbance on the carriage is the same for both cases. Its gain is 1/Cp and reduces with frequency with a minus one then a minus two slope at Cp/Cd and Cd/m respectively. These slopes in the attenuation may be more or less important for real colored noise.

Life becomes more interesting when the elasticity of the capstan shaft, the contact compliance and the stretch and bending of the draw bar are considered in the capstan driven case. The inertia of the capstan drive and the carriage interact as a fourth order system. The position sensor needs to be on the functional part--the carriage. So the control is not collocated with the sensor leading to some problems in stability if high gain is needed to reduce the effects of disturbances. This is where the introduction of a second sensor on the capstan drive becomes important especially if the disturbance such as friction is associated with the capstan drive e.g. brush friction on a motor. High gains about the capstan drive are now possible with a tachometer both because it is collocated and because it is now a first order system.

Given that velocity information is needed the question is then can one achieve the angular velocity information from an encoder or do we need to depend on the demonstrated precision of the classical tachometer? DTM3 [Bryan 1980], had tachometers on its capstan drives that provided a resolution of 1 rev/5 yrs. With a rapid traverse that was limited by the slew rate of the laser interferometers of the day to a few cm/sec the dynamic range offered by the tachometer was from 3e-8 to 10 rad/sec or greater than 9 orders of magnitude. Furthermore to maintain the resolution of 1e-9 m the orientation equivalent for the 1 cm radius capstan is 1e-7 rad or 60 million bits per revolution. If discrete encoders are used one must do the best job possible to derive the velocity information from this sequence of discrete measurements.

Discrete differentiation

There are a number of ways of approximating the derivative given a sequence of discrete values of a variable. The z-transform can be used to find the coefficients for weighting values of the sequence when the samples are measured at uniform time intervals, T. To develop a control for PD (proportional plus derivative), the Laplace transform, (Cp+Cd*s)*y can be approximated as Cp*y0+Cd*(y0-y1)/T or (Cp+Cd/T)*y0-Cd*y1/T using the definition of a derivative. By zero-pole matching, Cd*(s+Cp/Cd)=>Cz*((z-z1)/(z-z2)) where z2 can be 0 to match the first form or -1 and z1=exp(s1*T) where s1=-Cp/Cd and matching gains at s=0 and z=1, Cz=Cp((1-z2)/(1-z1)). For small T this gives same result as the first method. But neither provides much flexibility in design to minimize the error in approximating the derivative. It is easier to compare methods if the derivative is calculated separately. If the sequence of measured values is fitted with a polynomial

y=a0+a1*t+a2*t^2+....

and t=0 is the current value then the derivative is just the coefficient a1. For t=0, the value measured is y0, for t=-T, y1 et c. for a sampling period T. Given m measurements and a polynomial of degree p-1, for m>=p one can fit the data by least squares. M*a=y , where

M=[1 0 0...; 1 -T -2T...; 1 (-T)^2 (-2T)^2...; et c.]

then for e=M*a-y, minimizing the J=e'*e gives a=(M'*M)\M'*y. But we only need a1 so only the second row of the matrix is of interest. For the unweighted case this second row V contains 1/T. For example for some m and p up to 6 and 4 respectively, V(m,p)=Vmp/T with the Vmp given below (the first few are easily checked by hand)

```
V22 =
  1.0000e+00  -1.0000e+00
V42 =
  3.0000e-01   1.0000e-01  -1.0000e-01  -3.0000e-01
V33 =
  1.5000e+00  -2.0000e+00   5.0000e-01
V43 =
  1.0500e+00  -6.5000e-01  -8.5000e-01   4.5000e-01
V63 =
  5.8929e-01  -3.5714e-03  -3.2857e-01  -3.8571e-01  -1.7500e-01   3.0357e-01
V44 =
  1.8333e+00  -3.0000e+00   1.5000e+00  -3.3333e-01
V55 =
  2.0833e+00  -4.0000e+00   3.0000e+00  -1.3333e+00   2.5000e-01
V65 =
  1.8188e+00  -2.6772e+00   3.5450e-01   1.3122e+00  -1.0728e+00   2.6455e-01
```

One may wish to weight the values closest to time t=0 to preserve the bandwidth and respond more quickly to sudden changes. Then the function to minimize is J=e'W'We which gives the standard result for a=(M'W'WM)\(M'W'W)*y. Again only the second row is of interest and as before, once the sampling time is known the matrix is determined and gives a constant row vector which need only be calculated once at the start.

When the measurements are not weighted, the zeros of the z-transfer function all occur on the unit circle. Increased weighting of current values brings the zeros (except the one at +1) closer to the center of the unit circle.

Figure 1 shows the effect of weighting:

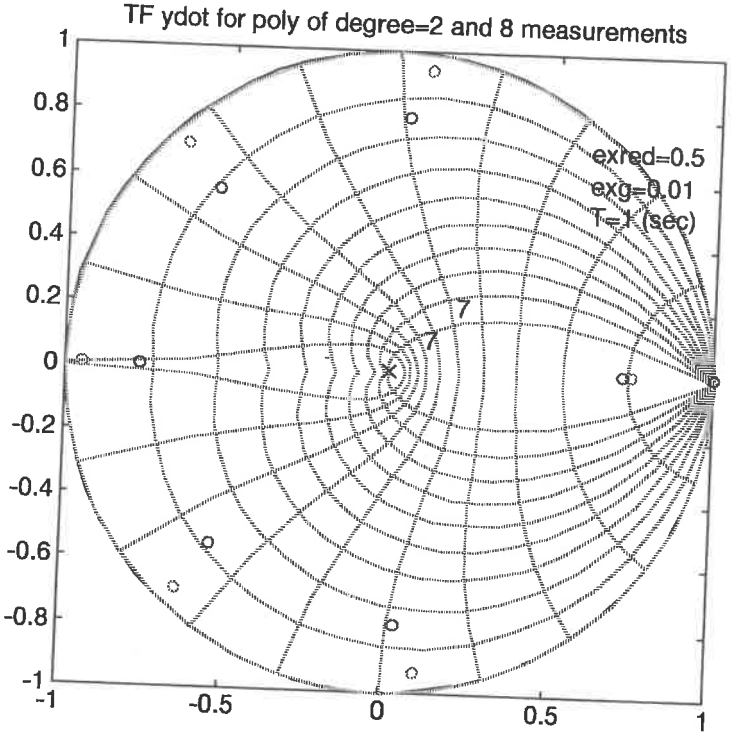

Figure 1, Weighting brings the extra zeros closer to the origin

The polynomial fitted transfer function spreads the zeros around compared to the classical filter thereby preserving the phase, see Fig. 2.

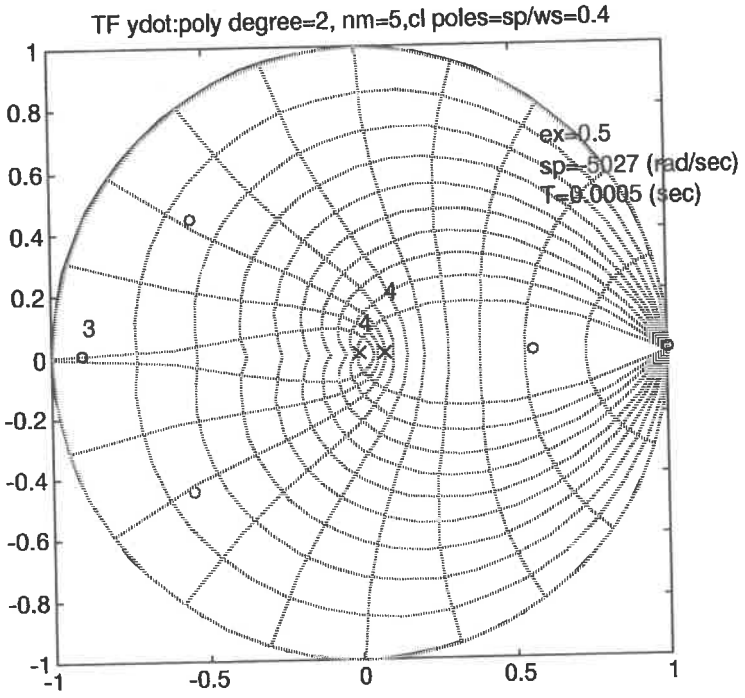

Figure 2. The classical filter has 4 poles placed at 0.4 ws and its zeros at -.9 to avoid the phase singularity as w->ws/2.

The discrete frequency response shows the comparison with the phase preserved better with the polynomial fit than with the classical filter. See Figure 3a and 3b.

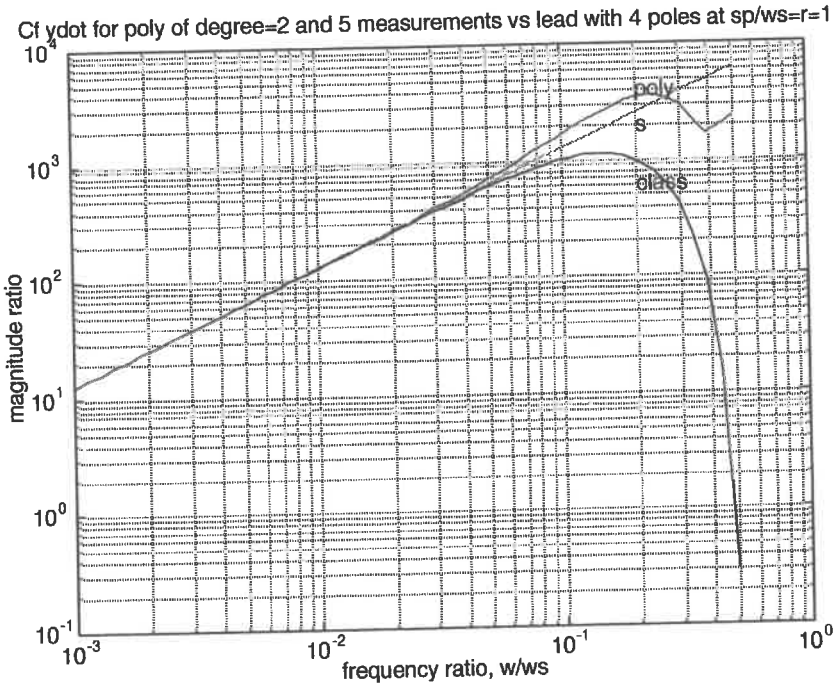

Figure 3a The polynomial filter compared with a perfect 's' and the classical filter.

The slight increase in amplitude slope of the polynomial fit is necessary to preserve the phase as can be seen on Fig 3b. When compared with a classical design with the same number of poles set at a ratio r to the sampling frequency ws, the discrete Bode plot shows the improvement one can obtain with a polynomial fit. Even with r=1, and for p=3 (polynomial of 2nd degree) and m=5 , phase is preserved to within 10 deg up to w/ws=0.07 for the polynomial fit while the classical fit has deviated 10 deg by w/ws=0.01 and falls off sharply reaching a phase error of -65 deg by w/ws=0.07.

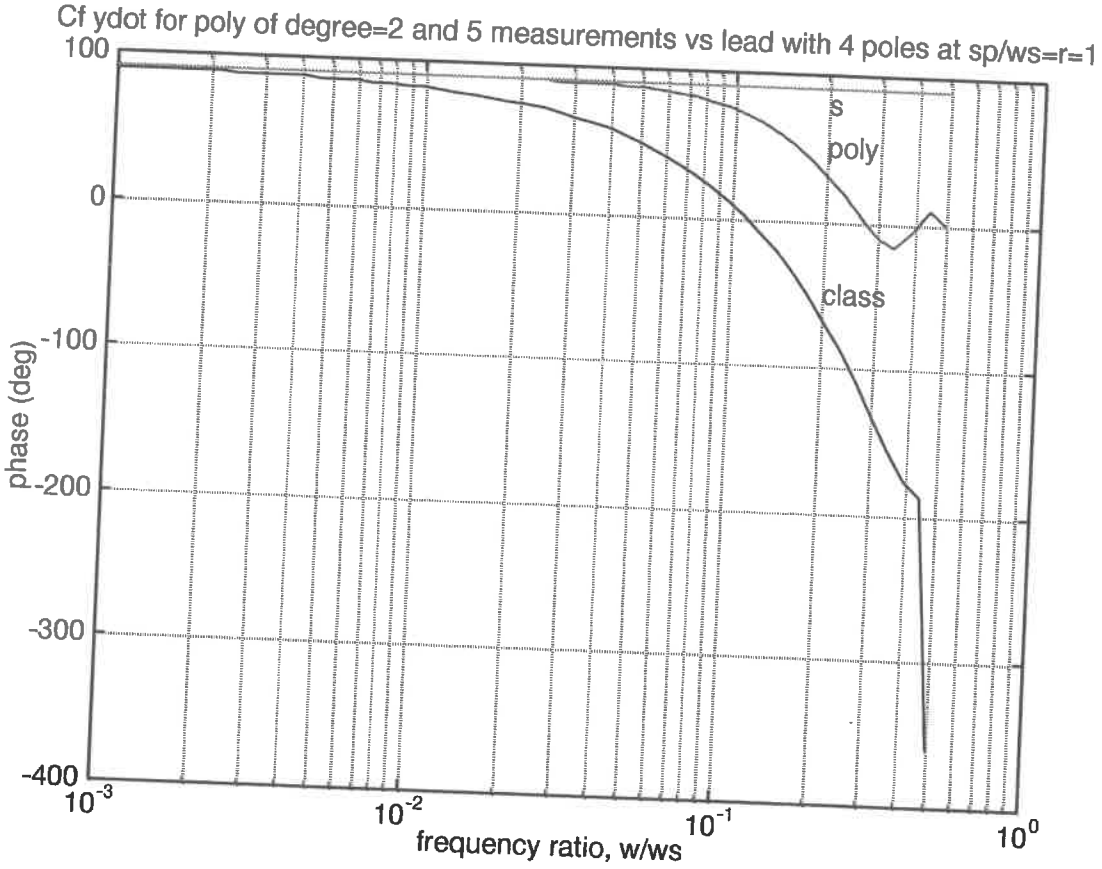

Figure 3b. Phase for the polynomial fit compared with a perfect 's' and a classical filter.

The need for velocity is greatest for an inner loop where the bandwidth is high. It is clear that one needs high sampling rate to preserve the fidelity of the velocity derived discretely. Some improvement can be made by this method of polynomial fitting. But care should be taken not to sample too fast especially if an integral control term is included lest the change each period is smaller than the least significant bit and the integral is lost.

Additional considerations

When the stiction is on the stage as it might be for a carriage in a hard vacuum riding on plane ways there is a good case to make for a direct drive so the position sensor can be collocated. Then the discrete differentiation can improve the bandwidth and is a significant improvement. If the friction is also on a capstan drive, one needs to obtain high bandwidth on the feedback to both inertias: the carriage and the capstan drive. Here one needs to have the carriage

position and a good measure of the elastic deformation to use as the 'control' on the carriage and use the tachometer on the capstan drive to calculate the control on the inner inertia. The elastic deformation involves the relative displacement so the integral of the tachometer needs to be computed for comparison with the outer stage position. This places additional requirements on the low frequency noise of the tachometer.

Estimation and model based filtering can be very effective as long as the dynamic behavior and models of disturbances are predictable. However when stiction is involved or other disturbances that change suddenly there is no substitute for measurement bandwidth.

Conclusion

When friction or other disturbances require high bandwidth the value of velocity information and collocated sensors on each inertia become important. For precision applications it is still hard to find discrete sensors that can provide the performance of a tachometer. Analog inner loops are still the best choice in many cases and the tachometer should be with us for quite a while for as we push for higher accuracy the very characteristics that makes the tachometer so impressive become more valuable and harder to replace.

Controller Requirements for High-Precision Motion Applications

Curtis S. Wilson
Vice President of Engineering and Research
Delta Tau Data Systems, Inc., Chatsworth, CA

Introduction

High-precision motion control applications put demands on a motion controller that many other applications do not. Many of the requirements are subtle, and not immediately obvious from data sheets. The designers of motion controllers must take special care to handle numeric issues, data rates, interpolation strategies, fast servo updates, and many other issues properly if they are to succeed in properly controlling a precision application. This paper surveys the key strategies required for success.

Commanded Trajectories

Proper strategies for commanded trajectories are vital for the success of high-precision motion applications. This subject is ignored in virtually all academic controls courses, but it is at least as important as the servo algorithms used.

Traditionally, commanded trajectories used a resolution no finer than the feedback resolution itself. In days where every byte of storage and computation was precious, this strategy made sense. It does, however, impose some serious performance limitations. The ideal intermediate points in most trajectories are not in whole numbers of "counts". The quantization noise introduced by forcing each point to the nearest integer count can be significant.

Even worse are the effects if feedforward is used. The most common feedforward terms, velocity and acceleration feedforward, require digital differentiation of the commanded trajectory – a noise-producing operation. Without substantial fractional resolution, these terms cannot reasonably be used, or used to maximum effect. A lot of the lore about problems with feedforward stems not from the technique itself, but from its use with inadequate resolution.

If positions are generated incrementally – each cycle's commanded position using the previous cycle's position as the seed for calculations – substantial fractional resolution is required to minimize numerical integration errors. This is particularly important in multi-axis applications to preserve proper coordination, which often means path accuracy, between axes.

Some of the most careful attention to numerical techniques mu st be paid in the area of trajectory generation. While many believe that floating-point math is superior to fixed-point math in all aspects, this is not necessarily true. If positions are represented as floating-point numbers, the amount of fractional resolution changes with the position. At a million counts – 100mm from the origin with nanometer resolution – 20 bits of fraction are lost. At a billion counts – 1m from the origin with nanometer resolution – 30 bits of fraction are lost. It is easy to see that standard 32-bit floating-point formats for position representation are utterly inadequate for precision applications. Care even must be taken with 64-bit floating-point representations here.

Furthermore, because floating-point representations are inexact, round-off errors from repeated addition operations can accumulate to become significant, even in applications where high precision is not required, and the floating-point resolution initially appears to be sufficient. If this is a problem in an application, a simple substitution of multiplication for some addition operations can fix the problem.

Virtually all controllers generate their commanded position trajectories using polynomial equations. As controllers have improved, the order of these equations has increased. The earliest digital controllers in the 1970's used first-order position trajectories, which could generate constant-velocity segments, but not control acceleration and deceleration. These systems required substantial lag in the analog servo drives to create physically realizable trajectories.

The second-order trajectories that became common in the 1980's permitted basic acceleration control and reasonably smooth cornering (C^1 continuity). This in turn permitted tighter servo control because the need for servo

lag was drastically reduced. Still, these requested step changes in acceleration, and hence in force and motor current, and step changes in curvature, none of which are truly physically realizable.

The third-order trajectories that some controllers introduced in the 1990's permitted jerk control and continuity in path curvature (C^2 continuity). With these, features such as "S-curve" acceleration and cubic splines could be implemented, to powerful effect.

The use of higher-order equations that can generate physically realizable trajectories is particularly important in precision systems that aggressively use feedforward to minimize tracking errors. Systems with substantial tracking errors, or "servo lag", can count on the lag to smooth out sudden command changes, but at the cost of accuracy.

Techniques such as S-curve acceleration are, in effect, low-pass filters on the command trajectory. These serve to prevent the excitation of higher-frequency resonances in the system. A newer technique is to build a band-reject filter into the commanded trajectory for the selective rejection of resonant frequencies, without also rejecting higher frequency content that can provide quick action.

It is still very common to reconstruct contours by commanding points directly on those contours with trajectories (such as "linear interpolation") that inherently fall to the inside of the curve. In doing so, errors are created in the commanded trajectory that dwarf other errors in the system. A modern precision controller must be able to support more accurate contouring trajectories, such as Hermite splines, to minimize these errors.

Feedback Issues

In high-precision applications, the controller must be able to accept feedback signals at data rates (expressed in LSBs per unit time) far exceeding typical motion control applications. The strategies this requires, both in hardware and software, can be different from those for standard control algorithms.

The first and simplest strategy is simply to use fast digital interface circuitry. While a standard quadrature encoder is hard-pressed to put out 500 kHz edge (count) rates, the incremental outputs from precision sensors can often put out 20+ MHz edge rates. Precision controllers must accept these rates.

Many precision sensors, such as interferometers, output a parallel digital data word representing position (or at least distance from a starting point). A precision controller must have the ability to latch a stable data word synchronously with the control-loop execution. If the controller has the ability to perform "software extension" of the position data, then it can interface to only a less significant portion of the parallel word, saving complexity and money.

Increasingly, controllers are asked to accept directly the "sine-cosine" analog signals from interferometers, linear scales, and rotary encoders, and resolve them with a high degree of interpolation. This interface typically requires a hybrid analog/digital interface, with a digital cycle counter and a pair of analog-to-digital converters combined with an arctangent algorithm (in hardware or software) to determine where within the cycle the system is. Good algorithms to combine the integer and fractional components of the cycle count without any transition glitches are difficult, but essential.

Servo Algorithms

Perhaps surprisingly, most high-precision motion applications do not require complex servo algorithms. Most of these systems engineer their mechanical systems so well that they do appear to the controller as simple rigid bodies; if hydrodynamic bearings are used, the problem of non-linear mechanical friction disappears as well. Standard-format PID controllers do very well on this type of system.

What the servo algorithms for these systems do require is a lot of speed and a lot of resolution. In the vast majority of industrial digital control systems, what limits the gains of the servo loop is not the classic stability criteria, but delays and quantization noise due to limited resolution. Delays, which add destabilizing phase lag to the loop, come first from the digital sample rate, which automatically introduces a half-cycle delay, and if velocity information is derived from position feedback, from the digital differentiation for the feedback, which introduces another half-cycle delay.

Further delays come from the finite calculation time between when the feedback is read and the command effort is computed, and from the "transport delays" required to get the computed value(s) converted to actual physical signals to drive the actuator. Many modern "smart" drives – digital drives with analog inputs – have exacerbated this problem by compounding these delays. A digital controller samples the position periodically, closes the position and possibly velocity loop, clocks the data to a digital-to-analog converter so the command is sent to the drive in analog form. The analog-to-digital converter in the drive periodically, but asynchronously to the controller, samples this signal, closes the current loop and possibly the velocity loop, then converts the voltage command effort values to physical signals. Multiple sample cycles of delay build up through this process, drastically reducing the gain, and hence the performance, of the system.

It is vastly superior from this point of view to close all of the loops in a single processor and quickly convert the command output values to physical signals (usually PWM on-off signals to the power transistors). This fully digital control scheme – including digital current-loop closure – can provide greatly superior gains, resulting in better stiffness, disturbance rejection, bandwidth, accelerations, settling times, and other attributes.

The finite resolution of digitized feedback also limits gains. Providing higher feedback resolution to the servo loop, particularly if the numeric values are differentiated (as in a velocity loop from position feedback), can substantially improved system performance, even if there are not corresponding increases in repeatability and accuracy. In one test, a common physical system consisting of a 1 kW brushless motor with a 1000-line sinusoidal encoder directly driving a ballscrew with a 10 kg load was tested with various degrees of interpolation on the encoder. The test move was a 25 mm move, settling to 1 micron. The results were:

- "x4" decode (4000 states per rev): 100 msec
- "x256" interpolation (256,000 states per rev): 75 msec
- "x4096" interpolation (4,096,000 states per rev): 60 msec

Elimination of mechanical friction through tools such as air bearings can be very important in precision applications to avoid the issues of "stick-slip" oscillations, but by eliminating the damping effect provided by the friction (even if it is non-linear), stability issues are made worse for the controller. A good rule of thumb is that the servo loop must be closed at twice the frequency of a comparable system with a little mechanical friction. As a practical matter, the servo update rates for these systems are a minimum of 4 kHz.

Feedforward terms as part of the servo algorithm can be critical in a precision system to keep tracking errors to a minimum, not waiting for errors to build up for the feedback algorithms to react. Luckily, high-precision mechanics are particularly amenable to the aggressive use of feedforward, with their dynamics typically being quite simple and readily modeled. In such a system, over 99% of the servo command can come from the feedforward terms, with the feedback algorithms just providing the occasional correction for disturbances and modeling errors.

Commutation Algorithms

In many applications that require limited precision, a simple switching commutation strategy for brushless motors, commonly known as "six-step" commutation, can be employed. In high-precision applications, more sophisticated commutation algorithms, commonly known as "sinusoidal" commutation, almost invariably must be used.

Even with "trapezoidally wound" brushless motors, six-step commutation provides significant torque/force ripple over the span of a single step, and the sudden switching of current in phases at step boundaries produces a noticeable torque/force perturbation. This can result in visible marks in the surface finish of a cut part, for example.

Because the torque produced by a commutation algorithm is proportional to the cosine of the measurement error in the rotor's magnetic field angle, small measurement errors, such as those due to resolution limitations, have little effect on the results of the algorithm. Therefore, it is not necessary to have as much resolution for the commutation algorithm as for the servo algorithm. Typically, however, the commutation algorithm uses the same sensor as the servo algorithm. All of this resolution may not be used; it is common to use the closest point in a sinusoidal look-up table of more limited resolution.

The strategy for closing the current loop is inextricably tied up with the commutation algorithm. Microprocessors, particularly DSPs, have recently gotten fast enough to perform current-loop closure digitally. This permits several

important improvements. First, analog transmission of commands, which are noise-sensitive, can be eliminated. Second, it is possible to do all of the feedback calculations, for position loop, velocity loop, commutation and current loop, in a single processor, minimizing transport and calculation delays, which, as explained above, leads directly to higher possible gains and performance.

Compensation Algorithms

No physical system is perfect, and it is often more cost-effective to measure these physical errors and compensate for them algorithmically than to fix them physically. A good precision controller needs a variety of techniques to compensate for errors. These usually include position ("leadscrew") compensation tables with independent corrections in the positive and negative directions, two-dimensional and sometimes even three-dimensional compensation tables, and squareness correction algorithms.

At the highest levels of precision comes the realization that even the best systems that are supposedly Cartesian are never truly Cartesian, especially as temperatures vary. Advanced users are now experimenting with the use of robotic-style kinematic algorithms to handle these slight deviations from the ideal Cartesian systems.

Synchronization Issues

In these applications, the motion itself is really only a means to an end, with the motion required to create a certain spatial relationship for an operation. In many applications it is desired to perform an operation during rapid motion with as tight a relation as possible to the physical position. Two strategies that can assist in this are "position-capture" and "position-compare" circuits.

Traditional controllers have performed these functions in software, limiting the accuracy of these functions due to the latency of the software loop. Around 1990, controllers started to appear with dedicated digital hardware for the capture and compare functions, eliminating software delays. The transition of a digital input signal (encoder index, probe switch, proximity sensor) immediately "captures" the present encoder counter value into a dedicated register, independent of where it is in the servo cycle. The software can then process this information later without its delays hurting the accuracy of the process.

The position-compare process is logically the inverse of the capture. The processor pre-loads a hardware register with a value equal to the encoder count at which an output signal is desired. Without further software intervention, the digital hardware "continually" compares this value to that of the encoder counter. When the two values are the same, a digital output value is immediately triggered.

These digital-hardware techniques revolutionized the synchronicity of motion to digital inputs and outputs. However, as demands for higher resolution have taken the processing of feedback past simple digital quadrature into more complex hybrid analog-digital processing, the capabilities of the digital capture and compare techniques have not kept pace with the increased resolution.

A new technique rectifies this imbalance. The digital hardware associated with the encoder counter uses dedicated timer circuits to compute fractional count values at the same rate at which the counter can increment. With updated fractional count information now always available, the capture and compare circuits can be extended to incorporate the fractional information as well. When used with interpolation circuitry for sinusoidal encoders, as long as the zero-crossings of the sine and cosine waves are used internally to feed a counter associated with the timers and capture/compare circuitry, the resolution of these circuits can "catch up" to that of the interpolator.

(Note that earlier timer-based strategies for sub-count interpolation only calculated the fractional count information once per servo cycle – inadequate for immediate capture and compare functions.)

Because the zero-crossings of sinusoidal encoders are their most "dependable" feature, this purely digital timer-based circuitry is not only simpler and less expensive that analog-based capture/compare circuits, it is at least as accurate as well.

Sinusoidal Velocity Profiles for Motion Control

A review on traditional solutions and a proposal for a solution with reduced piece–wise constructors and reduced harmonic content of the kinetic perturbations

Victor M. Arevalo
Augen Opticos, S.A., Ensenada, B.C., Mexico 22830

Background

When facing the simplest and first question to be made with a motorized motion: how to perform the change of position from one point to another, the present technical literature provides similar answers to those given 30 years ago.

The available solutions can be summarized as follows:

- Constant Velocity Window.- For mass–reduced, robust mechanisms, with enough power to tolerate the acceleration impulses at the beginning and the end of this type of motion. This method is not regarded as a "solution" herein.
- Trapezoidal Velocity Profile.- Produces rectangular acceleration windows. The jerk obtained is in the form of impulses (4 in total), aligned with the edges of the acceleration windows.
- S–Curve Velocity Profile.- Part of the work reported in this paper is the development of a procedure that generalizes the treatment of this family of profiles. The generalization includes the special cases of "short travel" and allows to "select" the particular profile by means of a single parameter (denoted as γ in the example figures). By varying continuously γ from 0.0 to 1.0, the profile respectively evolves from "impulsive jerks" (i.e. the Trapezoidal Velocity Profile, appearing as a particular and extreme case of the S–Curve **family** of functions), to its maximum "smoothness", namely, triangular acceleration profile and minimization of both, jerk and peak–power values.

The analytical flexibility offered by these solutions is a tradeoff with their features. As shown in the final summary table, the benefit of reduced peak values of power and jerk has a cost of additional components in the piece–wise construct of the functions. Even after the identification and utilization of symmetry points for mirror simplification, the constructors count is still high.

As a final word, the traditional velocity profiles are solutions of such numerical simplicity that can be used when computing power is expensive, limited or absent. However, the use of computerized control increases to the point that in some cases it is mandatory.

As long as assertions like: "*Over the past 30 years the price of computer processing power has declined by an annual average of 30% in real terms*", and "*... the cost of a unit of computer processing power has fallen by 99% over the decade*"[1] can be made, it is clear that computer utilization in motion control is not an affected trend, but a strong foundation.

Proposal

This work proposes a motion profile named Sinusoidal Velocity Profile. It is a piece–wise construct with 3 components: An acceleration zone, a constant speed zone and the corresponding decelerating zone, similar to the construction used in trapezoidal profiles.

Procedures

The calculation procedures will be developed in a dual fashion: As a procedural review of the traditional S–Curve, and as a presentation of the proposed Sinusoidal profile.

The following parameters are required:

- Vm ≡ Maximum Velocity allowed (absolute value).
- Am ≡ Maximum Acceleration peak value allowed (absolute value).
- Throw ≡ The travel distance (positive or negative).

Also, when dealing with the S-Curve profile, the parameters set must include γ, dimensionless quantity varying from 0.0 to 1.0 as explained above. The effects of some typical values are shown in the final summary table.

The numerical format for these and the rest of the variables employed herein is not restricted to be integer and the units adopted for these variables can be freely selected according to the natural specification of the motion environment (resolver counts, micrometers, millimeters, meters, inches, etc.). The general idea with this approach is that, for the sake of self–documentation and clarity, the calculation part of the control system contains the user's abstraction of the problem, and the required conversions (resolver integer counts, stepper pulses, etc.) can be made at the final "delivery" stage of the process. Conversely, when "reading" from the physical devices, the conversion of units made at the "source" of the information favors maintenance and inspection versatility.

With the "user" set of parameters in hand, another set of 12 (with a temporary *Yaux* added for a total of 13) "calculation" parameters is obtained prior to the utilization of the procedural formulas. In terms of software implementation it is convenient that this initialization procedure be confined in a function (or subroutine). This will be referred to, as the Initialization Sequence:

No.	Profile Type	Initialization
1	Both	$Sgn = sgn(Throw)$
2	Both	$Yf = \lvert Throw \rvert$
3	Both	$Ys = \frac{Yf}{2}$
4	S-Curve	$Yaux = \frac{1}{2}\cdot(1+\gamma)\cdot\left(\frac{Vm^2}{Am}\right)$
	Sinusoidal	$Yaux = \frac{Vm^2}{Am}$
5	Both	$Ya = \begin{cases} Ys & \forall\ Ys \le Yaux \\ Yaux & \forall\ Ys > Yaux \end{cases}$
6	S-Curve	$Vw = \begin{cases} \sqrt{\frac{Ys\cdot Am}{\frac{1}{2}\cdot(1+\gamma)}} & \forall\ Ys \le Yaux \\ Vm & \forall\ Ys > Yaux \end{cases}$
	Sinusoidal	$Vw = \begin{cases} \sqrt{Ys\cdot Am} & \forall\ Ys \le Yaux \\ Vm & \forall\ Ys > Yaux \end{cases}$
7	Both	$To = \frac{Vw}{Am}$
8	S-Curve	$Ta = To\cdot(1+\gamma)$
	Sinusoidal	$Ta = 2\cdot To$
9	S-Curve	$\tau = \gamma\cdot To$
	Sinusoidal	$\omega = \frac{2\cdot\pi}{Ta}$
10	S-Curve	$Tm = \frac{Ta}{2}$
	Sinusoidal	$Ks = \frac{Ta\cdot Vw}{4\cdot\pi^2}$

No.	Profile Type	Initialization (continued...)
11	Both	$Tk = 2\cdot\frac{Ys-Ya}{Vm}$
12	Both	$Ts = Ta + \frac{Tk}{2}$
13	Both	$Tt = 2\cdot Ts$

The following figures are generic outlines for arbitrary (S–Curve or Sinusoidal) profiles, intended as a graphical description of some of the the variables employed in this section.

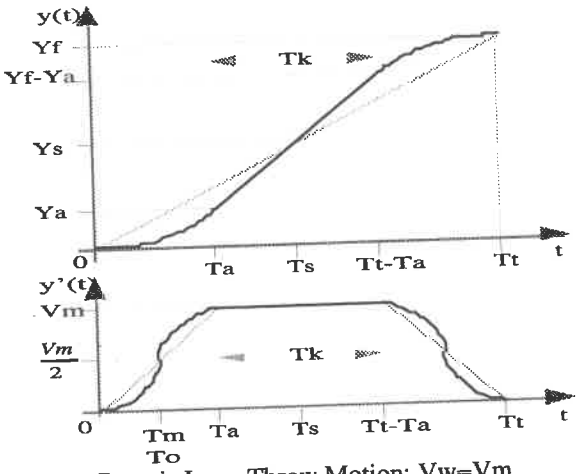

Generic Long Throw Motion: Vw=Vm

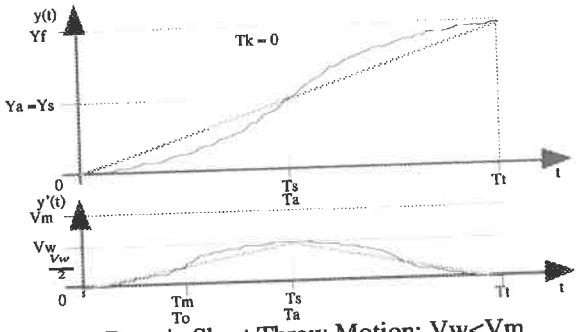

Generic Short Throw Motion: Vw<Vm, Ya=Ys, Ta=Ts

The procedural equations can be stated in several ways and the adoption of a particular style is a matter of taste, and available space. That is the reason for the adoption of the "recursive" style. Although the software implementation was experimented following both, the "classical" style (using auxiliary functions) and the "recursive" style, apart from the characteristic compactness of the later, there are not improvements in performance in following a particular style.

$$y(t) = Sgn \cdot \hat{y}(t)$$

$$\hat{y}(t) = \begin{cases} 0 & \forall\ t \le 0 \\ \left(\frac{1}{2}\cdot\frac{Vw}{To}\right)\cdot\left(\frac{t^3}{3\cdot\tau}\right) & \forall\ 0 < t < \tau \\ \left(\frac{1}{2}\cdot\frac{Vw}{To}\right)\cdot\left[\left(t-\frac{\tau}{2}\right)^2+\frac{\tau^2}{12}\right] & \forall\ \tau < t \le To \\ Ys + Vw\cdot(t-Ts) + \hat{y}(Ta-t) & \forall\ To < t \le Ts \\ Yf - \hat{y}(Tt-t) & \forall\ Ts < t \end{cases}$$

Equations Set ***1-a:*** S-Curve Profile Position

$$y'(t) = Sgn \cdot \hat{y}'(t)$$

$$\hat{y}'(t) = \begin{cases} 0 & \forall\ t \le 0 \\ \left(\frac{Am}{2}\right)\cdot\left(\frac{t^2}{\tau}\right) & \forall\ 0 < t < \tau \\ \left(\frac{Am}{2}\right)\cdot(2\cdot t - \tau) & \forall\ \tau < t \le To \\ Vw - \hat{y}'(Ta-t) & \forall\ Tm < t \le Ts \\ \hat{y}'(Tt-t) & \forall\ Ts < t \end{cases}$$

Equations Set ***1-b:*** S-Curve Profile Velocity

$$y''(t) = Sgn \cdot \hat{y}''(t)$$

$$\hat{y}''(t) = \begin{cases} 0 & \forall\ t \le 0 \\ \left(\frac{Am}{\tau}\right)\cdot t & \forall\ 0 < t < \tau \\ Am & \forall\ \tau < t \le To \\ \hat{y}''(Ta-t) & \forall\ Tm < t \le Ts \\ -\hat{y}''(Tt-t) & \forall\ Ts < t \end{cases}$$

Equations Set ***1-c:*** S-Curve Profile Acceleration

$$y(t) = Sgn \cdot \hat{y}(t)$$

$$\hat{y}(t) = \begin{cases} 0 & \forall\ t \le 0 \\ \frac{Am}{4}\cdot t^2 + Ks\cdot(\cos(\omega\cdot t)-1) & \forall\ 0 < t \le Ta \\ Ys + Vw\cdot(t-Ts) & \forall\ Ta < t \le Ts \\ Yf - \hat{y}(Tt-t) & \forall\ Ts < t \end{cases}$$

Equations Set ***2-a:*** Sinusoidal Profile Position

$$y'(t) = Sgn \cdot \hat{y}'(t)$$

$$\hat{y}'(t) = \begin{cases} 0 & \forall\ t \le 0 \\ Ks\cdot\omega\cdot(\omega\cdot t - \sin(\omega\cdot t)) & \forall\ 0 < t \le Ta \\ Vw & \forall\ Ta < t \le Ts \\ \hat{y}'(Tt-t) & \forall\ Ts < t \end{cases}$$

Equations Set ***2-b:*** Sinusoidal Profile Velocity

$$y''(t) = Sgn \cdot \hat{y}''(t)$$

$$\hat{y}''(t) = \begin{cases} 0 & \forall\ t \le 0 \\ \frac{Am}{2}\cdot(1-\cos(\omega\cdot t)) & \forall\ 0 < t \le Ta \\ 0 & \forall\ Ta < t \le Ts \\ -\hat{y}''(Tt-t) & \forall\ Ts < t \end{cases}$$

Equations Set ***2-c:*** Sinusoidal Profile Acceleration

The presented sets of equations are for $y(t)$ –position–, $y'(t)$ –velocity–, and $y''(t)$ –acceleration– (sets 1–a, 1–b and 1–c respectively for S–Curve and sets 2–a, 2–b and 2–c respectively for Sinusoidal). The independent variable t is the local time in terms of a particular profile motion which starts at $t = 0$, and finishes with $t = Tt$. Any subsequent motion restates its own t.

Note that the following validation checks are performed: $y(t) = 0 \quad \forall\ t \le 0$ and $y(t) = Throw \quad \forall\ t > Tt$ for position boundaries.

Also, all the velocity and acceleration boundaries (when $t \le 0$ and $t \ge Tt$) are validated to ZERO values.

Results

Higher order derivatives, jerk (acceleration derivative) and the so called "jounce" (jerk derivative) can be similarly obtained. Note that the jounce for the S-Curve profile is a set of impulses even for the smooth case. Conversely, the jounce for the Sinusoidal profile is a pair of windowed cosine functions. This result is associated to the fact that the harmonic content of the sinusoidal curves (acceleration and jerk), by definition is the minimum attainable, when compared with the triangular and rectangular counterparts.

The experimental work with these procedures in a target servomechanism confirmed the expectations made with the Sinusoidal profile. Although the observations were made while comparing the different profiles, the test results are qualitative rather than quantitative. The bottom line is that the difference between the canonical S-Curve ($\gamma = 1$) and the sinusoidal profile is perceptible but far from dramatic. Probably the major advantage, apart from marginal reductions in servo positioning errors, lies in the procedural simplicity of the implementation.

A word about the test implementation: In a i486–DX4 type processor at 66 Mhz (with FPU integrated), running an ISR (interrupt service routine) that feeds a servo controller at a rate of 250 Hz, under a multitasking OS (Linux), there is not an appreciable difference for the computational load of calculating any of the profiles reviewed.

Also available as a complement of these procedures is the solution to the opposite problem: For a given travel time, What is the required parameter change (velocity in this case) that satisfies the motion conditions?.

This can be useful when synchronizing motion in several axes, or in the case when the calculated Tt in Initialization has to be adjusted upwards to the nearest multiple of the sampling period. In this case the parameters to be given are:

- Am ≡ Maximum Acceleration peak value allowed.
- Tt ≡ Elapsed time required for the motion.
- Throw ≡ The travel distance (positive or negative).
- Vm ≡ The original Maximum Velocity allowed (absolute value) for validation of the Tt provided.

The procedure verifies the validity of the parameters and finds in closed form (a quadratic) the result: Two values of velocity that, when adopted as Vm, will work as a solution to the problem of traveling the **Throw** in **Tt** seconds.

The Tt equation for the S–Curve is

$$Tt = \frac{Yf}{Vw} + \frac{Vw}{Am} \cdot (1+\gamma),$$

and for the Sinusoidal profile

$$Tt = \frac{Yf}{Vw} + 2 \cdot \frac{Vw}{Am}.$$

Both formulas are similar and, for the purpose of this analysis, a convenient simplification consists in using only the S–Curve formula and regarding the Sinusoidal profile case as an S–Curve with $\gamma = 1$.

The pertinent solutions are [2]

$$V_1 = \left(\frac{Am}{1+\gamma}\right) \cdot \frac{1}{2} \cdot \left(Tt + \sqrt{Tt^2 - 4 \cdot \left(\frac{1+\gamma}{Am}\right) \cdot Yf} \right),$$

$$V_2 = \frac{2 \cdot Yf}{Tt + \sqrt{Tt^2 - 4 \cdot \left(\frac{1+\gamma}{Am}\right) \cdot Yf}}.$$

V_1 ≡ The solution that minimizes (or cancels) the constant velocity zone.

V_2 ≡ The solution that maximizes the constant velocity zone.

Both solutions are valid, but only V_2 guarantees the security condition $V_2 \le Vm$.

Summary Table of Velocity Profiles

Velocity Profile Type	Normalized Transition Time (Ta)	Total Piece Wise Constructor	Normalized Jerk Value	Jerk Shape	Normalized Peak Power per Unity of Mass
Trapezoidal $\gamma = 0$	1.00 (Reference and lowest)	3	∞	4 Impulses	1.00 (Reference)
S–Curve $\gamma = 0.25$	1.25	7	4.00	4 windows	0.88
S–Curve $\gamma = 0.50$	1.50	7	2.00	4 windows	0.75
S–Curve $\gamma = 0.75$	1.75	7	1.33	4 windows	0.63
S–Curve $\gamma = 1.0$	2.00	7	1.00 (Reference and lowest)	2 pairs of linked windows	0.54 (Lowest)
Sinusoidal	2.00	3	1.57	2 windowed sinusoids	0.63

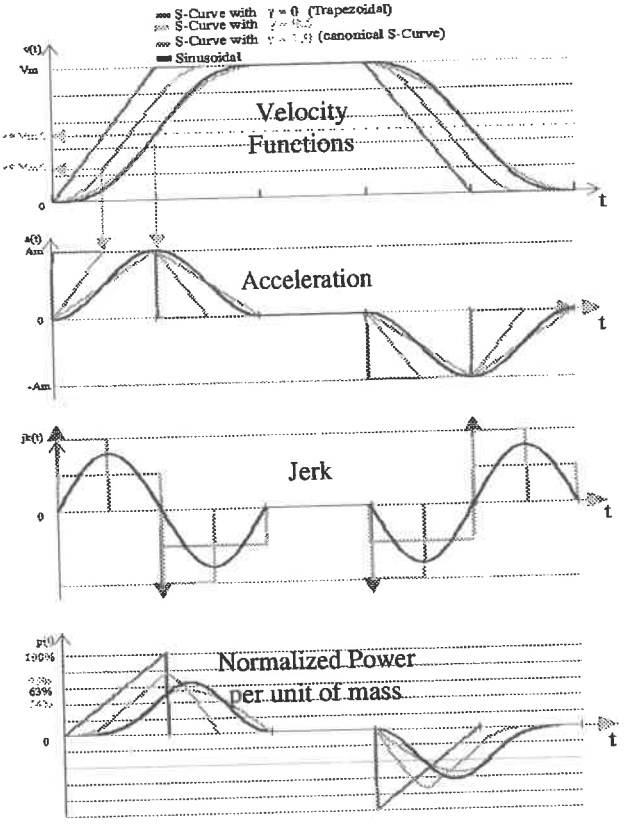

Final Comment

Contrary to the traditional methods, the Sinusoidal Profile requires computing power for the trigonometric evaluation (FPU, series expansion or lookup tables), but provides a simplified algorithmic implementation.

1.-"The price of age," The Economist, Dec 23rd 2000, pp 91-94.

2.- Press, W.H. et al,"Numerical Recipes", 2nd ed., Cambridge UP, New York, 1995.

Enhancing Precision Manufacturing Through In-Situ Metrology

Shane C. Woody & Stuart T. Smith
Center for Precision Metrology, University of North Carolina at Charlotte, Charlotte, NC 28223

Introduction

Production methods for generation of artifacts with nanometer level dimensions and tolerances include modifications of traditional tools plus the development of new manufacturing methods. These can be classified as reductive and additive. Reductive methods are represented by conventional machining, abrasive processes (belt and rigid wheel grinding), third body abrasion (including chemically assisted), etching, electrolysis and ion beams. Additive methods include the broad variety of deposition processes such as electro deposition, plasma sprays, sputtering, e-beam and magnetron deposition etc. We are concerned in these investigations with the identification of the optimal means of increasing precision and accuracy of manufactured components produced using multiple processes. In particular, we will be seeking to enhance the manufacturing precision of reflective optical elements. Currently, these are made by diamond turning and polishing of mandrels, replication by deposition and removal of metallic coatings followed by a final sputtering of highly reflective coatings (iridium).

Manufacturing processes aim towards the minimization of the ratio of volume error of the component to the removal/deposition rate. Precision and accuracy of manufacture is, ultimately, limited by the repeatability of all processes that impart features over spatial wavelength scales relevant to the functional geometric tolerances. For example, polishing can be used to create surfaces with a superfine surface finish (short surface wavelengths) and nanometer level dimensional control of surface removal. However, it is not possible to simultaneously control short and long-range (or profile) features on the surface. This limited ability to control spatial wavelengths and low removal rates lead to a low manufacturing 'efficiency'. On the other hand, diamond turning can be used to produce geometric features with short wavelength geometry limited to the tool's tip dimensions over spatial wavelengths comparable to the working volume of the machine. However, the resolution of the tool control is limited by both the resolution of the laser scale and the repeatability of the slide error in each axis. Currently, the diamond turning machines available to this project use laser scales with a resolution of 2.5 nm, a slide straightness of the order 0.25 μm per 100 mm of traverse, display scale resolution of 10 nm and axial alignment error of the order of a few arc seconds. Typically, temperature control to within ±0.1 C is maintained during a machining cycle.

In this paper we present a modified diamond turning center that includes a precision tool servo for nanometer level control and a profilometer for in-situ metrology, Figure 1. In a typical machining cycle the specimen will first be cut to the nominal profile but over-size. The specimen will then be measured using the profilometer and deviations from the desired shape computed. These errors will then be removed by

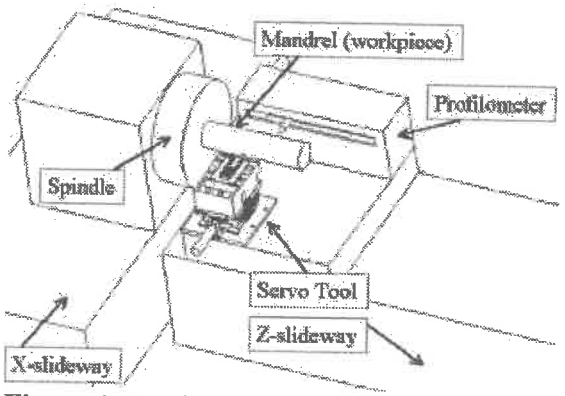

Figure 1: Modified diamond turning center

the fine tool servo in a second and final cut to net shape, this second cut being of the same depth as the first.

Technical approach

Traditionally, at higher precisions, dimensional metrology has taken place in temperature and humidity controlled laboratories, often housed away from the manufacturing process. Even for routine measurements it is often necessary to remove the work-piece from the machine or, at best, stop the process. Within this project, a portable, robust surface profiler will be designed and built. This will utilize technologies previously developed[i] for the Nanosurf family of profilers[ii]. In particular, we plan to exploit the precision motion slideway design integrated with newly developed drive couplings[iii] and stylus probe systems[iv]. Such a profiling instrument will enable a study of the implementation of local error correction using measurement at the limits of precision[v] as well as an assessment of the issues associated with the integration of nanometer metrology into manufacturing processes.

In an effort to improve the precision of machine tools, error compensation is commonly used. Typically, the errors between the position measured by the machine scales and actual position of tool relative to the specimen are mapped using a metrology system of higher precision and accuracy. This information is then used to develop (usually) software compensation that operates by effectively 'lying' to the controller so that the control set -point corresponds to the 'true' desired position. Clearly, such a compensation strategy is limited to the resolution and stability of the motion control and measurement capability of the machine. However, the potential compensation is limited only to the repeatability of the machine. Hence to exploit this potential it is necessary to either increase the precision of the scales and controller or add an additional, fine motion system. It is this latter approach that is currently under development.

Additionally, the relationship between the repeatability of the machine and the error compensation is not clear. In general, it is known that a conventional machine tool slide can exhibit nanometer level repeatability over short traverse ranges for short periods of time. However, under closed loop position control the machine tool will be working to compensate additional errors of the measuring scales, primarily measurement noise. Cl early, the resolution of the scales and the repeatability of successive cuts are independent. Hence it is possible that, while active compensation can reduce errors, it is possible that this also randomizes the residuals. This random error may be greater than the original repeatability of the uncompensated machine. Such issues will be assessed using the profilometer developed in this study.

To assess the limits of precision in diamond turning, it is necessary to calibrate the process using a method of considerably higher accuracy and precision. The precision of the profilometer will be derived from the slideway and probe technologies. Accuracy of the profiling capability will be assessed using reversal methods[vi]. These will be implemented in-situ using a probe mount design that enables precise 180 degree rotation of the stylus while maintaining lateral registration between the straight edge and stylus tip.

Hence, for the diamond turning and post processing of x-ray optical elements, this study will assess the necessary conditions for inter-process compensation in terms of process stability and repeatability.

Other technical advances that will be necessary within this project are the implementation of cascade, or 'nested' controllers in precision machines and the design of low cost, high precision dedicated machine tools.

In summary, the main attributes of this approach to error compensation are

1. The effects of workpiece distortion due to machining forces are included in the compensation.
2. It may be possible to achieve a precision governed by the repeatability of the slideways therefore representing the physical limit.
3. Repeatability may be enhanced by using fewer closed loop controls.

Design of a stylus profilometer

This instrument will be used to measure the profile of components throughout the manufacturing process. For replicated optics, it will be necessary to measure surface profiles of both the replicating mandrel during diamond turning and post polishing, the replica after deposition and separation and the final surface form after finish coatings (iridium) have been applied. To use this profiler at all stages in the manufacturing process, it needs to be both portable and sufficiently robust to function satisfactorily at the location of each process.

Conceptually, this design will follow that of most other profiling systems in which the stylus probe is traversed along a datum surface that is aligned to be parallel to the specimen [vii]. During this traverse the stylus is maintained in contact with the surface and va riations in this motion are measured and interpreted as the surface profile. For an ideal traverse and stylus probe the output signal will be an accurate representation of the surface profile of the interface between probe tip and specimen. If the interface pressures and frictional forces are low, the measured profile will correspond to the free surface of the specimen. In practice, these requirements can be adequately satisfied to produce profile measurements with sub-nanometer repeatability. Key components of such a profilometer comprise the slideway, drive mechanism and probe head. These are briefly discussed in the following paragraphs.

Slideways used in the Nanostep family of profilometers have also been applied to larger measuring machines as well as the bearing system on the ultra-precision grinding machine Tetraform[viii] with unsurpassed performance. While this clearly exhibits the ability to provide nanometer level repeatability with high stiffness and load bearing capacity, this bearing technology has not been applied to the design of robust metrology systems for integration within manufacturing environments. In this design, the carriage supporting the stylus probe will traverse over a vee slide made up of two optical flats. A composite polymer/bronze bearing[ix] will be used to maintain a constant height during motion. A motor-gearbox combination will drive a feedscrew which in turn will be coupled via a nut to the carriage. Motion of the nut will be transmitted by a patented decoupling mechanism to attenua te motion errors of the drive[x]. When used to assess diamond turned mandrels, it may be desirable to use the *z*-axis traverse to drive the carriage, again via the decoupling mechanism. A linear scale providing 50 nm resolution over 100 mm traverse will be used to measure motion of the carriage relative to the instrument frame.

Dual probes will be necessary to assess both surface finish and profile. Surface finish will be assessed using a metrological constant force probe based on a measuring principle similar to that used in atomic force microscopes[xi]. Profile measurement will be carried out using a simple stylus arm on a flexure pivot. The difference between the two measurements is the tip radius (1.0 μm for surface finish 0.5 mm for profiling) and sensor bandwidth (200 and ≈ 10 Hz respectively). In both cases, displacement of the probe tip will be measured using custom-built capacitance gages utilizing a digital lock-in amplifier and ratio transformer preamplifier. Each probe will be fastened onto the carriage with a mount that enables reversal of the probe so that standard

reversal techniques can be applied to implement slideway error separation[xii]. Probe calibration will be performed using high resolution laser interferometry developed at UNCC[xiii].

Designed into the instrument frame will be kinematic mounting points so that the complete instrument can be readily moved and relocated within any process.

Development of a tool translation mechanism

In general, as currently developed, the servo tool provides a translation range of 3 μm with a resolution of 1 nm[xiv]. Adapting a high precision servo tool and profilometer system into a diamond turning center is a challenging design task. Considering that the workpiece and servo tool may be doused with an oil or air bath, a thin walled environmental shell is utilized to prevent any oil from entering the carriage chamber and disrupting the electronics, Figure 2.

A monolithic, tool translation flexure, Figure 3, rigidly mounts to the top of a vertical carriage platform. Four leaf flexures are designed on each side of the tool mount to provide high axial stiffness and moderately high resonant frequency. Additionally, there are two further flexures underneath the carriage that are squeeze clamped to the platform. Consequently, the base flexures restrict the carriage from tilting about the X axis. A combination of conventional milling and wire EDM were used to produce the monolith. The tool carriage is designed with approximately 4 MN m^{-1} stiffness and a 500 Hz natural frequency. A piezoelectric (PZT) stack actuator provides a single linear motion and uses capacitance gauging for closed loop control, Figure 4. In this design, the capacitance gage directly measures the local tool motion due to PZT expansion or contraction.

A piezoelectric (PZT) stack actuator provides a single linear motion and uses capacitance gauging for closed loop control, Figure 3. The PZT stack has a maximum range of 17 micrometers with an applied potential of 150 V. The use of capacitance sensor for closed loop control significantly reduces the hysteretic effects. In this design, the capacitance gage directly measures the local tool motion due to PZT expansion or contraction. The capacitive sensor consists of two aluminum coated glass slides. The base glass slide is approximately 1 mm in thickness and the central region is etched with a 20 μm step prior to coating of aluminum

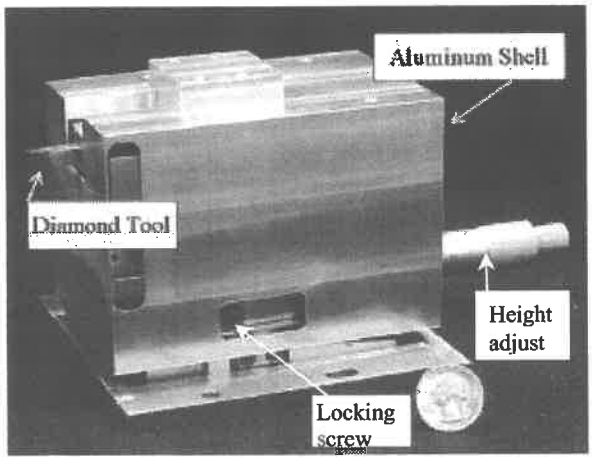

Figure 2: Assembled fine tool translator with aluminum cover

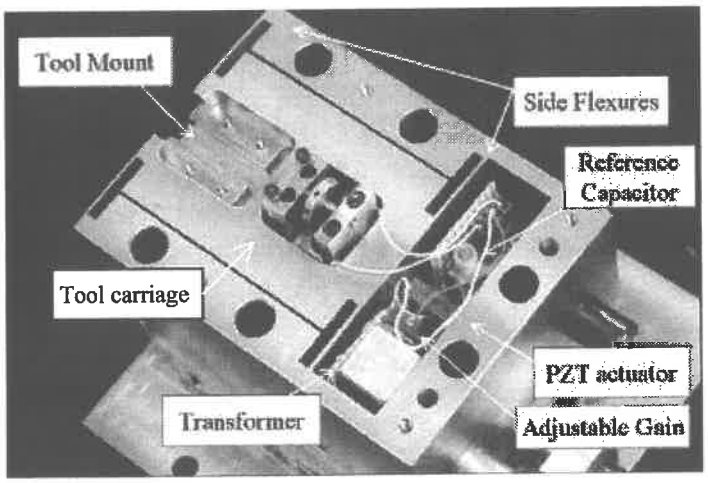

Figure 3: Tool translation flexure and capacitor electronics

electrodes. A second slide bridges across the base plate and epoxy is applied to each corner. Glass slides of 0.2 mm thickness and aluminized on one face are chosen as the top slide to

provide low stiffness. A ruby sphere is bonded with epoxy to the top slide to provide a contact point for transferring motion of the carriage to displacement of the thin glass slide electrode. The capacitance assembly mounts into a flexure tilt stage. A differential screw accommodates a fine adjustment mechanism and, with feedback, this can be controlled to better than 2 μm. The complete capacitor assembly and fixture is placed through a clearance hole in the tool carriage and bolts to the carriage platform. Fine differential adjustment is then utilize d to bring the ruby sphere of the capacitance sensor into contact with the tool carriage. The contact is aligned with the diamond tool axis in order to minimize Abbe offset.

Performance Testing

The servo tool has been calibrated using a Hewlett Packard laser interferometer. During calibration, the demodulated capacitance voltage is compared to the laser displacement reading and a second order polynomial is used to fit the measured data. Next, the tool is tested to determine the fastest response time or limiting bandwidth. The response time is determined from the output from the capacitance gage when a step demand is fed into the PID controller. The servo's settling time is optimized by adjusting the three terms of the PID controller while monitoring the response in real time. Currently, the servo's optimal settling time is determined to be 12 ms, Figure 4.

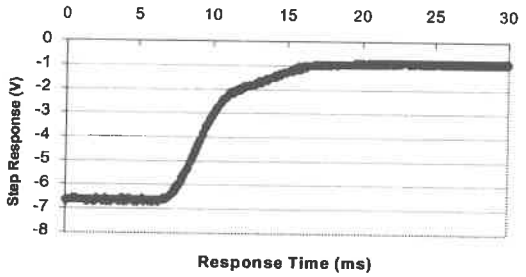

Figure 4: 12ms servo settling time under closed loop control

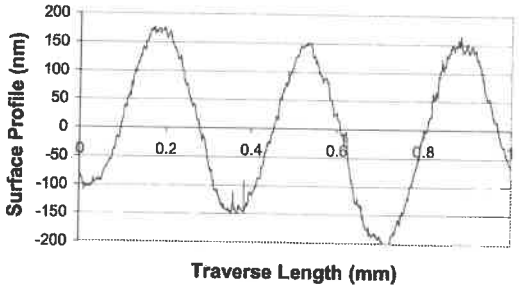

Figure 5: Sinusoidal profile of 300 nm pk-pk amplitude

Recent investigations include cutting step and sinusoidal profiles across the face of 4" diameter aluminum blanks. First, the tool servo is mounted into a Precitech diamond turning center with the PID controller and Capacitor lock-in located to the side of the Z-axis slide. These tests involve first facing the sample piece in several cutting passes until a P-V surface finish of between 50-100 Å is achieved. In the final pass, the *Z*-axis slide is translated towards the blank for a nominal depth of cut of 0.5 μm and *X*-axis feed is slowed to 2 mm per minute. A sample is cut with a sinusoidal profile having a wavelength of 0.33 mm^{-1} successive increases in depth of 20 nm after three cycles, Figure 5. A Talystep was used to measure the subsequent surface profile. Current sample measurements indicate minimal overshoot during the tool's step response. Presently, less than 60nm amplitudes have been produced, figure 6.

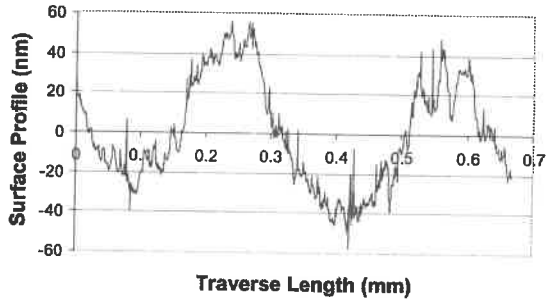

Figure 6: Profile of sinusoidal profile≈ 60 nm pk – pk amplitude.

Design of component specific machine tools

Currently, the diamond turning machines to be used in this study have been designed for commercial manufacture of components of arbitrary geometry. This versatility, while desirable from a commercial standpoint, reduces the stiffness, dynamic response and thermal/temporal stability of the machine tool and is not necessary to produce simple shapes. Per chance, the profiling system linear bearing and fine tool translator also represent the key components for a compact diamond turning machine capable of producing replication mandrels. An ultimate goal is the design of fast, stiff, compact, inexpensive, component specific diamond turning machines. Such machines would comprise a minimum number of axes each shaped to translate the tool in specified paths with nanometer level error compensation.

References

[i] Lindsey K. and Smith S.T., UK Patent GB 2 221 962 B, U. S. A. Patent No. 4 944 606 Precision motion slideways, 20 pages (also filed in the USSR and Denmark)

[ii] Lindsey K., Smith S.T. and Robbie C.J., 1988, Sub-nanometer surface texture and profile measurement with 'Nanosurf 2', *Annals of the CIRP*, **37**, 519-522.

- Garratt J.D. and Bottomley S.C., 1990, Technology transfer in the development of a nanotopographc instrument, *Nanotechnology*, **1**, 28-43.
- Leach R.K., 2000, Traceable measurement of surface texture at the National Physical Laboratory using Nanosurf IV, *Meas. Sci. Technol.*, **11**, 1162–1172.

[iii] G. Singh, C. Hsu and Smith S.T., A decoupled nut mechanism, patent filed 101-98

[iv] Howard L.P. and Smith S.T., 1994, A metrological constant force profiler, *Rev. Sci. Instrum.*, 65(4), 892-902

- Chetwynd D. G., Liu X. and Smith S.T., 1996, Controlled force stylus displacement sensor, *Precision Engineering*, **19**(2-3), 105-111

[v] Bennett J., Elings V., Recent advances in the profiling of optical surfaces, *Appl. Optics*,

[vi] Campbell A., 1995, Measurement of lathe z-axis straightness and parallelism using a flat land, *Precision Engineering*, **24**, 372 – 379.

[vii] Smith S.T. and Chetwynd D.G., 1992, *Foundations of Ultraprecision Mechanism Design*, Gordon and Breach, London, 348 pages, ISBN 2-88124-840-3, fourth printing 1999

[viii] Lindsey K., 1991, Tetraform grinding, **SPIE**, 1573, 129-135.

[ix] Smith S.T., Harb S. and Chetwynd D.G., 1992, Tribological properties of polymeric bearings at the nanometer level, *J. Phys. D.*, **25**(1A), 240-248

[x] G. Singh, C. Hsu and Smith S.T., A decoupled nut mechanism, filed 101-98

[xi] Howard L.P. and Smith S.T., 1992, Long range constant force profiling for measurement of engineering surfaces, *Rev. Sci. Instrum.*, **63**(10), 4289-4295.

[xii] Evans C.J., Hocken R.J. and Estler W.T., 1996, Self-calibration: Reversal, redundancy, error separation and 'absolute testing', *Annals CIRP*, **45**(2), 617 – 631.

[xiii] Badami V.G. and Patterson S.R., 2000, A frequency domain method for the measurement of nonlinearity in heterodyne interferometry, *Precision Engineering*, **24**(1), 41 – 49.

[xiv] Woody S.C. and Smith S.T., A Lathe Tool Translator for Form Error Reduction in Diamond Turning, *Proc. of ASPE, 2000*, **22**, 256-259.

CONTROL OF A DYNAMIC FLEX-STAGE

Pai-Hsueh Yang, Brian J. Alamo, John McCoy, and Gerry B. Andeen
Ion Diagnostics, Inc., 2238 Martin Avenue, Santa Clara, CA 95050

I. Requirements and Strategy

The stage was developed for the needs of multicolumn electron-beam lithography. An array of e-beam columns is placed above the wafer to be written. The stage moves the wafer under the columns while the e-beams write simultaneously over the entire wafer.

The path specified is a pattern similar to plowing a field beneath each e-beam so writing from each column corresponds to the column spacing, approximately 40 mm X 40 mm. The speed during writing is 100 mm/s and the acceleration during stage turnaround to make another pass at a distance of 0.02 mm from the first pass is 0.5 G. Nanometer accuracy of beam placement is required. The requirement on stage position is to maintain sub-micron accuracy of all points on the wafer in three-space and to measure and report the deviation from the desired trajectory. The beams can then be deflected to achieve the desired accuracy in the horizontal plane. The micron requirement is sufficient in the vertical because of the large depth of focus of electron beams.

Although it seems straightforward to measure and correct to nanometer accuracy, it is difficult because of latency in the reporting of position. By the time the error can be reported, the moving stage is already hundreds of nanometers beyond. Very smooth (noise free) motion of the stage is essential so that the current position of the stage can be predicted from prior measurements.

Our design and control strategy was to have the columns and wafer connected only by the measurement-control system, not by a rigid structure. We designed a very stiff writing-measuring structure, mounted the structure at a low natural frequency in a vibration free environment, and then positioned a floating six degrees-of-freedom stage so as to follow the trajectory relative to the writing-measuring equipment. This approach is a departure from the more common practice of mounting the stage and writing equipment on a common base.

Complicating factors due to the electron beams design included high-voltage isolation of the stage, ultra-high vacuum compatibility, and a low magnetic-field environment.

II. Stage Design

IIA. Flex Joints

Stage designers have probably always wanted to avoid sliding or rolling tracks. The relatively small overall motion requirements made it possible for us to do just that, to use joint elements that bend or flex as opposed to sliding. The key advantage of a flex-stage in our application is smooth and predictable motion.

In the design achieved, shown in the sketch of Figure 1, the stage is supported on three legs having flexing joints at their ends. For kinematic reasons, one of the ends of each rod can have a universal joint kind of behavior while the other must provide three degrees-of-freedom. The long legs provided high voltage standoff as well as the range of motion desired with only small joint flexure.

The stage standing on legs is unstable. It can fall in three ways; forward-backward, sideways, and twisting.

IIB. Horizontal Motors

Horizontal actuation of the stage is provided by four non-commutating linear motors located in 'wings' that provide for electrical isolation. Magnets for the motors are mounted in the walls of the vacuum chamber. Current controlled amplifiers provide electrical power for the motors. Because there is no contact between the stage and the chamber except the controlled force due to the current, the stage is isolated from chamber vibrations.

IIC. Vertical Motors

Each leg is positioned vertically by a voice-coil motor in parallel with a very low frequency spring, a Nano-K® passive vibration isolation device. A voice coil motor with current amplifier provides the same vibration isolation as the horizontal linear motors. Since continuous current, not desired in a vacuum environment, would be required to support the stage the low spring constant devices were added. Horizontal vibration anticipated at the base is insufficient to cause a harmful disturbance at the wafer level.

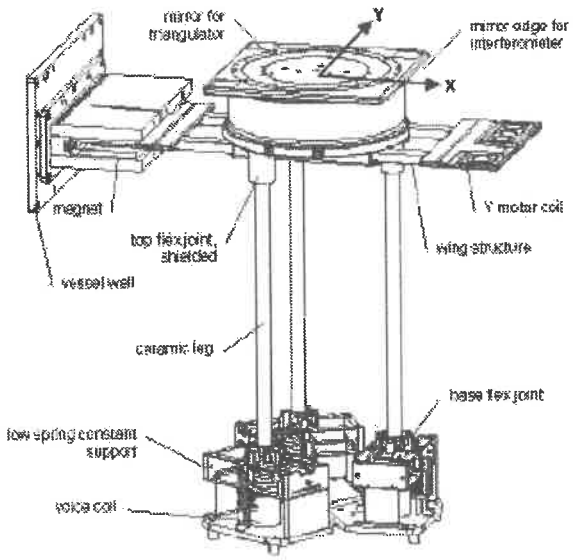

Figure 1 Schematic of the stage

III. Control System

IIIA. Measurement and Control Equipment

Three laser interferometers having 0.625 nm resolution are used for horizontal measurements and three laser triangulators with ~0.15 μm resolution are used for less critical vertical measurements. The interferometers measure the distance to the mirrored edges of the wafer holding plate. The triangulators provide an absolute measurement to mirrored surfaces adjacent to the wafer. Three accelerometers were placed on the writing-measurement structure at roughly the same positions as the interferometers to sense accelerations in the horizontal plane. The instrumentation platform (without e-beam columns) is shown in Figure 2.

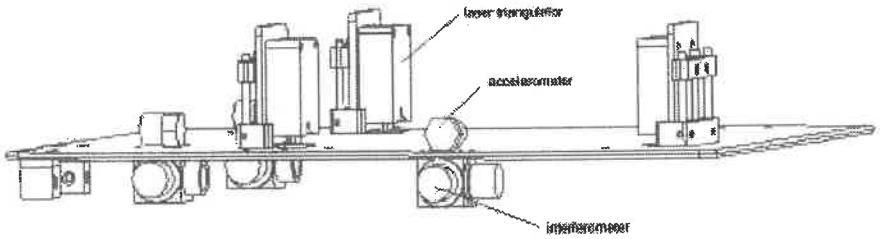

Figure 2. Instrumentation arrangement

During development, MatLab Simulink, and RealTimeWorkshop were used to generate the control code then executed in a dSpace DSP board.

IIIB. Trajectory Planning

The trajectory (position in time) of the wafer motion relative to the e-beam columns is known in advance. The desired position, velocity, and acceleration are calculated for each control step in Cartesian coordinates relative to the columns. In a calibration step after loading the precise orientation of the wafer to the stage can be determined. The calibration values can be added to the trajectory to define the desired position of the stage in time. Only the X and Y positions are intended to vary during operation. The other positions remain constant at the calibration values. Figure 3 illustrates the nature of the horizontal trajectory.

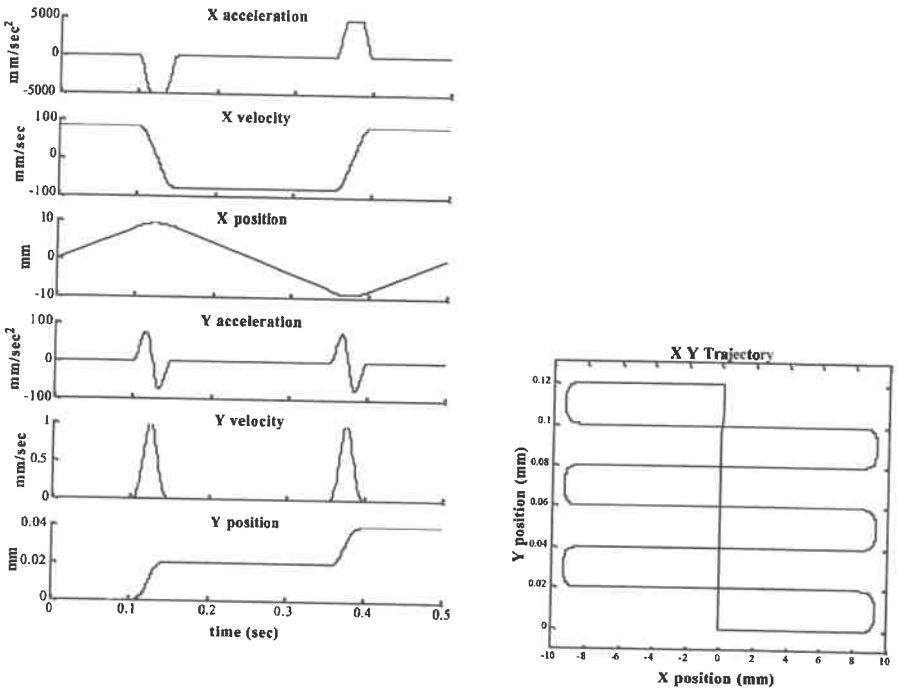

Figure 3. Horizontal trajectory (abbreviated)

IIIC. Coordinate Transformation and Control Distribution

We chose to execute the control in the coordinate system of the planned trajectory. Hence it is necessary to convert the measurements by a matrix multiplication. The horizontal and vertical measures were taken to be independent, e.g. the horizontal measurements depended only on the horizontal instrumentation, and the vertical on the vertical. These assumptions are valid as long as the rotations remain small. The matrix for the measurement transformations was calculated from geometric information.

Similarly, the control commands require a transformation to the motor commands by a matrix. The non-symmetric matrix required was approximated from geometric information. The transformation matrix can also be obtained by measuring the response to known signals to the motors. These measurements provide the matrix from the motors to the measurements that can be inverted (or pseudo inverted) to give the desired motor matrix. We found the geometric information to be sufficient, except for the case of large forces as will be discussed later.

IIID. Control Mechanisms

Several mechanisms were employed simultaneously as described in this section. A simplified schematic of the stage controls is shown in Figure 4.

IIID1. Servo Control

First a PID control was implemented. This control was capable of following the prescribed trajectory but was not expected to achieve the desired control accuracy. Its eventual function was startup, disturbance rejection, and safety (capture of a runaway).

IIID2. Gravity Compensation

In order to minimize the load on the servo, we elected to compensate for the gravity forces by providing restoring forces with the stage linear motors. Slowly moving the stage with the PID controller and observing the control signals determined the required compensation forces. We later expressed the data in a linear equation of the horizontal position measurements. Using the compensation, the stage could be moved with neutral stability to any

position within its range of motion. The effect was to create a floating body that was accelerated according to the control forces on it.

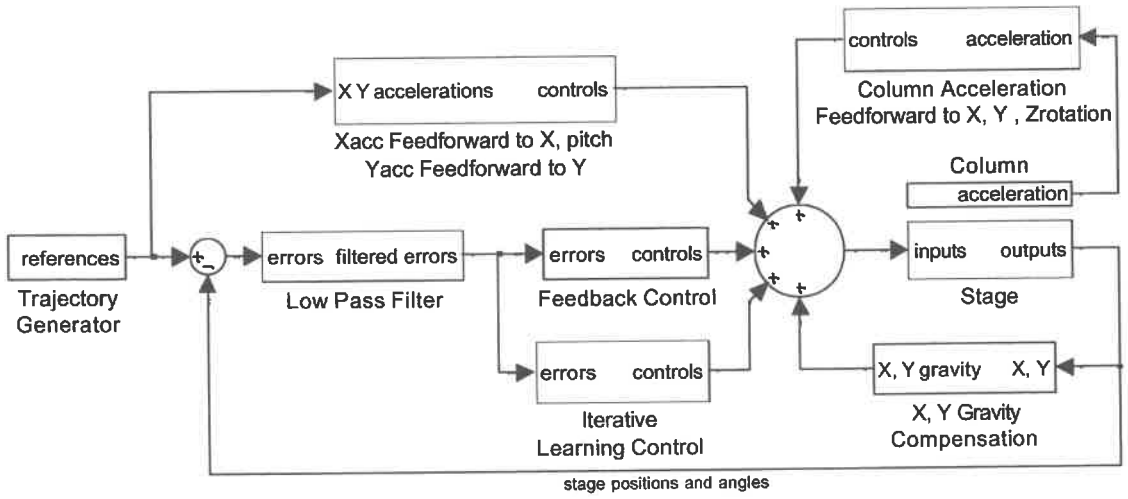

Figure 4. Control system block diagram

IIID3. Force Feedforward

The largest stage control is feedforward of the desired acceleration. The issues are sufficient knowledge of the details of the stage body with the location of the points of force application, and determining the appropriate gains. Indeed if this feedforward is done perfectly, the control problem is solved. Of course the discussion continues.

Trajectory acceleration

The stage trajectory is known in advance. The trajectory accelerations with the appropriate gain are the control values for the stage. These force commands can take over the major control of the stage from the servo, which would remain to provide small corrections.

The largest acceleration occurs during the stage turnaround, especially in the X (writing) direction. During the writing itself, the stage is coasting. Because the motor force vectors do not pass through the center of gravity of the stage, application of force causes rotation. While the purpose of the control distribution matrix is to account for this effect, our simple matrix did not do this. Our solution was to feed the X direction acceleration to the pitch (rotation about the Y axis) control with a gain tuned manually.

We also fed the absolute value of the X direction acceleration (with a tuned gain) to the height control to compensate for vertical forces generated in by the leg structure by the turnarounds.

Column acceleration

If the column structure is moving in the horizontal plane, the accelerations required to follow the movement can be measured and fed to the stage control. Once again the servo loop is relieved of the job of following, and now makes fine adjustments. The importance of this acceleration depends on the level of the column movement. An example of the importance in our experimental setup is shown in the traces of Figure 5.

IIID4. Learning Control

Learning is the primary mechanism for fine-tuning performance. The trajectory of the stage involves writing passes that are nearly the same as the previous pass, nearly repetitive. Thus, corrective forces are based on the errors observed during previous passes.

The correction control signal is maintained in all six axes for each control step in a back and forth pass of the stage. This correction signal is modified each pass according to the error in each axis. In our implementation, the correction signal was modified according to errors that occurred a few control steps later in the pass history. The filter to modify the correction signal was determined experimentally.

This learning control is capable of compensating for errors arising from nearly all sources.

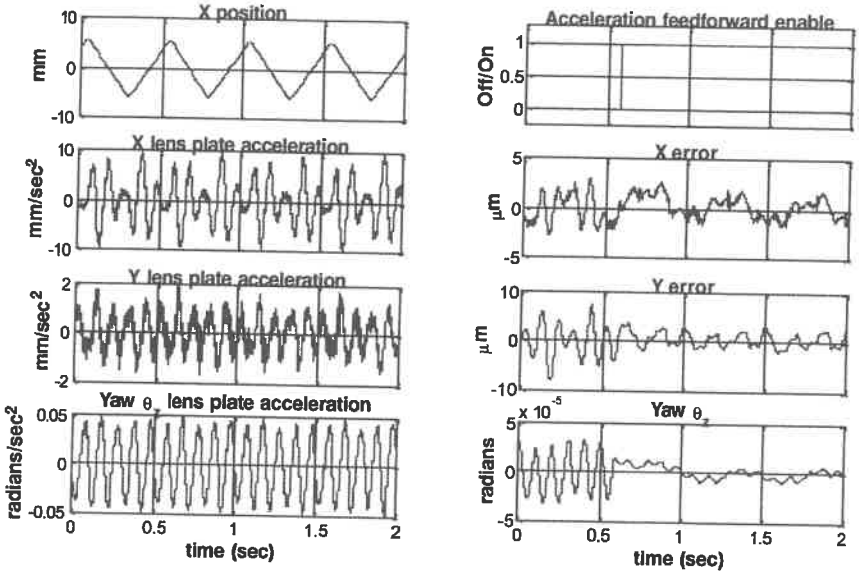

Figure 5. Feedforward correction of instrumentation platform movement

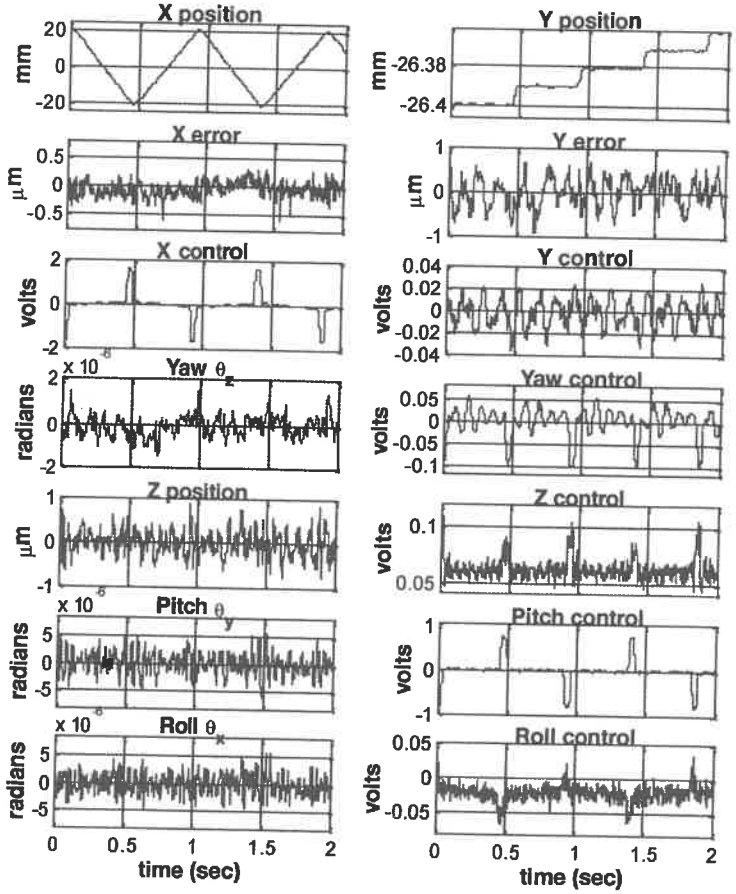

Figure 6. Stage performance

IIIE. Prediction

Because of interferometer reporting delay, it is necessary to predict the present deviation from the trajectory based on prior measurements. We employed a tapped delay line predictor. Experimentally we settled on to base the prediction on four previous values. As we are able to reduce noise in the system, we may increase the number of values increasing the prediction accuracy. The predicted trajectory error can then be used to deflect the electron beams thereby improving the overall system accuracy.

We tried using the predicted positions in the servo control, actually by adding a PD loop using predicted (present) error. The use of the predicted error significantly improved the performance of the servo itself, reducing the following error by more than half. However, the difference was negligible when the learning was also employed. The writing trajectory is sufficiently repetitive that the learning correction is able to compensate for any servo error.

IV. Performance

The stage performance in all six degrees-of-freedom is shown in Figure 6.

The components of the control signal for the X direction are shown in Figure 7.

As has already been suggested, the largest contributor to the control is the trajectory feedforward. The gravity compensation and lens plate acceleration feedforward play successively smaller roles. The role of repetitive control, however, is crucial in achieving the high performance required. Another way of looking at it is that the repetitive control allows us to be less than perfect in the other control employed.

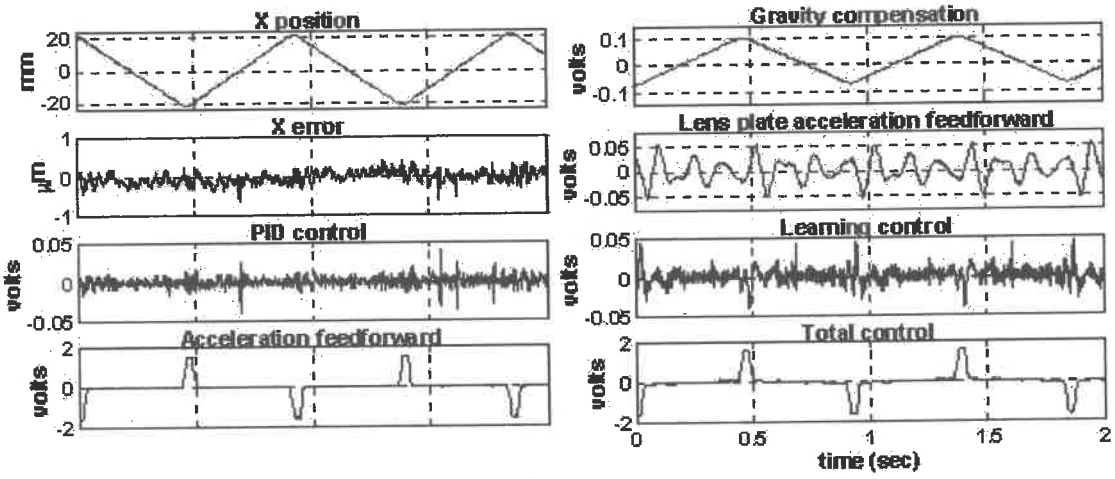

Figure 7. Components of the control signal

V. Acknowledgement

Martin Lee was a key contributor to the design of the stage and the flex joints.

DYNAMICS OF A HIGH PERFORMANCE WORKPIECE TABLE FOR ACTIVE CONTROL DURING PRECISION GRINDING

Y. Gao*, D. Zhang, and C. W. Yu

Hong Kong University of Science and Technology
Clear Water Bay, Kowloon, Hong Kong
*E-mail: meygao@ust.hk

Introduction

In the surface grinding process, a high speed work table motion is involved. In order to achieve active control of the process, the commands will include substantial amount of high frequency signals, which could not be sufficiently implemented by the wheel infeed system that typically has a small bandwidth. In order to solve this problem, a separate actuating unit will be required to support the workpiece in order to implement small but fast control actions. The workpiece actuating unit and the wheel infeed unit will work together under a composite control scheme [1], in which the advantages of the wheel infeed unit and the workpiece actuating unit are combined, such that both the large driving force capability and the fast active control can be achieved.

To realize the workpiece actuating unit to implement positioning functions that are fast but at the level of micrometers, a piezoelectric translator is used. Compared with the traditional feed mechanisms, workpiece micro-positioning tables using PZT are advantageous in resolution, static and dynamic stiffness, and most importantly, dynamic response. In precision positioning, this type of positioning tables has been used to generate compensation actions [2-9].

However, the tables have some inherent shortcomings such as hysteresis and parasitic motion that exists in multi-dimensional positioning. An additional one is overshoot. Using closed loop control and correctly tuned controllers, the hysteresis and parasitic motion could be solved. However, the overshoot problem during high speed positioning remained critical. It can be seen that high speed dynamic micro-positioning has not been achieved [2-9]. Typically, the settling time was 150ms and the resolution was 500nm [9]. Further improvement in high speed positioning accuracy is necessary.

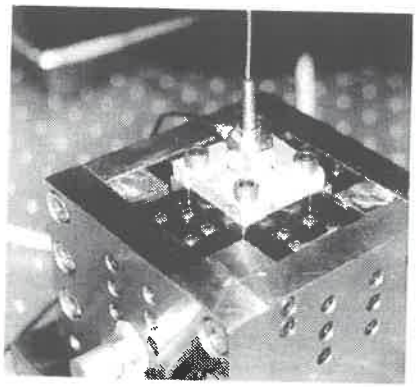

Fig. 1 Testing of the micro-positioning table

Design of the Micro-positioning Table

To achieve the above objectives, a new workpiece micro-positioning table has been developed (Fig. 1). It has a piezoelectric translator at its center to generate a displacement up to 47.7μm and a pushing force up to 1000N. This would give the workpiece table a working range of approximately 45μm after the removal of the effect due to the spring stiffness on the expansion range of the piezoelectric translator. The rigidity of the translator is approximately 17N/μm. The PZT is used to push the moving part in the workpiece table. Four

precision ball bearing guides are used to provide support for the moving part. This is to ensure that a good rigidity in the horizontal plane is maintained to reduce the possible deformation generated by the tangential grinding force and to reduce the parasitic errors. The moving part is used to support the top piece that in turn is used to mount a workpiece. The area of the top piece is 100x100mm.

Transient Displacement Models of the Workpiece Table

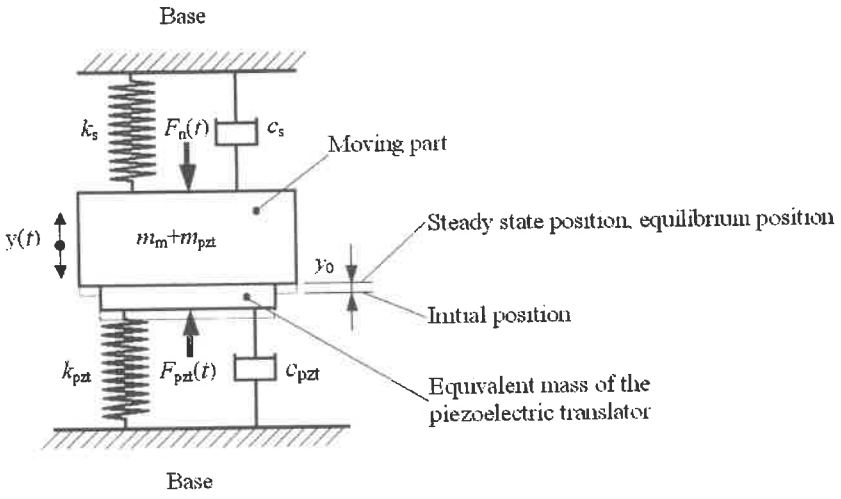

Fig. 2 Mechanics model of the workpiece micro-positioning table

In order to investigate the dynamics of the table, a mechanics model is used (Fig. 2). The moving part and the four springs are included. The PZT is modeled as a mass and spring system with a damping coefficient. $F_{pzt}(t)$ is the force generated by the PZT, $F_n(t)$ is the normal grinding force, $y(t)$ is the table displacement, and y_0 is the steady state displacement.

The mass-spring system will respond dynamically if it is subject to the piezoelectric driving force, $F_{pzt}(t)$, as the input to the system. The differential equation of the displacement $y(t)$ can be obtained as follows:

$$(m_{pzt}+m_m)\ddot{y}(t)+(c_{pzt}+c_s)\dot{y}(t)+(k_{pzt}+k_s)y(t)=F_{pzt}(t)-F_n(t) \tag{1}$$

where m_m is the mass of the moving part, m_{pzt} is the mass of the piezoelectric translator, c_{pzt} is the equivalent damping coefficient of the piezoelectric translator, and c_s is the equivalent damping coefficient of the springs used for preloading. To solve Eq. (1) for the above objectives, the normal grinding force $F_n(t)$ is assumed to be zero. Use the PZT force model during the expansion stage, noted as $F_{pzte}(t)$, the displacement $y(t)$ can be obtained. The acceleration of the table can then be obtained as:

$$\begin{aligned}\ddot{y}(t)=&\frac{A}{\omega_n}\frac{e^{-\zeta\omega_n t}}{\sqrt{1-\zeta^2}}(2\zeta\omega_d\cos(\omega_d t+\phi)+(1-2\zeta^2)\omega_n\sin(\omega_d t+\phi))\\&+NA\frac{e^{-\zeta\omega_n t}}{\sqrt{1-\zeta^2}}((2\zeta^2-1)\omega_n^2\sin(\omega_d t-\phi)-2\zeta\omega_n\omega_d\cos(\omega_d t-\phi))\\&\frac{LA}{\omega_n}\frac{e^{-\zeta\omega_n t}}{\sqrt{1-\zeta^2}}((2\zeta^2-1)\omega_n^2\sin(\omega_d t)-2\zeta\omega_n\omega_d\cos(\omega_d t))-\frac{GA}{R^2C^2}e^{\frac{t}{RC}}\end{aligned} \tag{2}$$

where ζ is the damping factor, ω_n is the natural frequency, and

$$2\zeta\omega_n = \frac{c_{pzt}+c_s}{m_{pzt}+m_m},\ \omega_n^2 = \frac{k_{pzt}+k_s}{m_{pzt}+m_m},\ A = \frac{1}{m_{pzt}+m_m}k_{pzt}d_{33}nk_{amp}v_0,\ \phi=\text{arctg}((1-\zeta^2)^{0.5}/\zeta)$$

$$G = -\frac{RC}{2\zeta\omega_n - \omega_n^2 RC - 1/RC},\ N=-G,\ L = \frac{2RC\zeta\omega_n - 1}{2\zeta\omega_n - \omega_n^2 RC - 1/RC}$$

where k_{amp} is the amplification factor of the piezoelectric drive amplifier, RC is the time constant of the piezoelectric translator circuit, d_{33} is the piezoelectric constant, n is the number of layers in the translator, k_{pzt} is the stiffness of the piezoelectric translator, and k_s is the stiffness of the springs for preloading. From Eq. (2), it can be seen that the acceleration of the table is proportional to the coefficient A that is proportional to the input voltage v_0 of the step command signal to the drive amplifier.

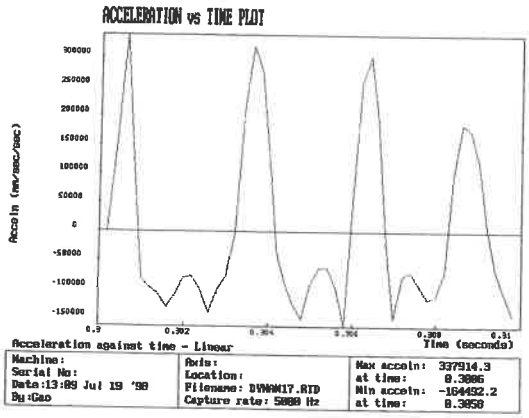

Fig. 3 Experimentally obtained acceleration to a step command signal

Experimental Testing and Discussion

In order to verify the performance of the developed micro-positioning table and the dynamic model, a series of experimental tests have been carried out. A Renishaw ML10/EC10 laser interferometer was used in the tests. To reduce the effect of external disturbance such as vibration, the tests were carried out on a Newport RS-2000 optical table with four I-2000 stabilizer vibration isolators. The environmental noise after the vibration isolation was approximately 10nm. Through a 12-bit D/A board, a computer generated a control command signal of a voltage range 0-10 volts. A PI E505 piezoelectric drive amplifier was used to generate a drive voltage of 0-100V to be applied to the piezoelectric translator. The average output power of the drive amplifier is 30W and the average output current is 300mA. The peak output current (<5ms) is 2000mA.The drive was selected to match the demand for the dynamic operation of the PI P-

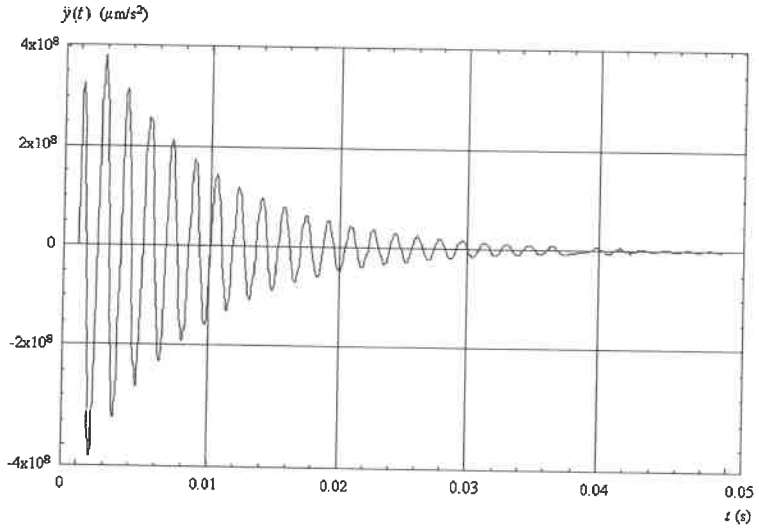

Fig. 4 Theoretical acceleration to the step command signal

840 piezoelectric translator with a current coefficient of 15μA/Hzμm.

From the tests, the table was found to have a resolution of 10nm after the noise effect is removed, a closed loop stiffness of approximately 400N/μm, a natural frequency of approximately 579.2Hz (Fig. 1), and a rising time of 400μs. Due to the high response speed to the step command, the acceleration was found to be up to 337914.3mm/s^2 that is 34.48 times of the gravitational acceleration (Fig. 3). Using Eq. (2), the theoretical acceleration is obtained (Fig. 4), where the theoretical maximum acceleration is found to be approximately 3.5x10^{8}μm/s^2. This result is quite close to the experimental result shown in Fig. 3, except the distortion at the bottom of the cycles due to the effect of detachment that is modeled separately, thus validates the dynamics model in Eq. (2).

Conclusions

A new workpiece micro-positioning table is developed to offer improvements in dynamic responses that are required for many high speed machining and motion applications. The piezoelectric translator is simplified as a spring and mass system driven by a piezoelectric force. A dynamic model is established to describe the acceleration of the table. The acceleration is mainly affected by the time constant of the drive amplifier and piezoelectric translator system, the damping factor of the spring and mass system in the workpiece table, and the input command signal to the drive. The model is validated by the experimental tests in which the maximum acceleration was many times of the gravitational acceleration.

References

[1] Y. Gao, Composite control for the surface grinding process, *Proc Int Manuf Eng Conf*, Storrs, Connecticut, USA, 1996, Freund Publishing, ISBN 965-294-121-2, pp. 157-159.

[2] J. Otsuka, S. Koshimizu, S. Hata, and A. Shimokohbe, An ultrafine motion table using piezoeletric actuator for ultraprecision grinding, *Int. J. Japan Soc. Prec. Engg.*, **30**(4), 1996, pp. 345-346.

[3] Z. Zhong and T. Nakagawa, Development of a micro-displacement table for ultra-precision machining and grinding for curved surfaces by the use of it, *Int. J. Japan Soc. Prec. Engg.*, **26**(2), 1992, pp. 102-107.

[4] V. Portman and B. Z. Sandler, High-stiffness precision actuator for small displacement, *Int. J. of Machine Tools & Manufacture* , **39**(3), 1999, pp. 823-837.

[5] K. Mizutani, T. Kawano, and Y. Tanaka, A piezoelectric-drive table and its application to micro-grinding of ceramic materials, *Precision Engineering*, **12**(4), 1990, pp. 219-226.

[6] M. Jouaneh and P. Ge, Modeling and control of a micro-positioning tower, *Mechatronics*, **7**(5), 1997, pp. 465-478.

[7] H. Goto and T. Sasaoka, Vertical micro-positioning system using PZT actuators, *Bull. Japan Soc. of Prec. Engg.*, **22** (4), 1988, pp. 277-282.

[8] P. D. Atherton, Nanometre precision mechanisms, *Measurement and Control*, **31**, 1998, pp. 37-42.

[9] J. D. Kim and S. R. Nam, Development of a micro-depth control system for an ultra-precision lathe using a piezo-electric actuator, *Int. J. Mach. Tools Manufact* ., **37**(4), 1997, pp. 495-509.

Lawrence Livermore National Laboratory ULTRA-350 Test Bed

David J. Hopkins, Timm A. Wulff, Keith Carlisle
Lawrence Livermore National Laboratory
P.O. Box 808, L-792, Livermore, CA. 94550

Abstract

LLNL has many in-house designed high precision machine tools. Some of these tools include the Large Optics Diamond Turning Machine (LODTM) [1], Diamond Turning Machine #3 (DTM-3) and two Precision Engineering Research Lathes (PERL-1 and PERL-II). These machines have accuracy in the sub-micron range and in most cases position resolution in the couple of nanometers range. All of these machines are built with similar underlying technologies. The machines use capstan drive technology, laser interferometer position feedback, tachometer velocity feedback, permanent magnet (PM) brush motors and analog velocity and position loop servo compensation [2]. The machine controller does not perform any servo compensation it simply computes the differences between the commanded position and the actual position (the following erro r) and sends this to a D/A for the analog servo position loop.

LLNL is designing a new high precision diamond turning machine. The machine is called the ULTRA 350 [3]. In contrast to many of the proven technologies discussed above, the plan for the new machine is to use brushless linear motors, high precision linear scales, machine controller motor commutation and digital servo compensation for the velocity and position loops. Although none of these technologies are new and have been in use in industry, applications of these technologies to high precision diamond turning is limited. To minimize the risks of these technologies in the new machine design, LLNL has established a test bed to evaluate these technologies for application in high precision diamond turning. The test bed is primarily composed of commercially available components. This includes the slide with opposed hydrostatic bearings, the oil system, the brushless PM linear motor, the two-phase input three-phase output linear motor amplifier and the system controller. The linear scales are not yet commercially available but use a common electronic output format.

As of this writing, the final verdict for the use of these technologies is still out but the first part of the work has been completed with promising results. The goal of this part of the work was to close a servo position loop around a slide incorporating these technologies and to measure the performance. This paper discusses the tests that were setup for system evaluation and the results of the measurements made. Some very promising results include; slide positioning to nanometer level and slow speed slide direction reversal at less than 100nm/min with no observed discontinuities. This is very important for machine contouring in diamond turning. As a point of reference, at 100 nm/min it would take the slide almost 7 years to complete the full designed travel of 350 mm. This speed has been demonstrated without the use of a velocity sensor. The velocity is derived from the position sensor.

With what has been learned on the test bed, the paper finishes with a brief comparison of the old and new technologies. The emphasis of this comparison will be on the servo performance as illustrated with bode plot diagrams.

Introduction

The ULTRA-350 is a horizontal diamond turning machine. The machine configuration is illustrated in Figure 1. The current machine design uses linear brushless motors for the actuators and high precision linear scales 2D (displacement and yaw) for the metrology sensors. The ULTRA-350 test bed was established to evaluate these technologies for use on the new machine. Previous in-house designed high precision LLNL diamond turning machines have used capstan drives with DC rotary motors as the actuators and Michelson type two frequency heterodyne laser interferometers as the metrology sensors.

The target performance for the new diamond turning machine is 25nm (pv) contouring accuracy and a 4 nm rms surface finish. Active real time control of the tool tip position will be used to achieve the stated accuracy. There are several elements of the machine design that together contribute to the final machine accuracy. Some of these elements include the metrology system, the temperature control system and the

servo system. An error budget can be developed to identify the impact of each of these sources. LLNL has high confidence in the ability to obtain very high precision temperature control (0.001 degree C or better) of the machine. As of this writing, the 2D linear scales for the metrology system are being evaluated for the required accuracy. This paper discusses the scales only in the context of motor commutation and machine servo compensation.

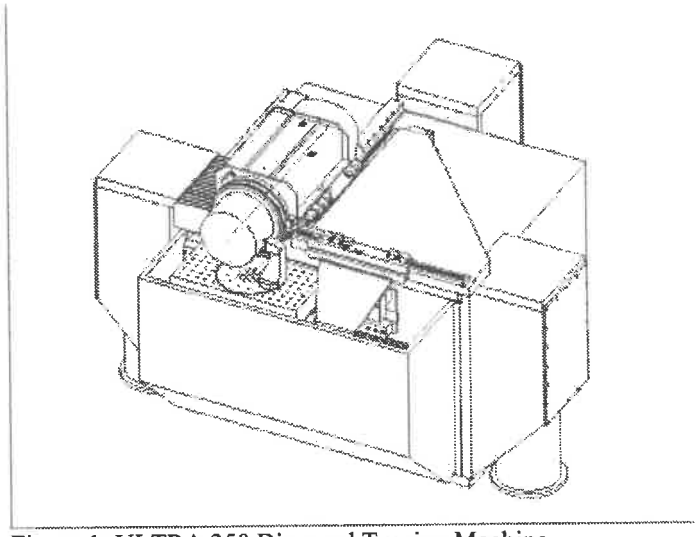

Figure 1. ULTRA 350 Diamond Turning Machine

The primary focus of this paper is to report on how the test bed servo system was setup, tuned and evaluated. The test bed helped answer many questions e.g. 1.) Will a linear motor drive system perform as well as a capstan drive system? 2.) What about the contrast between DC motor self-commutation and brushless motor controller commutation? What about the quality of the velocity feedback provided by a co-located motor tachometer verses velocity derived from only a position transducer? What about the use of a complete digital control system for velocity and position control loops as opposed to an analog only velocity loop and position loop analog compensation with digital command?

Contouring in diamond turning may require axis reversal. In the LLNL diamond turning machines, the analog velocity loop tachometer feedback provides damping and feedback when the rate of the position feedback (from the interferometer) is reduced to near zero. The tachometer loop also solves the problem of magnetomechanical resonance that occurs in capstan slide drive systems using DC torque motors. This effect reduces the torque (force) to velocity loop transfer function gain at frequencies below the resonance for small motor angular displacements (Figure 4). The effect is thought to be caused by the restoring torque when the rotor of the motor takes a magnetic set. The slide mass (M) along with the_ reflected spring stiffness (K) creates the magnetomechanical resonance The resonant frequency is $\sqrt{(K/M)}$. Data from the test bed has demonstrated nanometer level positioning (Figure 6) and extremely low speed (less than 100 nm/min) slide reversal without any observed discontinuities (Figure 5). The test bed high resolution position feedback and the use of controller high resolution sinusoidal motor commutation appears to provide sufficiently smooth slide motion with proper servo system compensation.

The majority of the system dynamics are enclosed in the velocity loop, The last section of this paper contrasts the open loop velocity transfer functions (torque or force versus velocity as a function of frequency) of several of LLNL diamond turning machines to that of the test bed.

Test Bed Components

Figure 2 is an abbreviated block diagram of the ULTRA 350 major components. The test bed is primarily composed of commercially available components. This includes a slide with opposed hydrostatic bearings, the oil bearing pump system, the PM brushless linear motor, a three-phase output, two phase input linear motor amplifier and the controller. The 2D linear scales are not yet commercially available, however for the purpose of this paper the second axis of the scale is not relevant.

From a servo system standpoint, the controller is the heart of the system. It provides the encoder resolution extension algorithm, the commutation algorithm and all the tuning parameters. Additional analog inputs and outputs have been activated as shown on the diagram. These inputs and outputs, when properly scaled can be used with a dynamic signal analyzer (DSA) for the purpose of setting and verifying the servo system compensation. There are several servo configurations that are allowed by this controller. The one shown in Figure 2 is the standard configuration minus feed-forward terms.

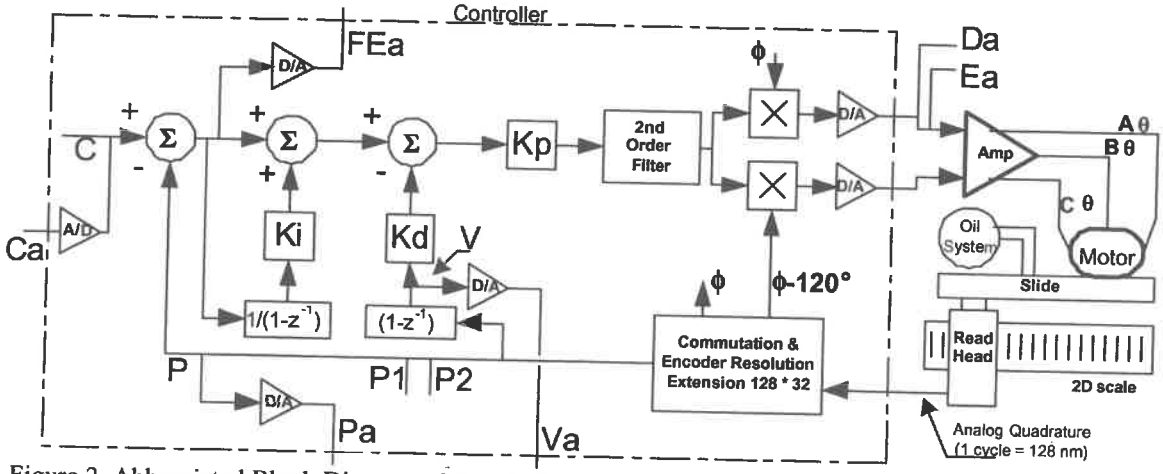

Figure 2. Abbreviated Block Diagram of the ULTRA-350 Test Bed

The amplifier is a linear (non-switching) torque amplifier (transconductance amplifier) with several modes of operation for motor commutation. In this system, the amplifier does not perform motor commutation. The amplifier, with the controller commutation algorithm and the high-resolution encoder feedback, provides the sinusoidal motor commutation. Sinusoidal commutation minimizes motor torque ripple. The amplifier internally develops the third motor phase output from the two input signals.

The motor is composed of a non-contacting forcer coil with rare earth magnet tracks. The ironless nonmagnetic forcer eliminates cogging and magnetic attraction.

The scale is 2D linear scale with 0.5 um line spacing. The read head provides a four times optical extension and generates a sinusoidal quadrature output with a period of 128 nm. The quadrature signal is fed to the controller where the extension algorithm provides for a "whole count" resolution of 1nm and with the 32 count "fractional" extension the position resolution is 0.031nm.

Setup, Tuning and Evaluation

Setup consisted of the necessary mechanical and electrical connections as well as the development of an E-Stop system to protect the operator and equipment of the test bed. A brake can be actuated to hold the slide in position in the event of an E-Stop. In addition, the encoder resolution extension and commutation algorithms and controller variables were setup and initialized.

There are three important loops in the control system of Figure 2. The first is the current loop that is part of the amplifier. The amplifier input voltage is converted to a current. This current is proportional to motor force and hence the motor acceleration. The second is the velocity loop. This loop encloses the third summing junction starting at the input to the gain term (Kp) and continuing through the system to the motor, slide, encoder and back to the negative input of the summing junction. This loop encloses the majority of electrical and mechanical dynamics of the system. It is the phase delay through this loop and the system dynamics e.g. resonances that limit the loop bandwidth. The third is the position loop. It encloses the first summing junction, the velocity loop and completes with the position feedback at the negative input of the first summing junction. The acceleration, velocity and position are the three state variables of this control system. As the acceleration loop is enclosed in the velocity loop and the velocity

loop is enclosed in the position loop each of the inner loops must have a greater bandwidth than the outer loops. The approach to servo compensation was to evaluate and or tune each of these loops individually. A dynamic signal analyzer (DSA) was used to accurately measure transfer functions (output/input) of system components and tune the loops. The analyzer provides a plot of gain and phase versus frequency. A bode plot.

The ultimate goal of this control system is to precisely control the position of the slide, reject slide disturbance forces and provide the highest static and dynamic machine stiffness. How well the control system meets the goals is a function of the position loop gain. Generally, loop gain increases at a specific frequency as the unity gain crossover frequency increases or as the loop bandwidth increases. Therefore, the higher the bandwidth, the better the system meets the goals. The acceleration or force loop is the most inner loop of the control system and therefore must have the highest bandwidth. As the motor force is directly proportional to the motor current, the bandwidth of the amplifier current loop is the first limit on system performance.

The amplifier was evaluated by measuring the closed loop transfer function of the output current versus input voltage. A current probe was connected to the A phase output of the amplifier and the input voltage was applied to the corresponding input. The other amplifier input was shorted to ground. (Note the amplifier is not connected to the controller for this test.) The motor is connected as the amplifier load and the slide (or forcer) is locked in place. This measurement indicated a current loop bandwidth of 4 kHz and a peaking in the response of less than 3dB at 2.38 kHz. The phase lag is less than 5 degrees at 300 Hz. This data indicates the amplifier should not limit system performance. Note the amplifier was evaluated at several different drive levels to observe any non-linearity. For example, crossover distortion will appear as a reduction in gain at low drive amplitudes.

The next step was to tune and evaluate the velocity loop. The controller has some auto-tuning capability but the optimum system performance will probably not be achieved with this method. Referring to Figure 2, the controller allows the position loop to be opened between P1 and P2. (The position loop had not been tuned so the loop should be left open at this point.) The open loop velocity transfer function can be measured by breaking the loop between Da and Ea and inserting a non-inverting unity gain summing amplifier. The DSA excitation signal is injected at one input of the summing amplifier and the signal at Da is connected to the other input. The open loop velocity transfer function is the ratio of Da/Ea. The tuning parameters Kd, Kp and the 2^{nd} order filter can then be adjusted with complete knowledge of the effects. Note that there are several points to make about this measurement. A.) The velocity loop is actually closed when this measurement is made but the connections to the DSA provide the open loop response B.) The position feedback device is an incremental encoder. Each time the system is started, the controller uses an algorithm that injects current into the motor causing motor motion and allowing the controller to compute the encoder-motor phasing for proper motor commutation. Upon completing this algorithm, the loop closes and the commutation angle is such that the maximum signal gain is available at Da. It is important that this condition exist in order to achieve the proper loop gain measurement. C.) With this controller topology, the velocity loop gain is a function of Kd, Kp and the 2^{nd} order filter. The initial value or gain for each of these was set to one. The gain of Kp or Kd was then adjusted upward until the DSA indicated the higher frequency resonances would drive the loop unstable. A filter was designed that would attenuate the high frequency resonances and allow an increase in velocity loop gain and bandwidth.

Figure 3 shows the magnitude of the velocity loop transfer functions. (Note the absolute magnitude of the individual transfer functions are not shown. The curves have been moved vertically to help show the shape of the transfer functions.) Curve A is the measured shape of the open loop velocity transfer function before the filter. Curve B is the 2^{nd} order filter transfer function designed to reduce the frequency components at 700 and 900 Hz and to reduce the peaking at 300 Hz. Curve C is the measured shape of the compensated open loop velocity transfer function. The phase plots are not shown but the loop gain with the filter can be adjusted to provide a velocity loop crossover frequency of about 85 Hz with a 45 degree phase margin. The bandwidth could be further extended if an additional 2^{nd} order filter was available. The current filter contributes almost 18 degrees of phase lag near the crossover frequency to attenuate the peaking at 300 Hz. If an additional filter was available, it could be designed to reduce the peaking at 300 Hz with minimal phase shift at the crossover. This would allow a decrease in the damping of the poles of the first filter and

hence an increase the phase margin at the crossover frequency. The loop gain could then be increased increasing the crossover frequency and velocity loop bandwidth.

The position loop is now easy to compensate as the dynamics have been addressed in the velocity loop. Once the proper scaling and offset of the D/A and D/As were set, the open loop velocity transfer function was found by injecting the DSA excitation signal at Ca and measuring the ratio of Pa/FEa. The position gain is the forward gain Kp. It was changed to increase or decrease the position loop gain but the product of the Kd and Kp must remain constant (the velocity loop gain). The Ki term and the Kp term were adjusted until the maximum crossover frequency could be obtained with a 70 degree phase margin.

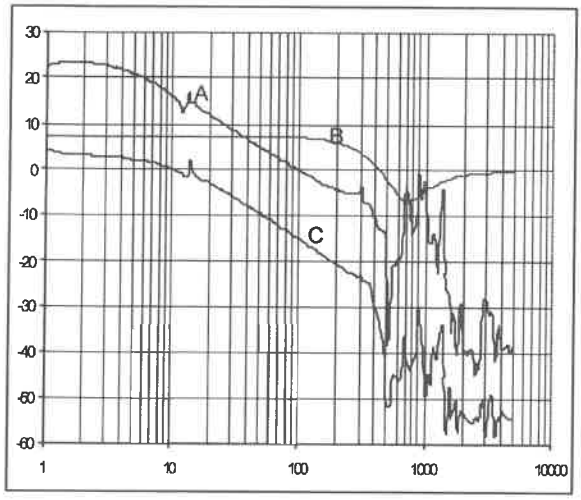

Figure 3. Velocity Loop Transfer Functions (TFs)

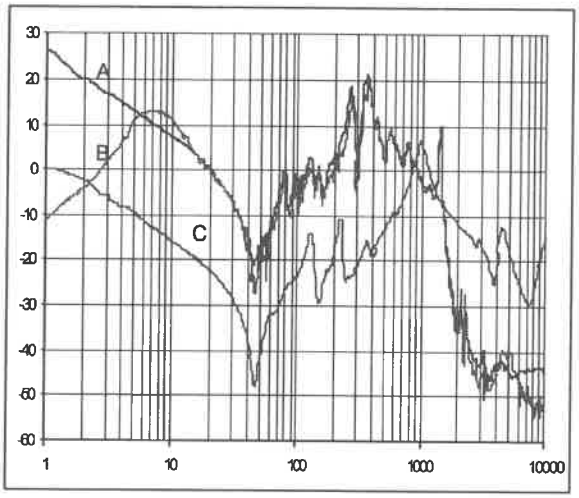

Figure 4. Capstan Drive Velocity Loop Transfer TFs

System Measurement Results

Figure 5 and Figure 6 indicate two important measurements taken from the test bed. Figure 5 is a strip chart recording of position versus time. It is approximately half of an S shape curve. Curve A is an analog voltage signal equivalent to the commanded position. Curve B is an analog voltage output signal from an LVDT amplifier with a probe in-line with slide travel. The bandwidth of this signal is limited to 3 Hz. Each vertical division is 6 seconds. Each horizontal division for the LVDT output is approximately 6.25 nm/div. The maximum rate of change of the curve is 100 nm/min. The curve clearly indicates smooth slide reversal.

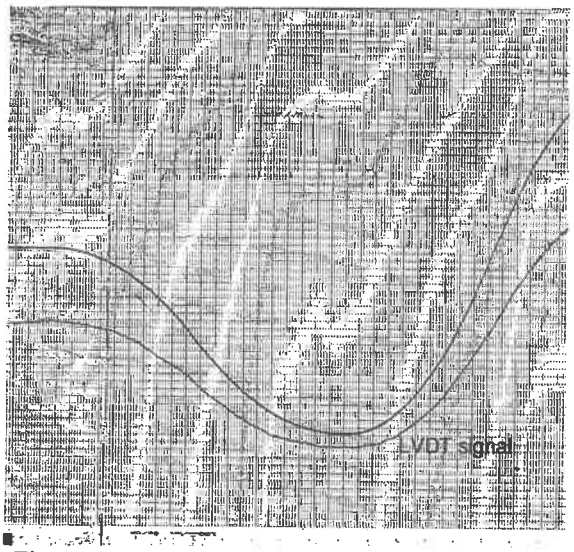

Figure 5. Low speed slide reversal

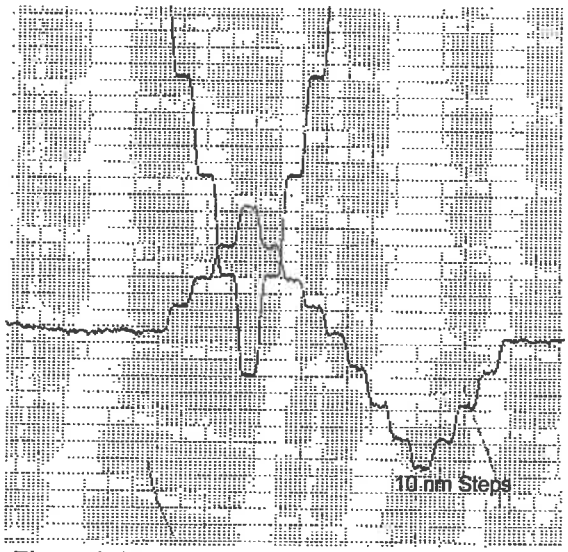

Figure 6. 10 nm steps

Figure 6 is the output of the LVDT when the slide is commanded to move in 10 nm steps. The larger steps in the chart are the inverse of the analog voltage equivalent to the commanded position step. (Only a small part of this signal is shown.)

Technology Comparisons

The dynamics of the open loop velocity transfer function between the linear motor drive system of the test bed and some of the capstan drive machines can be seen by comparing Figures 3 and 4. Figure 3 curve A is the open loop velocity transfer function of the linear motor system before compensation. Figure 4 Curve A is the LODTM open loop velocity transfer function before compensation. Figure 4 Curve B is also a LODTM transfer function but the curve demonstrates the magnetomechancial resonance that is apparent under small signal conditions. Figure 4 Curve C is an open loop velocity transfer function of DTM-3 before compensation. LODTM and DTM-3 are much larger machines than the test bed, however, PERL is a small 100mm diamond turning machine that has a similar characteristic signature of the two larger machine transfer functions. For PERL, the first deep notch is at 200 Hz and the corresponding resonance is at 600 Hz. Although the phase plots are not shown, it should be apparent that the dynamics of the linear motor test bed system are much easier to compensate than the capstan drive system. It also appears that bandwidth for a given system can be much higher with a linear motor drive system than a capstan drive system.

Summary

LLNL in-housed designed high precision diamond turning machines have used capstan drive technology, laser interferometer position feedback, tachometer velocity loop feedback, permanent magnet (PM) brush motors and analog velocity and position loop servo compensation. A new LLNL diamond turning machine is planned that will use brushless linear motors, high precision linear scales, machine controller motor commutation and digital servo compensation for the velocity and position loops. As of this writing, the linear scales are still under investigation for positioning accuracy, however the test bed has demonstrated these technologies will perform as required to meet the new diamond turning machine design goals.

This work was performed under the auspices of the U.S. Department of Energy by the University of California, Lawrence Livermore National Laboratory under Contract No. W-7405-Eng-48.

[1] Donaldson, R.R. and Patterson, S. R., "Design and Construction of a Large Vertical Axis Diamond Turning Machine", SPIE's 27th Annual International Technical Symposium and Instrument Display; Aug. 1983

[2] McCue, Howard K., "The Motion Control System for the Large Optics Diamond Turning Machine (LODTM)", SPIE's 27th Annual International Technical Symposium and Instrument Display; Aug. 1983

[3] Carlisle, Keith, Edson, E. L., "Design of an Ultra Precision Machining Facility: ULTRA 350", LLNL Center for Precision Engineering, 1999

Lorentz Motor With Stationary Magnets and Coils Applied in a 6-DOF Contactless Motion Stage

L. Jabben[1], **P.M. Overschie**
Delft University of Technology, Laboratory for Advanced Mechatronics, Delft, The Netherlands
A. Molenaar
SKF Engineering and Research Centre, Nieuwegein, The Netherlands
H.F. Van Beek
Emeritus Professor Micro-Engineering, Delft University of Technology, The Netherlands

Abstract

This paper presents a novel electro-magnetic motor principle that has all the advantages of Lorentz-type actuators and but works with stationary permanent magnets and stationary coils. Different candidate motor solutions will be discussed and the most attractive solution is selected.

This novel motor principle has been incorporated into a 6-degree-of-freedom (6DoF) Planar Active Magnetic Bearing (PAMB) design. The dimensioning of this motor type to the required specifications for this application is presented. Results of experiments on a modified existing setup show that the motor operates according to the presented theory. The results of our work indicate that future systems can benefit from more modular designs which take symmetry considerations into account. A sketch of the potential future configuration is given.

1 Introduction

In the design of stages that must move in a horizontal plane with relatively large XY-movement disturbing forces from traditional bearings will limit the final accuracy. The use of Active Magnetic Bearings (AMBs) enables to virtually eliminate these disturbances. The generation of driving forces generally introduces heat dissipation, which gives a potential loss of accuracy.

[1] L.Jabben@wbmt.tudelft.nl

The creation of combined electro-magnetic suspension and propulsion systems has been a focus in our research at the Delft University of Technology. F. Auer designed a modular 6DoF table, consisting of 3 contactless Suspension and Propulsion Units (SPU) [1]. Leveraging of Auers work A. Molenaar designed a Planar Active Magnetic Bearing (PAMB) [3], which integrates a reluctance type suspension and a Lorentz-type propulsion with moving coils (moving armature). Permanent Magnets (PMs) are used to generate the bias flux.

Disturbing forces introduced by the feeding wires of the propulsion coils and heat generation by the coils on the rotor form a potential limitation for the performance of the PAMB. This article presents a novel electro-magnetic propulsion principle which deals with these limitations, while keeping the advantages of Lorentz-type actuators.

2 Macroscopic Force Equation

This section will introduce the underlying theory to explain the forces that act in a system consisting of a coil, a PM, and a yoke. By applying the virtual work method the total summed magnetic force F_m on a yoke part movable in the x direction can be derived (see [4, p.190] and [2, p.55]):

$$F_m = I\frac{d\Phi_{cm}}{dx}\bigg|_{(I=0)} + \frac{1}{2}I^2\frac{dL_c}{dx} - \frac{dW_m(x)}{dx}\bigg|_{(I=0)}, \quad (1)$$

with I the current through the coil, Φ_{cm} the flux enclosed by the coil and originating from the PM, x the position of the yoke, W_m the magnetic field energy for $I = 0$ (i.e. from the PMs), and L_c the self-inductance of the coil. The first term is the force due to mutual flux linking, which varies with the flux from the PMs enclosed by the coil and is called *mutual force.* In most applications the magnetic induction (B-field) generated by the coil can be neglected, and the mutual force can be calculated $F = BIl$, the well-known *Bil-law* for Lorentz forces ([2]).

The second term is a function of I^2 and therefore independent of the direction of the current flow. This term always acts to increase the inductance ($\frac{dL_c}{dx} > 0$) or to decrease the magnetic reluctance and is therefore called *reluctance force.*

The third term represents the force due to a change in energy from the permanent magnet W_m, which is also a *reluctance force.*

3 Wireless Propulsion: Moving Iron

A Lorentz force originates from the moving charges in a wire 'I'. Thus, a Newtonian reaction force must act on the source of the magnetic flux density (B). A novel drive concept[2], referred to as *moving iron*, makes use of this reaction force. A rotor bar is driven by Lorentz forces without coils or magnets on it.

3.1 Working Principle

To understand the working principle of moving iron, consider a simple case as depicted in Figure 1. The I-shaped rotor is assumed to be supported on bearings that restrict movement to horizontal displacement[3]. Furthermore, the ferromagnetic C-shaped stator yoke is considered an ideal flux guidance ($\mu_r = \infty$). Therefore, the stator part between permanent magnet and air gap can be elongated without effect, which is indicated by the parallel line pair. Because the magnet poles travel through the flux guidances towards the crossing of the bars that define the air gap, the flux lines leave the stator at a position that moves along with the rotor iron. Thus the rotor behaves as a virtual source of B-field(!), while the actual PM can be positioned at a fixed position of the stator circuit. As a result, the reaction force of the Lorentz force act on the rotor.

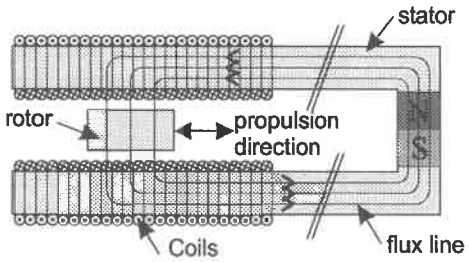

Figure 1: Winding scheme for a moving iron driven rotor, with a spiral wrapped coil option.

Since the guiding flux bars are assumed to be ideal and the air gap height to be constant, the magnetic field energy term resulting from the PMs W_m in (1), does not change with a horizontal change of position. For the same reason the self inductance of the coil will not change. The term $\frac{\Phi_{cm}}{dx}$ is non-zero and does not change with the position x because of the equally devided cupper. Thus a mutual (Lorentz) force is generated with $F \propto I$. A qualitative check is to verify if the enclosed flux of the winding changes while displacing the rotor.

To understand better the difference in a classical approach and the moving iron principle consider Figure 2.

Option A, C and D do not propel the rotor With option A shown in Figure 2, the enclosed flux will increase only with rotation. Hence only a bending moment on the rotor occurs. Option C (fixed to the rotor) will not work either because the enclosed flux is invariant with position change. The same holds for option D (alternatively, the Lorentz forces at both sides of the current loop will counterbalance each other).

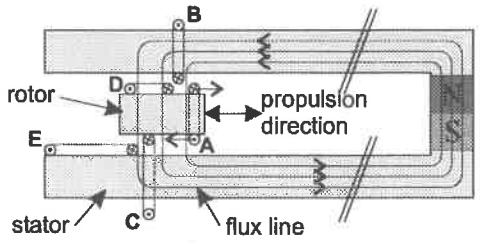

Figure 2: Sketch of a simple linear drive showing five optional drive schemes of which some will lead to a moving iron propulsion.

Option B, and E do propel To get a nett variation of the enclosed flux with a displacement, the return path of the current needs to be positioned outside the air gap region, which is the case with options B and E.

3.2 Moving Iron Winding Schemes

Moving iron requires a yoke configuration where the field moves with the rotor while the field source itself (a permanent magnet or a field coil) is fixed at a remote position of the stator. This is the case in the setup shown in Figure 3, where five more practical moving iron winding schemes are depicted. Options 1 and 2 are flat coils that are wound concentric and with a blending displacement, respectively. These will deliver the same force as the winding option depicted in Figure 1 but with about 50% less power dissipation.

[2]This concept is described in [4], but was not presented before.

[3]The suspension of the rotor is not discussed here, see [3, 4]

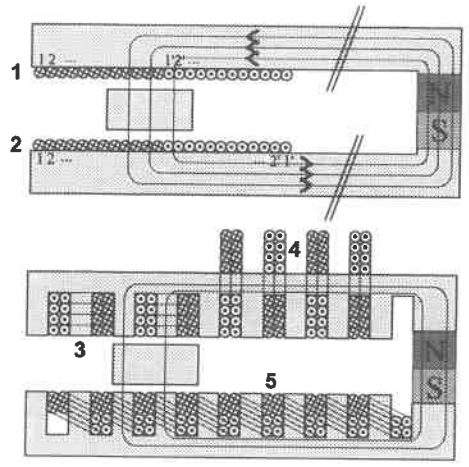

Figure 3: Alternative winding schemes for a moving iron driven rotor. Top: two flat would coil schemes. Bottom: three buried coil options on salient poles.

With options 3, 4 and 5 more ampère-turns can be coupled to the permanent magnet flux for a given motor length. However, parasitic reluctance forces will occur, called cogging. Option 5 has overlapping coils, which is beneficial for smooth and efficient commutation.

3.3 Advantages

Active magnetic bearings utilizing the moving iron principle show three major advantages. First, the positioning accuracy of a moving iron setup is not limited by disturbing forces introduced by the feeding wires of the rotor coils. Secondly, the heat dissipated by the coils can be carried away through the stator material by conduction. Finally, a light weighted and compact linear driven rotor with planar freedom can be created that is not influenced by the size of the coils or the size of the permanent magnets used.

4 Towards a Prototype

4.1 Practical Implementation

The novel moving iron principle can be implemented by modifying the PAMB set-up of Molenaar described in [3, 4]. The less complex moving iron winding scheme of Figure 1, was applied because of practical reasons, although this is not the most power efficient winding scheme. This is shown in Figure 4. Each pair of upper and lower propulsion coils is series connected, thus assuring symmetrical loading.

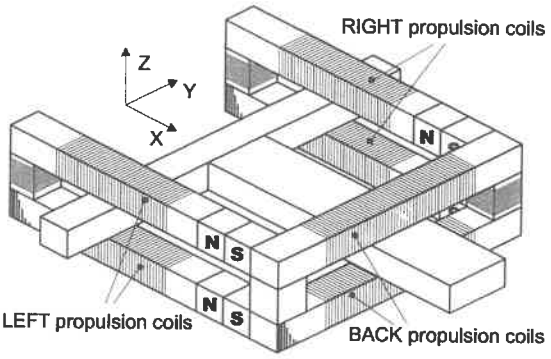

Figure 4: Planar active magnetic bearing with moving iron *propulsion.*

4.2 Dimensioning of the Coils

Next the dimensioning of the coils in Figure 4 is discussed. The size of the flux guiding bars and the rotor (upper part of the T) is 20×20 mm^2. The total air gap between the rotor and stator is 1.1 mm. An aim in the design of the PAMB is to have an accelleration of 1g. With a rotor mass of 3.5 kg, a force of 34.4 N is needed. Forces in the x-direction are generated by the left and right propulsion coils in a total of four air gaps. Assuming a B-field in the air gaps of 1 T, we can calculate with the *Bil-law* that the Ampère turns needed in one airgap is 429. This must be equal to the cross section area of the airgap (1×20 mm^2) times the filling factor times the maximum current density ($\rho_{i,\max}$). Taking $\rho_{i,\max}$ equal to 33 A/mm^2, the gap filling factor that is needed is 65%.

The maximum peak current that amplifier used in the setup can deliver is 4 A, which determines the minimum wire diameter to 0.39 mm. This means that we need two or three layers.

To allow to probe the flux density in the test setup the stator is wound with one layer of a wire with 0.55 mm core and .58 mm outer diameter. This reduces the filling factor to 41% and $\rho_{i,\max}$ to 16.8 A/mm^2. The B-field realized in the test setup is 0.6 T. This results in a propulsion force of $F = 0.6 \cdot 1 \cdot 20 \cdot 0.41 \cdot 16.8 \cdot 20 \cdot 10^{-3} = 1.65$ N per air gap. Thus the total force is $4 \cdot 1.65 = 6.6$ N and the maximum acceleration 1.9 m/s^2.

4.3 Experimental Results

The iron moving principle was applied to the PAMB test set-up as descriped in [3, 4]. The obtained relevant results are given in the table below.

Table 1: *Experimental results of the* PAMB *with the moving iron principle applied.*

characteristic	Aim	Realized
square planar range [mm]	100	130
suspended mass [kg]	3	3.37
position stability $\pm 2\sigma$ [nm]	50	75
air gap height (clearance) [mm]	- (0.1)	1.1 (0.4)
magnetic induction [T]	1	0.6
propulsion force [N]	-	6.5
acceleration [m/s^2]	9.81	1.9

Comparing the propulsion force calculated by the *Bil-law* of 6.6 N, with the realized propulsion force of 6.5 N, confirms that the propulsion force in the moving iron principle may be calculated using the *Bil-law*.

5 Future Research

The *moving iron* principle was successfully applied in the PAMB. However magnetic cross-coupling between the three bearing positions, the asymmetric layout of the PAMB setup and the non-modularity prevents ultimate performance in positioning. Therefore a new design is suggested.

A modular design that utilizes the moving iron principle will allow further improvement of positioning accuracy. Figure 5 shows an example setup of three identical motor-bearing modules. Each module independently suspends and propels one leg of a three legged rotor in 2DoF, thus obtaining a 6DoF PAMB. The propulsion force is exerted at the center of gravity in any planar position, while there is no magnetic coupling between the three bearing positions.

No wires are attached to the rotor. Each motor-bearing module consists of a U shaped stator circuit. The working principle of the this stator circuit is similar to the working principle of the PAMB, taking into account only the left and the bottom part of the stator circuit shown in Figure 4 and "bending" these towards each other. As Figure 5 shows a concept rather that a fixed setup, its layout can easily be adapted to fulfill the needs of future applications.

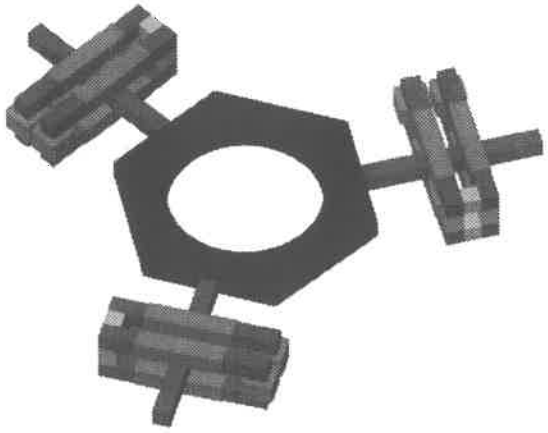

Figure 5: *An example setup for a 6*DoF PAMB *with moving iron propulsion.*

6 Conclusions

A novel electro-magnetic motor principle has been designed an incorporated into a planar magnetic bearing system. The principle has all the properties of Lorentz-type actuators, while having stationary coils and magnets. The motor principle has been tested and fulfills our expectations. Finally, a sketch of a novel motor-bearing design has been presented, utilizing the motor principle described. This modular and symmetrical setup seems very promising for applications where ultra precise positioning and thermal management is of concern.

References

[1] Auer F. et al., "A Magnetically Levitated, Six Degrees of Freedom High Accuracy Positioning System", *Proc. of MAG'95, Magnetic Bearings, Magnetic Drives and Dry Gas Seals*, pp.176-185, 1995.

[2] Hanselman, D.C., *Brushless Permanent-Magnet Motor Design*,McGraw-Hill, 1994.

[3] Molenaar, A., E.H. Zaaijer and H.F. van Beek, "A Novel Low Dissipation Long Stroke Planar Magnetic Suspension and Propulsion Stage", *Proc. 6th Int. Symp. on Magnetic Bearings*, MIT, Cambridge, MA, USA, pp. 650-659, 1998.

[4] Molenaar, A., *A Novel Planar Magnetic Bearing and Motor Configuration applied in a Positioning Stage*, PhD thesis, Delft University of Technology, The Netherlands, Delft, ISBN 90-6464-7372, 2000.

Quiet Hydraulic Actuators for the Laser Interferometer Gravitational Wave Observatory (LIGO)

Corwin T. Hardham, Graham S. Allen, Dan B. DeBra, Wensheng Hua, Brian T. Lantz, Jamie G. Nichol
Stanford University, Stanford CA

Introduction

LIGO is, effectively, the world's most sensitive optical displacement sensor. However, in order for this to be true, the reference mirrors between which the interferometer operates must remain steady with respect to inertial space and to one another. Hence, the suspension systems for the reference mirrors must provide isolation and alignment in all six degrees of freedom (DOF) against a variety of mechanical disturbances. While this problem is broadband, this paper focuses on the design of a unique actuator for a system which specifically addresses the low-frequency isolation and alignment requirements.

Based on predictions for low-frequency disturbances and other specifications of the total suspension, the requirements for the low-frequency system actuator are challenging. Four specifications define this challenge and drive the design of the actuator. They are: max force greater than 2000 N; throw of 1mm; bandwidth of at least 10 Hz; and noise not to exceed 10^{-9} meters rms from 10 mHz to 10 Hz.

Four categories of actuators were considered to meet these specifications: mechanical, electromagnetic, piezoelectric, and hydraulic. While mechanical systems (levers, ball lead screws, worm gears) can meet the force, throw and bandwidth requirements, the static friction and noise inherent in these devices make them poor candidates. Electromagnetic actuators are unsuitable due to the high current (heat dissipation) associated with holding large static offsets. Piezoelectric actuators are excluded by virtue of the hysteresis and limited throw found in these devices. Hydraulic actuators can easily meet the force, throw and bandwidth requirements, but conventional hydraulic actuators are excessively noisy. However, a little known subset of the study of hydraulics known as '*Quiet Hydraulics*' presents a solution which, as the name implies, has the potential to meet the low noise requirements for this application.

Quiet Hydraulics

Quiet Hydraulics differs principally from conventional hydraulics in that the flow in the system is not permitted to become turbulent. By maintaining laminar flow throughout the system, a quiet hydraulic actuator can reach very low noise levels. The quiet hydraulic piston actuator also differs from conventional hydraulic actuators in that there are no friction contact parts, and consequently, no seals. This absence of friction is obtained by using a pair of flexible bellows to constitute the two sides of the piston. A schematic layout of this concept is shown in Figure 1.

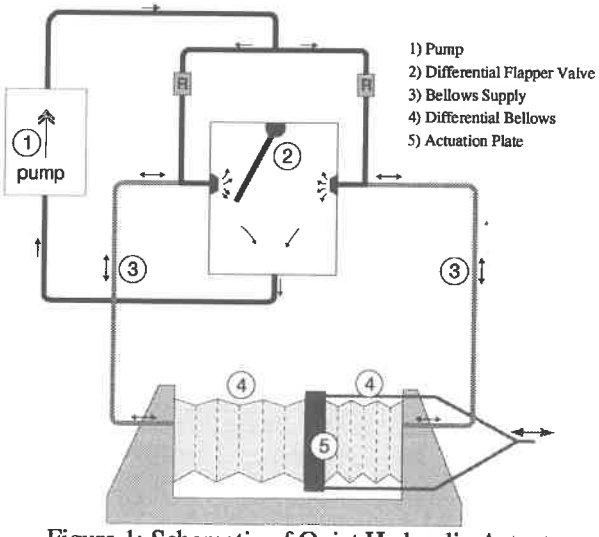

Figure 1: Schematic of Quiet Hydraulic Actuator

As shown in figure 1, the actuator is comprised of five principle parts. The pump (1) provides constant volumetric flow. The flow is then sent through a hydraulic equivalent of a Wheatstone bridge where a servo valve represents the lower two resistances in the bridge. By controlling the position of the flapper in the servo valve (2), the pressure at the intermediate nodes of the bridge are changed thereby modifying the flow to the bellows (3). The differential pressure created at the intermediate nodes of the bridge is applied to the actuation plate (5) by the area enclosed by the bellows (4) thus creating force.

Equations of Motion

In order to design a quiet hydraulic actuator that meets specification, we derive the equations of motion for the actuator. The equations of motion for a state-space representation of the actuator:

$$\begin{bmatrix} z \\ z\cdot s \\ \Delta p \end{bmatrix} \cdot s = \begin{bmatrix} 0 & 1 & 0 \\ \frac{-k}{m} & 0 & \frac{A}{m} \\ 0 & \frac{-A\cdot 2\cdot\beta}{V} & \frac{-2\cdot\beta}{V\cdot R} \end{bmatrix} \cdot \begin{bmatrix} z \\ z\cdot s \\ \Delta p \end{bmatrix} + \begin{bmatrix} 0 & 0 & 0 & 0 \\ \frac{k}{m} & 0 & \frac{1}{m} & 0 \\ 0 & \frac{2\cdot\beta\cdot A}{V} & 0 & \frac{-\beta\cdot P_s\cdot C_v}{V\cdot R} \end{bmatrix} \cdot \begin{bmatrix} z_g \\ z_g\cdot s \\ D \\ i \end{bmatrix}$$

Design Trades

There are many relationships between the design parameters for the actuator that can be derived from the equations above. The scope of these relationships is constrained by external factors such as material limitations in the bellows and other mechanical structures. Nonetheless, from the equations above, we developed a set of parameters that anticipate sufficient force and bandwidth at relatively low flow rates with mineral oil as a working fluid.

Mechanical Design of the Actuator

The dimensions arrived at from the equations of motion dictate the sizes for most of the components in the actuator. However, the mechanical design must also include compliant connections such that when multiple actuators are arranged to operate in concert (in an effort to control multiple DOF), the actuator is relatively uncoupled in all DOF except for the forcing direction of the individual actuator. In addition, for the purposes of feedback control, we have found that it is particularly convenient to incorporate sensors in the mechanical design such that they are colocated (aligned with the actuation axis and stiffly connected) with the actuator.

The first prototype design is shown in Figure 2. The tetrahedral arrangement of bars acts as a ball and socket joint which is stiff in the direction of actuation, but relatively soft in all other DOF. Parallel motion flexures are included at the sides of the actuation plate to constrain motion to one axis. The displacement sensor is well colocated directly between the actuator connection bolt and the top bellows.

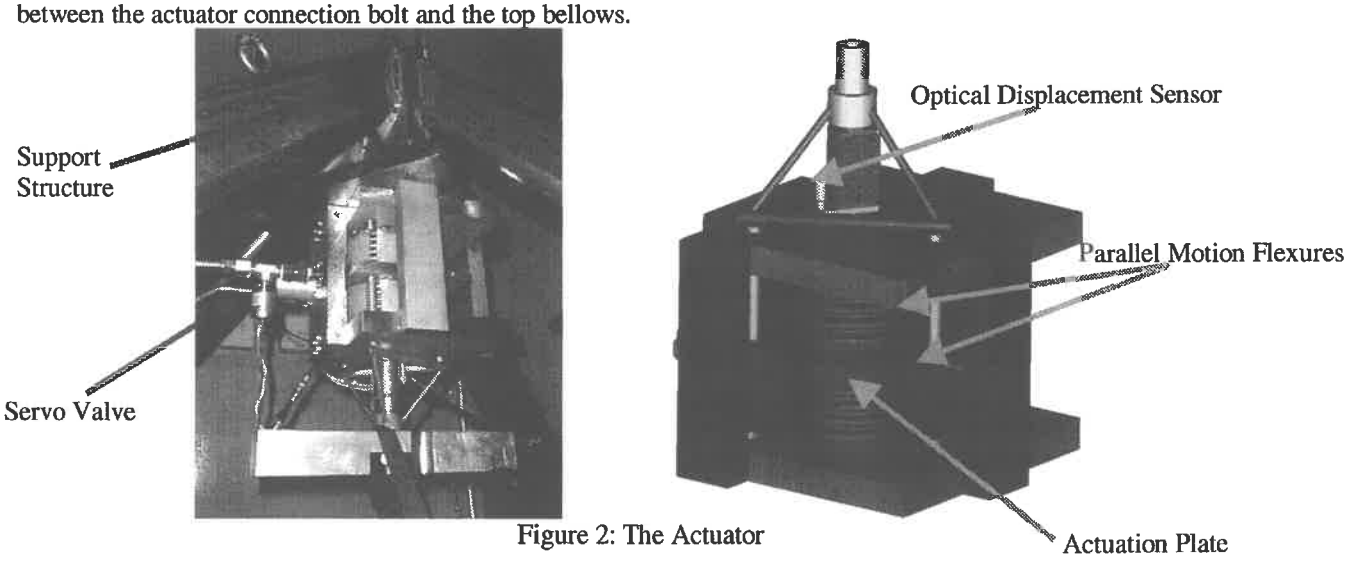

Figure 2: The Actuator

Filtering of a Pressure Source

Since the pressure differential across the two bellows yields the force created, the actuator noise is sensitive to pressure fluctuations from the pumping source. Pressure fluctuations can be removed both by passive and active means, but in order to remove both high and low frequency fluctuations, both are necessary. Passive reduction is done using accumulators. However, in order to reduce pressure fluctuations at low frequencies, a servo valve was added to the pump manifold. The servo valve operates in a feedback loop with a pressure sensor located at the pump. With the application of both filtering techniques the pressure fluctuations were reduced by two orders of magnitude at most frequencies.

Test Platform

With a well conditioned pressure source, we began to make measurements in preparation for control of the actuator. In order to conduct these tests, we constructed the test platform shown in Figure 3. The test platform situates two actuators around a test mass in such a way as to provide an exact replication of one corner of the final system in LIGO. In this configuration, each actuator is paired with a displacement sensor (as shown before) and a low frequency seismometer.

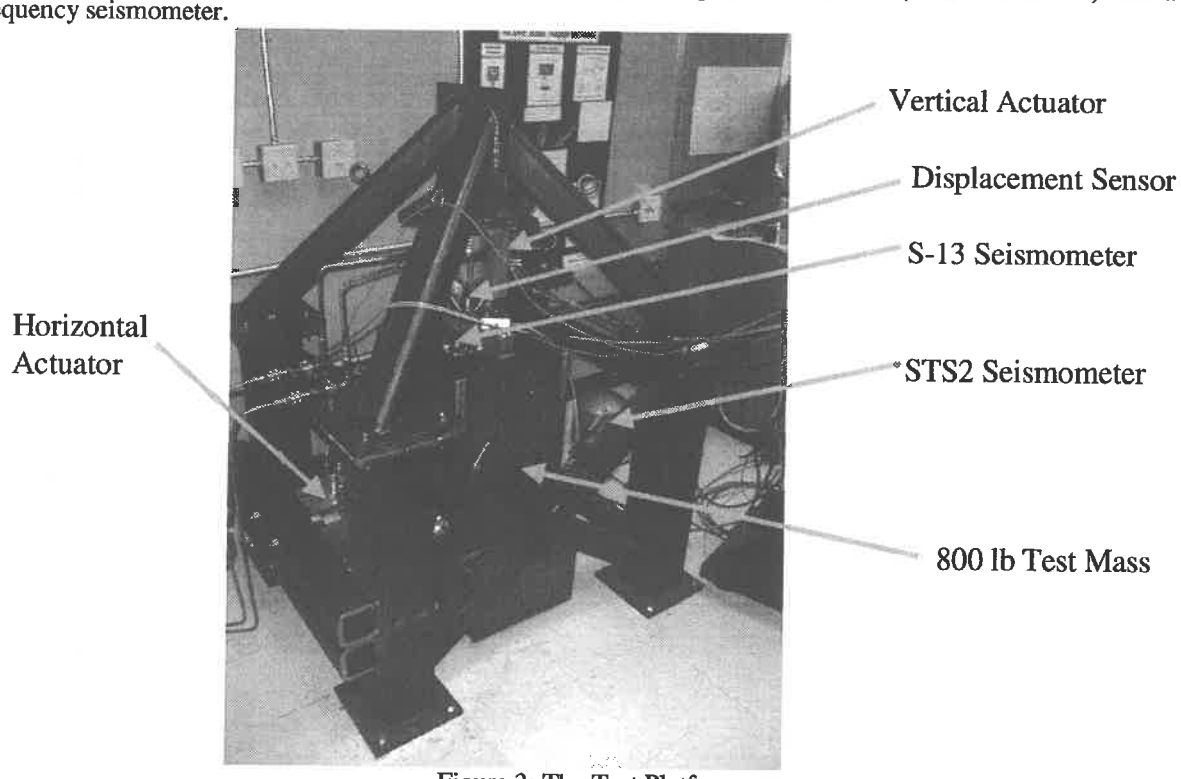

Figure 3: The Test Platform

Noise Measurements

The differential nature of the servo valve makes the actuator motion less sensitive to pump pressure fluctuations when the valve is centered. Therefore, it is necessary to extend the actuator to its maximum throw (and thereby, maximum force) in order to conduct worst case noise measurements. In this worst case scenario, the motion of the test mass as observed by the displacement sensor was measured, and both the horizontal and vertical actuators meet specification.

Control Schemes

The test platform incorporates several sensors that could be used to close both feedback and feedforward loops in either a single-input / single output (SISO) or multi-input / multi-output (MIMO) fashion. However, in

consideration of the alignment requirements for the final application we chose to apply a SISO control scheme known as sensor correction.

In this scheme, a feedback loop is designed to operate between the displacement sensor output and the servo valve on the actuator. The displacement sensor loop is designed to have large low-frequency gain for alignment authority, and in order to not introduce high frequency noise, the controller bandwidth is limited to 15 Hz. The output of the displacement sensor is:

Displacement Sensor Out = Position of Suspended Mass – Position of Ground

We recognize that by closing a feedback loop with the displacement sensor the test mass is controlled to follow the position of the ground. This is in direct conflict with the goals of seismic isolation. In order to remedy this, we correct the output of the displacement sensor by measuring the position of the ground (with a large inertial sensor on the ground) and add it to the displacement sensor output. Figure 4 is a plot of the relative transmission of seismic motion from the ground to the test mass both with the control on and off. This is a measure of the isolation performance of the actuator.

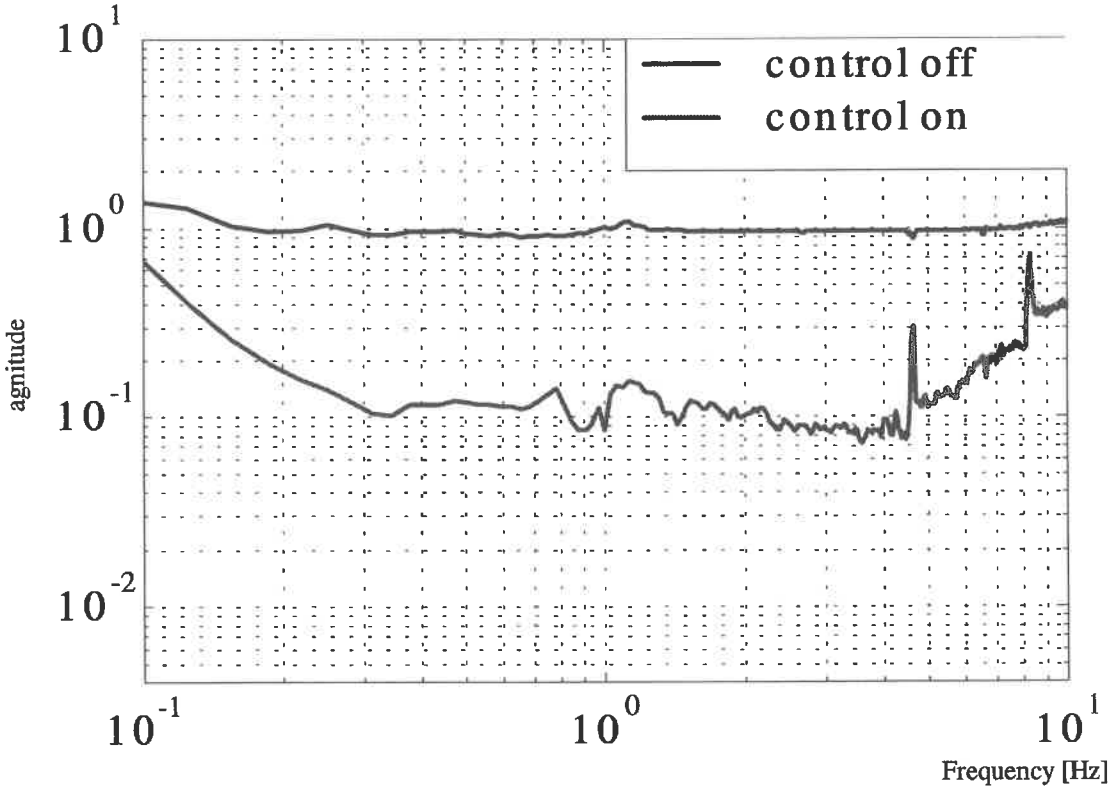

Figure 4: Isolation Performance

Conclusions

We have designed and constructed a quiet hydraulic actuator that meets specification for application in LIGO. We have demonstrated that two of these actuators can be operated in concert to meet seismic isolation and alignment specifications in each axis.

AC Motor Control in Precision Machines

Michael K. Liebman and David L. Trumper

Massachusetts Institute of Technology
Cambridge, MA 02139

Abstract

The field orientation principle allows us to control AC motors as if they were DC motors. AC motors, such as synchronous and induction motors, have multiple phases and complex transient behavior, which make them difficult to control. DC motors are simple to control: the armature current is directly proportional to the electric torque. The field orientation principle transforms stator currents for an AC motor into field currents, which are analogous to the currents in a DC motor. In this abstract we review the derivation of the field orientation transformations and show how they can be used to control AC motors.

Introduction

The ease with which DC motors can be controlled is due to the fixed arrangement of the main flux and armature flux. The main flux is directed between the two field windings of the DC motor and is also called the direct axis flux. The armature flux is oriented 90 electrical degrees from the main flux and is also therefore called the quadrature-axis flux. The fixed 90° angle between the direct-axis flux and the quadrature-axis flux produces maximum torque. In DC motors the mechanical commutator does the hard work of maintaining these two axes perpendicular to each other as the rotor rotates. The result is an easily controllable motor. In AC motors, we perform the commutation electrically, without the aid of a mechanical commutator. If we can achieve the same effect in AC motors, with the direct and quadrature axes always perpendicular, they will also be easily controllable.

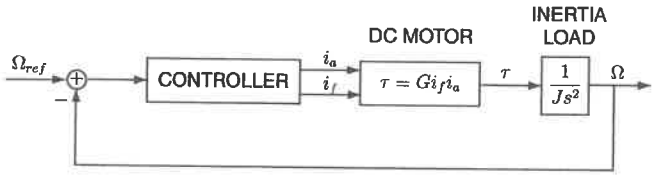

Figure 1: Standard control block diagram showing a DC motor driving a load.

Figure 1 shows a standard control block diagram for controlling the angular position Ω of a load attached to a separately excited DC motor. We assume that high bandwidth current controllers directly set the motor currents. The torque τ produced is proportional to the field current i_f and armature current i_a, as developed in many controls textbooks, $\tau = Gi_f i_a$. Thus it seems we can control the motor torque by adjusting either the field current i_f, or armature current i_a, or perhaps both. Typically, a DC motor is operated at maximum field current, and the armature current is adjusted to control torque. A DC motor using permanent magnets instead of field windings to create the main flux can be thought of as a separately excited DC motor with constant field current i_f. Thus, a permanent magnet DC motor is operated only by changing the armature current.

Field Orientation Transformations

In this section we derive the field orientation transformations which are used to simplify AC motor control. The derivation presented here draws upon Leonhard's excellent book, *Control of Electical Drives* [2], and uses similar notation. Another good reference is *Electric Machinery* [1].

We consider a rotary AC motor with a cylindrical cross-section. We will examine the case of a two-pole motor with symmetrical three-phase windings. The three stator currents, $i_{Sa}(t), i_{Sb}(t), i_{Sc}(t)$, may vary in any way provided that they are balanced,

$$i_{Sa}(t) + i_{Sb}(t) + i_{Sc}(t) = 0. \tag{1}$$

Thus, only two of the three currents can be set independently.

We now define $\mathcal{F}(\alpha, t)$ as the number of ampere-turns enclosed by a closed loop magnetic flux path which crosses the air gap radially at an angle α from the a-axis at time t. We will also define an angle γ that represents the offset angle for the other motor phases: for a three-phase motor $\gamma = 120°$. We will model the spatial ampere-turns distribution of each phase as sinusoidal and centered on the phase's magnetic axis. This yields an expression for the ampere-turns of a closed loop flux path crossing the air gap at an angle α,

$$\mathcal{F}(\alpha, t) = N\left[i_{Sa}(t)\cos\alpha + i_{Sb}(t)\cos(\alpha - \gamma) + i_{Sc}(t)\cos(\alpha - 2\gamma)\right]. \tag{2}$$

We can simplify the math by using complex numbers, for example, by substituting

$$\cos\alpha = \frac{1}{2}(e^{j\alpha} + e^{-j\alpha}), \tag{3}$$

and by introducing a time-dependent complex current vector,

$$\vec{i_S}(t) = i_{Sa}(t) + i_{Sb}(t)e^{j\gamma} + i_{Sc}(t)e^{j2\gamma} = i_S(t)e^{j\zeta(t)}, \tag{4}$$

where $i_S(t)$ and $\zeta(t)$ are the time-dependent magnitude and phase of the complex current vector $\vec{i_S}(t)$. Using equations (2), (3) and (4) we can write the ampere-turns wave $\mathcal{F}(\alpha, t)$ as

$$\mathcal{F}(\alpha, t) = \frac{1}{2}N\left[\vec{i_S}(t)e^{-j\alpha} + \vec{i_S^*}(t)e^{j\alpha}\right] = Ni_S(t)\cos(\zeta(t) - \alpha). \tag{5}$$

Equation 2 expresses the ampere-turns wave as a superposition of sinusoidal waves centered on the three magnetic axes with magnitudes determined by the three phase currents, i_{Sa}, i_{Sb}, and i_{Sc}. Equation 5 says that the same ampere-turns wave can also be thought of as a single sinusoidal wave with instantaneous magnitude $i_S(t)$ whose peak is instantaneously located at an angle $\zeta(t)$ from the a-axis.

At this point, it should be stressed, that the phase currents can vary in any arbitrary manner provided they are balanced. Although we are using a complex vector $\vec{i_S}(t)$, we have not specialized to steady state operation, and our complex quantities should not be mistaken for complex phasors used to describe steady state oscillation.

As an example of the formalism we have developed, let's consider the special case of steady-state rotation of the stator magnetomotive force at speed ω. If we feed the stator with balanced, three phase currents,

$$i_{Sa}(t) = I\cos(\omega t), \tag{6}$$

$$i_{Sb}(t) = I\cos(\omega t - \gamma), \tag{7}$$

$$i_{Sc}(t) = I\cos(\omega t - 2\gamma), \tag{8}$$

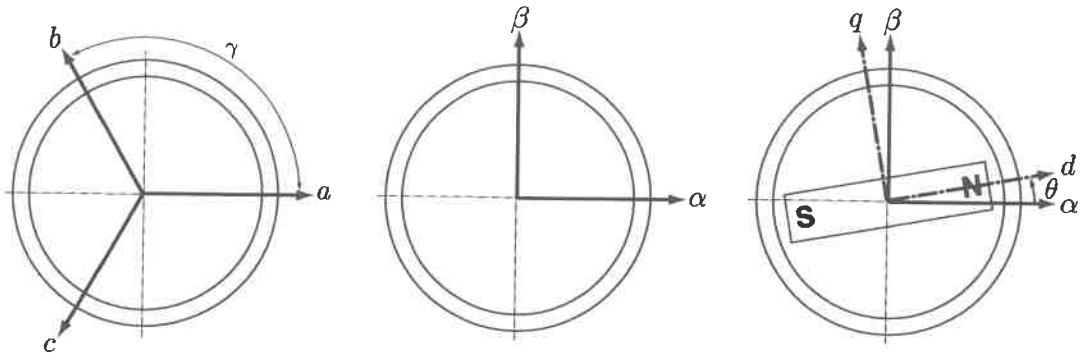

Figure 2: The *abc* axes form a three-phase AC system fixed in the stator frame. The $\alpha\beta$ axes represent an equivalent two-phase AC system fixed in the stator frame. The *dq* axes represent an equivaelnt two-phase DC system that rotates with the rotor flux.

equation (4) tells us that $i_S(t) = \frac{3}{2}I$ and $\zeta(t) = \omega t$. Thus the magnetomotive force wave $\mathcal{F}(\alpha, t)$ has a fixed magnitude, $\frac{3}{2}NI$, and rotates at constant angular velocity ω.

We are now ready to develop the field orientation transformations. The transformations will allow us to express the magnetomotive force and magnetic fields in the motor as two orthogonal components that rotate with the axis of the rotor's flux. We define the direct axis or d-axis to be aligned with the rotor's flux and the quadrature axis or q-axis to lead the direct axis by 90°. The d- and q-axes are shown on the right in Figure 2. For a motor with a permanent magnet rotor, the d-axis is aligned with the permanent magnet and rotates with the rotor.

Figure 2 shows three equivalent frames for describing the stator currents. The field orientation transformations allow us to switch between frames. The $abc \leftrightarrow \alpha\beta$ transformation converts between a three-phase AC system with fixed axes *abc* and a two-phase AC system with fixed axes $\alpha\beta$. It can be derived by equating the complex current vector $\vec{i_S}(t)$ in the *abc* frame to the complex current vector in the $\alpha\beta$ frame,

$$i_{Sa} + i_{Sb}e^{j\frac{2\pi}{3}} + i_{Sc}e^{j\frac{4\pi}{3}} = i_{S\alpha} + ji_{S\beta}. \tag{9}$$

Equation (9) together with the condition for balanced currents, equation (1), yields the $\alpha\beta \rightarrow abc$ transformation,

$$i_{Sa} = (2/3)i_{S\alpha} \tag{10}$$

$$i_{Sb} = -(1/3)i_{S\alpha} + (1/\sqrt{3})i_{S\beta} \tag{11}$$

$$i_{Sc} = -(1/3)i_{S\alpha} - (1/\sqrt{3})i_{S\beta}. \tag{12}$$

The $\alpha\beta \leftrightarrow dq$ transformation converts between a two-phase AC system with fixed axes $\alpha\beta$ and a two-phase DC system with rotating axes *dq*. The *dq* system corresponds to a DC motor, and in steady state its quantities are constant. We define θ as the angle of rotation of the *dq* frame from the $\alpha\beta$ frame as shown in Figure 2. The $\alpha\beta \leftrightarrow dq$ transformation can be derived by equating $\vec{i_S}(t)$ in the fixed $\alpha\beta$ frame and in the rotating *dq* frame,

$$i_{S\alpha} + ji_{S\beta} = (i_{Sd} + ji_{Sq})\, e^{j\theta}. \tag{13}$$

The $dq \rightarrow \alpha\beta$ transformation is

$$i_{S\alpha} = i_{Sd}\cos\theta - i_{Sq}\sin\theta \quad (14)$$

$$i_{S\beta} = i_{Sd}\sin\theta + i_{Sq}\cos\theta. \quad (15)$$

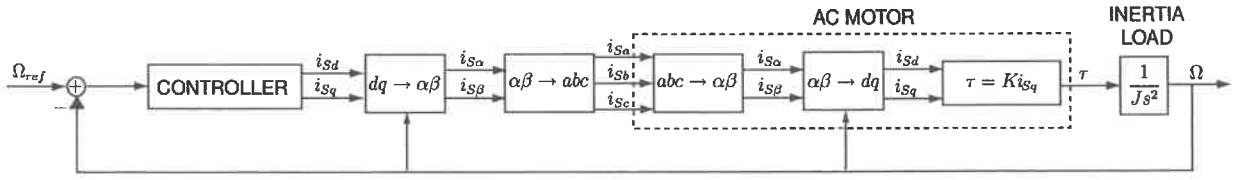

Figure 3: Block diagram of AC motor control in field coordinates. The transformations inside the AC Motor block are part of the motor model.

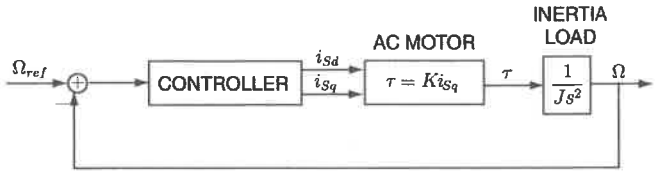

Figure 4: Controller design in field coordinates is analogous to DC motor controller design.

The field orientation transformations reduce the controller design procedure for AC motors to the familiar procedure for DC motors as shown in Figures 3 & 4. Since d-axis flux and q-axis current in an AC motor correspond to the main flux and armature current in a DC motor, the AC motor torque is proportional to i_{Sq}, $\tau = Ki_{Sq}$. For an AC motor with a permanent magnet rotor, the rotor flux is fixed and there is no point trying to change it with stator currents, so we set $i_{Sd} = 0$. The controller outputs desired torque which is proportional to q-axis current, i_{Sq}. Then, the $dq \rightarrow \alpha\beta$ and $\alpha\beta \rightarrow abc$ transformations convert i_{Sq} and $i_{Sd} = 0$ into 3-phase currents. The motor model, however, inherently contains the inverse field orientation transformations which turns 3-phase currents into mechanical torque. Thus, for the purposes of controller design, the forward and reverse transformations cancel each other and may be omitted as in Figure 4. The controller for the AC motor can now be designed as if it were controlling a DC motor.

References

[1] A. E. Fitzgerald, Jr. Charles Kingsley, and Stephen D. Umans. *Electric Machinery.* McGraw-Hill, Inc., New York, 1990.

[2] Werner Leonhard. *Control of Electrical Drives.* Springer, New York, 1997.

Precision Motor Control Development Using Rapid Control Prototyping Tools

E. Hill, R. Venugopal and V. G. Moudgal
dSPACE, Inc
22260 Haggerty Road, Suite 120
Northville, MI 48167
{ehill, rvenugopal, vmoudgal}@dspaceinc.com

Servo control of motor driven systems is one of the basic applications of control theory, and is a topic that has been extensively studied in the literature. However, several recent applications ranging from optical switching systems in communication networks to space-based precision pointing systems demand very high levels of performance and robustness. These requirements necessitate the design and implementation of high performance controllers within short development cycles. The use of Rapid Control Prototyping (RCP) tools significantly reduces the design, development and testing phases of new controllers, and thus enables a designer to meet tight time-to-market schedules. The ability to rapidly modify the structure and parameters of a controller is a key benefit of these tools. In this paper we describe the design and implementation of three control strategies on an optical sensing test-bed using RCP tools.

The test-bed consists of a DC brushless motor with a mirror mounted on it, a pulsed semiconductor laser and eight optical sensors. The objective is to slew the mirror in minimum time with a pointing accuracy sufficient to reflect the laser beam on to any specified optical sensor. The optical sensors are spaced 20 degrees apart at a radius of 15cm from the mirror. The mirror is directly mounted to the motor shaft via a specialized mounting fixture. The motor rotates the mirror so that the laser beam can illuminate each of the sensors. At each sensor, the laser is modulated to provide an eight-bit data stream. The sensors, and supporting circuitry, convert the light pulses into a TTL level electrical signal that can be monitored using digital inputs or an oscilloscope. After transmission of the data stream, the mirror rotates to the next detector and sends a new eight-bit data stream. Each sensor receives eight-bits of data at a minimum refresh rate of 100ms. The overall dimensions of the unit will be approximately 40cm wide by 20cm deep by 6cm tall. The unit will house the power supply, servo amplifier, and supporting electronic circuitry.

The paper describes the modeling, design, simulation and real-time implementation procedures used in the development of the control laws. PID and H_2 –optimal (LQG) controllers are tested and trade-offs between performance and design and implementation complexity are studied. A brief discussion on transitioning the concepts validated in the RCP environment to production is also included.

The tasks involved in the control system design process are
1 System Identification
2 Controller Design
3 Offline Simulation
4 Real-Time Implementation and Testing

System Identification: The electromechanical hardware in the system consists of a Computer Optical Products CM355 three-phase DC brushless motor with a 2048 line optical encoder attached to the shaft. The motor is driven by an Advanced Motion Controls current amplifier, which also handles the commutation of the three-phase signals. The controller is implemented on a dSPACE DS1103 controller board that feeds a reference voltage to the current amplifier.

The first task in designing the controller is to obtain a mathematical model of the system dynamics from amplifier voltage input to encoder position measurements. This task is accomplished by using system identification. The N4SID subspace algorithm is used for this purpose and is implemented using the MATLAB System Identification Toolbox. The input-output data used for system identification is obtained by driving the system with a random signal between +/-1V from the DS1103 and reading the encoder output. An unstable second-order state space model of the system dynamics is obtained using N4SID with an effort of 4 man-hours.

PID Controller Design: The control objective is to design a controller that achieves a 5% settling time of less than 50milliseconds with a steady-state error of less than 0.4 degrees. Using the identified state-space model of the motor dynamics, a PID controller is tuned by running several simulations of the closed-loop in Simulink. Then, this controller is implemented on the DS1103 using the dSPACE Real-Time Interface to Simulink at a sampling rate of 10KHz. The figures below show the experimental closed-loop system response to a square wave input at 1 Hz. The effort required for this phase of the design was 4 man-hours.

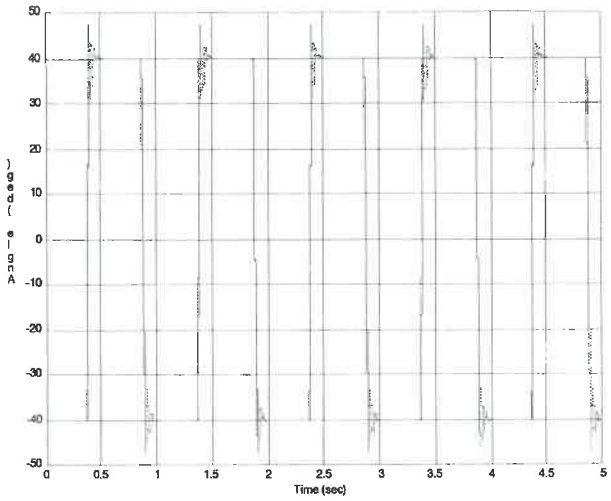

Figure 1: Closed-Loop Response of Motor with PID Controller. Solid Line: Shaft Position, Dashed Line: Reference Command

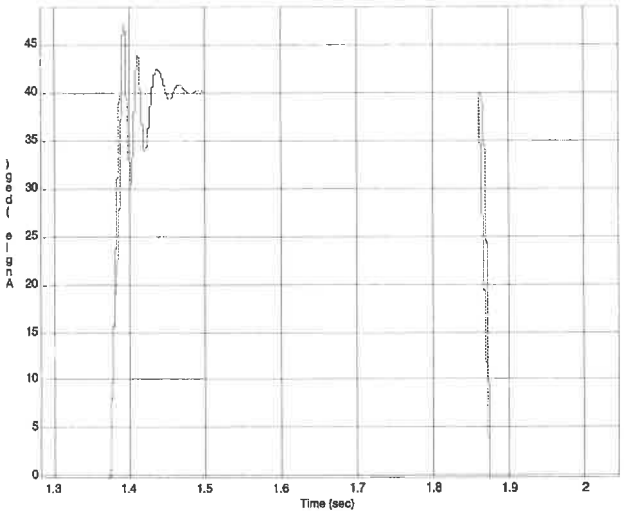

Figure 2: Transient Response of Motor with PID Controller. Solid Line: Shaft Position, Dashed Line: Reference Command

From the plots, we can see that achieve the control objective with a 5% settling time of about 45 milliseconds and with a steady-state error of 0.2 deg. However, the system has an undershoot of about 12%.

LQG Controller Design: An H_2 –optimal (LQG) controller is designed using the MATLAB Control System Toolbox by calculating the optimal regulator gain matrix and the Kalman filter (observer) gain. The system matrices obtained from system identification are used to calculate these gains by solving the associated Riccati equations. Several simulations are performed in Simulink using the identified model and different choices of control and output weights. The controller that performs the best in terms of settling time and steady-state error is then implemented on the DS1103 controller board running at a sampling rate of 10 KHz. The experimental closed-loop performance is shown in Figures 3 and 4. The effort required for this phase of the design was 4 man-hours.

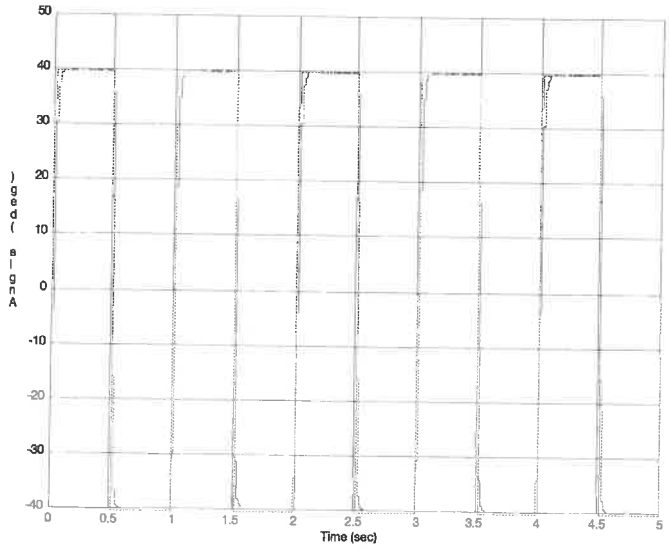

Figure 3: Closed-Loop Response of Motor with LQG Controller. Solid Line: Shaft Position, Dashed Line: Reference Command

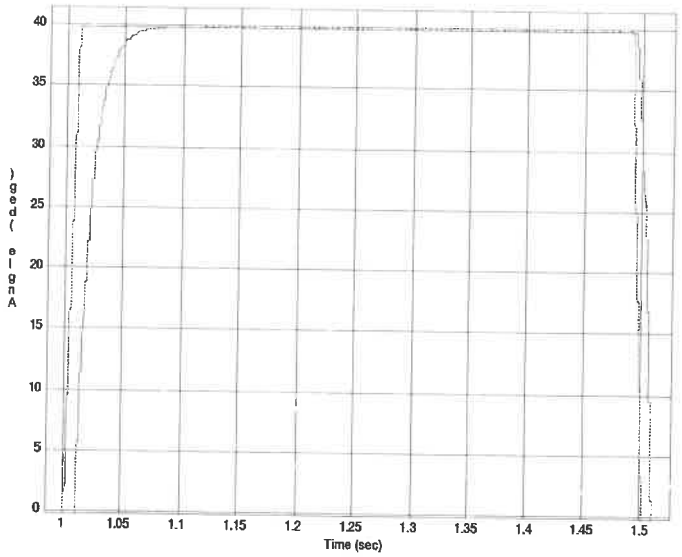

Figure 4: Transient Response of Motor with LQG Controller. Solid Line: Shaft Position, Dashed Line: Reference Command

The LQG controller achieves the control objective with a 5% settling time of 35 milliseconds and a steady-state error of 0.2 deg. It also shows a significant improvement in transient response characteristics compared to the PID controller with the output showing no overshoot.

Summary: This paper describes the use of Rapid Control Prototyping (RCP) tools for precision motion controller design. A test-bed for validating precision motion control concepts is described. We present results that use a combination of design and RCP tools to develop a state-space model of a DC brushless motor, and to design two controllers that meet steady-state response specifications using position feedback from an encoder. System identification, controller design and real-time experimental implementation for both controllers were achieved with an effort of 12 man-hours.

Adapting Feedforward for Active Vibration Isolation Systems

Dr. Peter G. Nelson
Dr. Emil Kraner
Technical Manufacturing Corporation (TMC)
15 Centennial Drive, Peabody, MA 01960

Vibration isolation systems have been crucial to semiconductor manufacturing equipment for many years. As geometries become smaller, and the need for higher machine throughputs increases, the demands on the isolation systems have become severe. This has been frustrated by the advent of 300mm wafers, which require heavier moving stages with longer travels. These factors have caused force impulses on payloads to become enormous, while the need to settle payloads to quieter levels, in less time, has become critical.

Active vibration isolation systems have the ability to address many of the issues generated by these changes. Both feedforward and feedback techniques can be employed to reduce payload settling times and noise levels. In pneumatic-based active vibration isolation systems, feedback can be strongly limited by structural resonances which limit servo bandwidth. Even if high bandwidths could be achieved, they may not be desirable: Though high bandwidths can give a system exceptionally good settling time for accelerations, the settling time for position in such servos is long. This makes any process which requires precise alignment with off-payload machinery very difficult (such as wafer loading/unloading and optics alignment).

Although some feedback should be used to *damp* the isolators' passive resonance to a suitable level, it should not be used to achieve active *isolation* or improve settling time. Instead, feedforward should be used to improve settling time. This is motivated by the fact that most machines do not require better isolation – they function perfectly well after the payload settles after a stage motion.

Feedforward can improve settling time be reducing the net force a payload sees from a stage motion. If the amplitude of force can be suppressed by a factor of 10, so is the required settling time. More than a factor of 10 is not considered realistic considering the non-ideal aspects of such systems. To obtain this level of suppression, the system must use an adaptive algorithm for finding the feedforward parameters.

Such systems have two feedforward inputs: the X and Y stage position. In addition, sensors mounted to the payload can determine the payload's motion in all six DOFs. Feedforward is accomplished by using servo valves for controlling isolator pressure, and electromagnetic actuators for applying short force pulses to the payload. There are a minimum of 12 parameters required to implement such a feedforward scheme, with several of the terms being nonlinear. One problem is to adapt these 12 parameters with only 8 inputs in a stable way. Pneumatic-only feedforward can avoid much cost and complexity, while maintaining significant benefit.

Pneumatic only feedforward still requires a minimum of 4 parameters to be adaptively set. This algorithm is complicated by the relatively slow response time of the isolators to valving compared with the time scales for typical stage motions. The talk will focus on the type of algorithms being developed at TMC for this problem, and types of issues that come up.

Enhancing Positioning Performance of Lithography Stages Using Smart Structures Technology

Baruch Pletner, Huck Dorn
Active Control eXperts, Inc., Cambridge, Massachusetts
Moti Karpel
Technion — Israel Institute of Technology

I. Introduction

As chip-making throughput requirements have increased, the positioning bandwidth of lithography stages has increased dramatically, bringing flexible deformation modes into the control band of the structures. This, coupled with the stages' low level of structural damping (arising from the requirement that the stages be both light and stiff) creates situations where active vibration control is attractive.

This study models the effect of applying induced strain actuators to the elastic portions of a lithography stage in order to reduce broadband vibration disturbances. Vertical servo-positioning of the stage is accomplished using a PID controller, while the elastic vibration damping is implemented using a Linear Quadratic Gaussian (LQG) controller.

A secondary objective of the study was to develop a numerically manageable state-space model, starting from a Finite Element (FE) model of over 60,000 elements. To achieve this, several model reduction techniques were employed, including the use of fictitious masses to simulate local actuator effects.

An illustration of the type of stage discussed in this paper is shown in Fig. 1. Note the presence of the three servo actuators used to actuate the stage in the vertical (Z) direction. The location of the elastic strain actuators is shown in Fig. 2, and is discussed in greater detail in a later section.

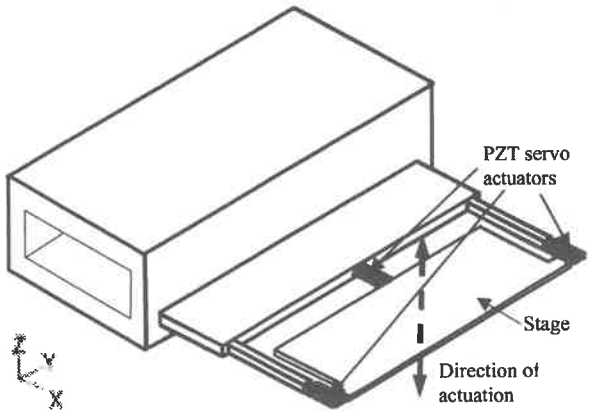

Fig. 1: Lithography stage

II. Model Reduction

This section describes modeling reduction techniques used for the dynamic analysis of a simulated lithography stage, resulting in state-space models for efficient simulation and augmentation of control systems.

Many FE codes solve for the structural response to a prescribed time-domain excitation by either the direct transient-response analysis or by the modal transient analysis. The direct procedure solves the equation

$$[M]\{\ddot{u}\}+[B_d]\{\dot{u}\}+[K]\{u\}=\{F(t)\} \qquad (1)$$

by numerical integration. It is very inefficient with a large number of degrees of freedom. Instead, a modal procedure can be used to solve

$$[M_s]\{\ddot{\xi}\}+[B_s]\{\dot{\xi}\}+[K_s]\{\xi\}=\{F_s(t)\} \qquad (2)$$

with a number of user-selected low-frequency vibration modes taken into account. The number and type of modes to be included in the modal analysis depends on the nature of the problem, with a trade off between accuracy and computational efficiency. For large structural models, the number of modes adequately taken into account is several orders of magnitudes smaller than the order of the full-size model. Hence, most structural dynamics analyses are based on the modal approach. One has to be careful, however, with the number and type of modes taken into account. When the excitation forces are prescribed (rather than functions of the structural response), there are usually negligible differences between the direct frequency response and the modal one, provided that the later includes all the natural vibration modes within the excitation frequency range. Hence, there is no advantage in using the direct approach in frequency-response analysis. However, when the forces are affected by the response, such as in control-augmented structures, one has to be careful in selecting the modes for modal analysis as in transient analysis.

Advanced modal methods that use fictitious masses and complementary static loads can be used to improve the model's accuracy and/or efficiency. As discussed later, the fictitious-mass (FM) approach is both suitable for dealing with PZT actuators, and can be applied conveniently with standard FE codes.

Derivation of State-Space Equations of Motion

To facilitate the integration of control systems and response simulations using modern synthesis tools, the modal equation of motion (2) is converted to the first-order state-space standard form

$$\{\dot{x}\} = [A]\{x\} + [B]\{u_i\} \tag{3}$$

where

$$\{x\} = \begin{Bmatrix} \xi \\ \dot{\xi} \end{Bmatrix}, \qquad \{u_i\} = \{F_e\},$$
$$[A] = \begin{bmatrix} 0 & I \\ -M_s^{-1}K_s & -M_s^{-1}B_s \end{bmatrix}, \quad [B] = \begin{bmatrix} 0 \\ M_s^{-1}\phi_e^T \end{bmatrix} \tag{4}$$

where $\{F_e\}$ is a vector of non-zero force components and $[\phi_e]$ contains the associated rows in $[\phi]$.

The outputs of the dynamic system can be expressed in the form

$$\{y\} = [C]\{x\} + [D]\{u_i\} \tag{5}$$

where discrete displacement, velocity and acceleration outputs are cast in this form with

$$\begin{aligned} [C_d] &= [\phi_d \;\; 0], \quad [D_d] = 0 \\ [C_v] &= [0 \;\; \phi_v], \quad [D_v] = 0 \\ [C_a] &= -[\phi_d][M]^{-1}[K_s \;\; B_s], \\ [D_a] &= -[\phi_d][M]^{-1}[\phi_f] \end{aligned} \tag{6}$$

where $[\phi_d]$, $[\phi_v]$ and $[\phi_a]$ are matrices of modal displacements at the associated outputs.

The standard set of state-space equations expressed by equations (3) and (5) can be used by utility codes such as Matlab for time-domain and frequency-domain analyses and for analysis and synthesis of augmenting control systems.

The Use of Fictitious Masses

A disadvantage of the modal approach is that important structural information near points of external excitation might not be contained in the low-frequency modal information. This problem might be magnified when PZT actuators are used. Adequate dynamics and control analyses with such actuators require high-accuracy representation of the surrounding structure. Static modes of structural deformations due to unit forces at the actuation points are sometimes added to the modal basis to overcome this problem. But, when the actuators are in a statically determined connection path, such as the Z-stage PZT stack-actuators in this study, this solution might not be adequate.

The fictitious-mass (FM) modal-coupling method [1] opened the way for the inclusion of local deformations around selected grid points. The method uses sets of low-frequency modes generated by standard normal-modes analysis procedures. Relatively large fictitious masses are added at selected points when the modes are calculated. The mass effects of theses masses are "cleaned" when the subsequent models are constructed, but the essential local deformations are retained in the modal information.

With a fictitious mass matrix $[M_F]$ added to the finite-element model, the resulting eigenvalues in the diagonal matrix $[\Omega_F] = [\omega_F^2]$ and the associated eigenvectors $[\phi_F]$ satisfy

$$[K][\phi_F] = [M + M_F][\phi_F][\Omega_F] \tag{7}$$

We now return to the original equation of motion (1) and assume that the displacement vector is a linear combination of a set of normal modes calculated with the fictitious masses, namely

$$\{u\} = [\phi_F]\{\xi_F\} \tag{8}$$

The substitution of equation (8) in (1), the pre-multiplication by $[\phi_F]^T$ and the removal of the damping and the external force terms yield the free undamped modal equation of motion

$$[M_f - \phi^T M_F \phi]\{\ddot{\xi}_F\} + [K_f]\{\xi_F\} = \{0\} \tag{9}$$

where $[M_f]$ and $[K_f]$ are the generalized mass and stiffness matrices associated with equation (7):

$$\begin{aligned} [M_f] &= [\phi_F]^T[M + M_F][\phi_F] \\ [K_f] &= [\phi_F]^T[K][\phi_F] \end{aligned} \tag{10}$$

Equation (9) forms an eigenvalue problem whose eigenvalues and eigenvectors satisfy

$$[K_f][\psi] = [M_f - \phi_F^T M_F \phi_F][\psi][\bar{\Omega}] \tag{11}$$

The diagonal terms of $[\bar{\Omega}]$ are the "cleaned" eigenvalues, namely those obtained from the FM modes by removing the effects of the fictitious masses. In typical applications, most eigenvalues (except the largest ones) are practically identical to those calculated directly for the original system ($[\Omega]$). The remaining eigenvalues are not natural ones, but they should be included in the model when the local response near the fictitious-mass points is of interest. The cleaned modes associate with $[\bar{\Omega}]$ can be calculated by

$$[\bar{\phi}] = [\phi_F][\psi] \tag{12}$$

With $[\psi]$ normalized such that

$$[\psi]^T[M_f - \phi_F^T M_F \phi_F][\psi] = [I] \tag{13}$$

A state-space model of the form of equations (3)-(6) can then be constructed with $[M_s] = [I]$, $[K_s] = [\bar{\Omega}]$ and $[\phi] = [\bar{\phi}]$.

Elastic Strain Actuators

In order to provide vibration damping, elastic strain actuators were modeled on the two support arms of the lithography stage. The location of these actuators is shown in Fig. 2 below. Depending on the state of actuation of the two strain actuators, the support arm can be controlled in extension (X-direction) or in bending (around the Y-axis).

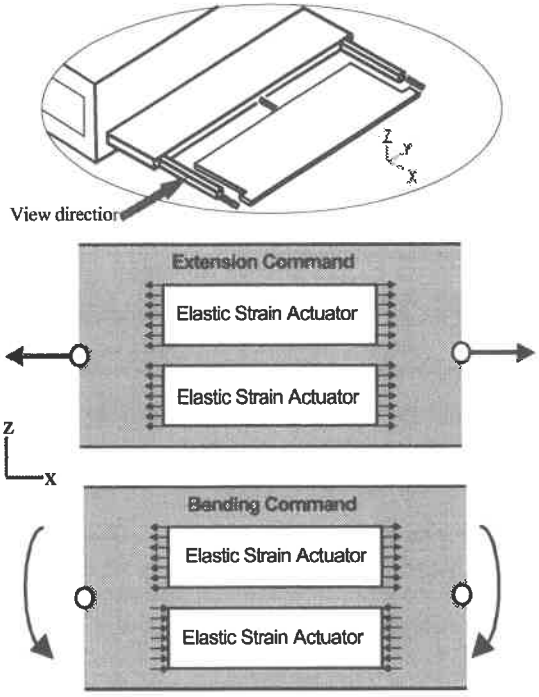

Fig. 2: Location and orientation of elastic strain actuators

In this model, it was assumed that the elastic actuator stiffness values are small compared to those of the ceramic arms to which they are attached. The addition of fictitious masses to the end points of these actuators in the normal-modes analysis facilitates the accurate inclusion of actuator forces and deformations in the input and output parameters of the resulting state-space model. It also allows the addition of strain actuator stiffness effects without returning to the FE analysis. Two state-space models were generated, one based on FE normal-modes analysis without fictitious masses and one based on FE analysis with 14 fictitious masses. Six fictitious masses, 30Kg each, were added in the Z direction at the servo actuator points. Four fictitious masses, 100Kg each, were added in the X direction of the strain actuator end points. Four fictitious moments of inertia, 30Kg·m^2 each, were added in the θ_y direction at the strain actuator end points. As demonstrated below, the fictitious masses are essential for an accurate account of the strain actuator deformations.

Step Response to Servo Actuator Commands

The step responses shown in this section are due to a deformation command of -4μm in the Z direction at one of the servo actuators in Fig. 1. To demonstrate the main purpose of the fictitious masses, the response of the right actuator to the -4μm command at this actuator is shown in Fig. 3 and Fig. 4 (without and with fictitious masses, respectively). While the step response without fictitious masses converges to –3.74μm, the response with fictitious masses converges to -4μm, exactly as it should.

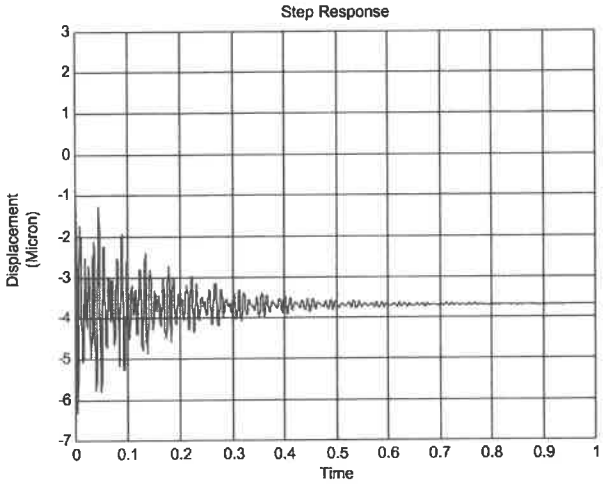

Fig. 3: Step response of the right servo actuator to a -4μm command at that actuator, without fictitious masses.

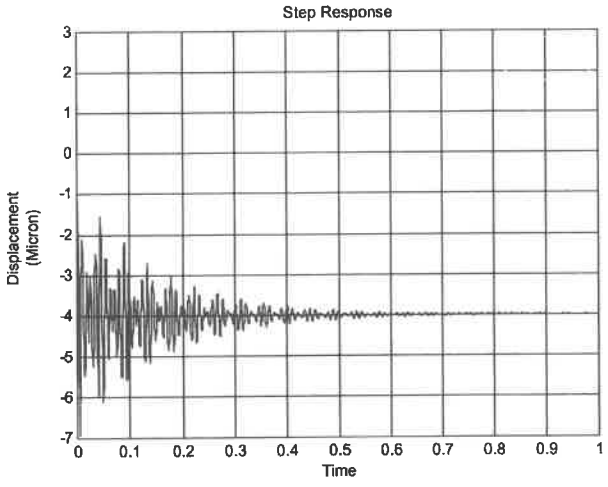

Fig. 4: Step response of the right servo actuator to a -4μm command at that actuator, with fictitious masses.

Frequency Response

Also of interest is the frequency response of the stage. Fig. 5 below shows the transfer function from an input disturbance on the body of the lithography structure to an output on the stage. The direction and location of the input and output are shown in Fig. 6. The structure has natural frequencies at 90Hz, 112Hz,

and 158Hz, which correspond to mode shapes of vertical deflection, torsional bending, and in-plane deflection of the stage, respectively. These modes offer potential for significant vibration reduction, and are thus target modes for the elastic actuators mentioned described earlier.

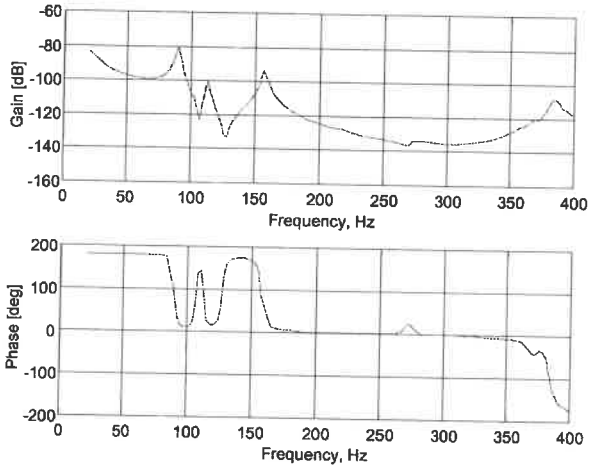

Fig. 5: Frequency response of lithography stage

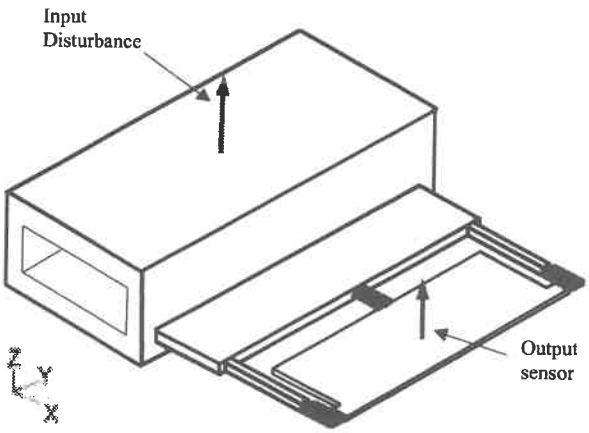

Fig. 6: Input/Output locations of frequency response

III. Control Architecture

This section describes how the control problem was set up and how techniques were used to design controllers and simulate closed loop performance.

The performance requirements for the lithography tool require the pitch and roll components of the stage to be fixed while tracking a vertical (Z-motion) trajectory. For our analysis, we choose to command the three servo actuators in unison as a one degree of freedom actuator for Z-direction positioning. Since doing so reduces the ability of the actuators to attenuate the elastic vibrations of the Z-table structure, the elastic actuators located on the Z-table support arms were used to suppress the vibrations.

Clearly, this is not the only possible architecture. For example, the three servo actuators could be used independently to control Z, pitch and roll motions simultaneously to a given command. However, as a first solution, the decoupled tracking and vibration damping architecture was adhered to. This architecture is attractive since the servo actuators have no control authority over the horizontal vibrations of the Z-table (Y and yaw) that are excited by Y acceleration of the reticle stage and Y-direction noise coming in through the guide. The control problem was therefore set up to allow optimal observability and controllability for the Z-direction positioning, and six degree of freedom elastic control.

There are two control loops in the design: the Z servo-positioning loop, and the vibration control loop. Both can be seen in Fig. 7 below. A PID controller is used for the servo positioning control. A single input single output (SISO) loop is closed around an output that gives the vertical position of the stage. The input command is deducted from this output resulting in a position error signal. This signal is then fed back into a PID controller, the output of which is fed into all three positioning actuators simultaneously.

The control design technique used for vibration control is multiple input multiple output (MIMO), output-weighted linear quadratic Gaussian (LQG). This technique was chosen because it is particularly effective for attenuating the response of dynamic systems in the presence of broadband stochastic disturbances such as air bearing noise. In order to simulate real-world operation, a command (either 10-micron step or 30-micron shaped input) is introduced into the servo loop, and band-limited white noise is introduced into the guide acceleration inputs. In addition, a finite-time pulse is introduced into the Y-direction guide acceleration in order to simulate stage acceleration to exposure.

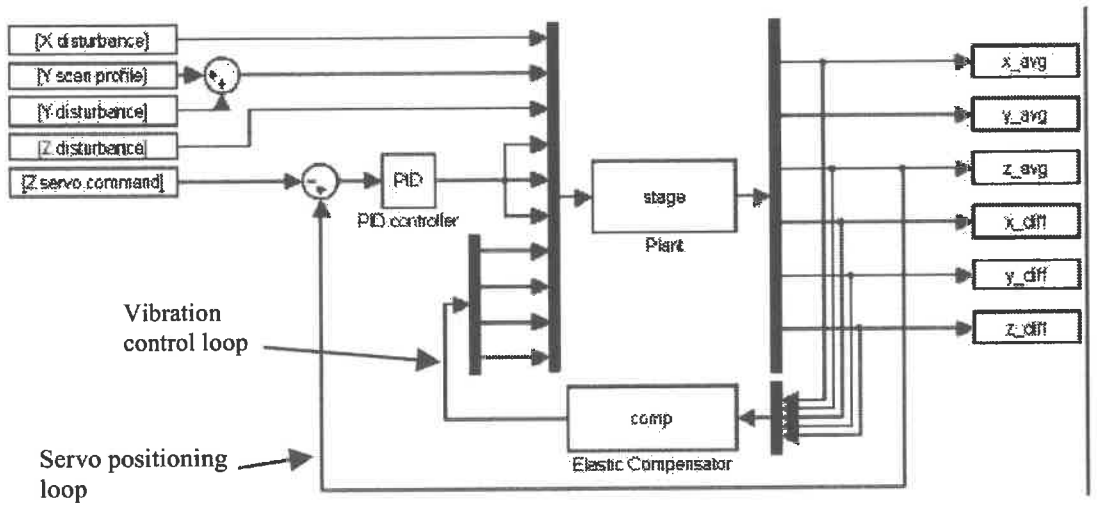

Fig. 7: Control Architecture

IV. Results

Fig. 8 shows two responses to a step input, one response with only servo control active, the other with both servo and elastic control active. The elastically controlled response has a faster rise time and greatly reduced vibrations.

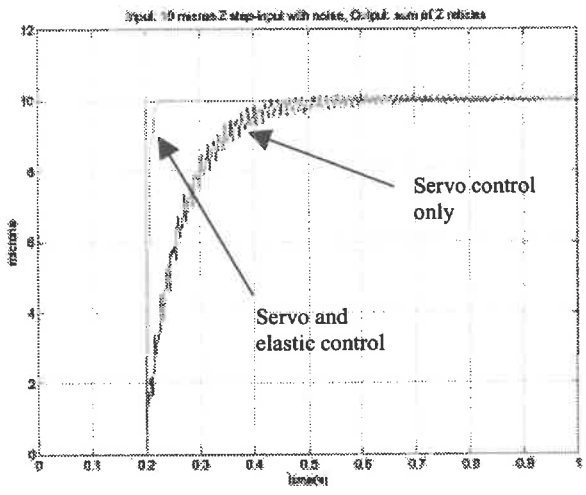

Fig. 8: Response to step input

Fig. 9 shows the response to a shaped input with only servo control active, while Fig. 10 shows the response to the shaped input with both servo and elastic control active. The two figures also display the tracking error (difference of command and response.) The decrease in tracking error from Fig. 9 to Fig. 10 illustrates the effect of the elastic damping.

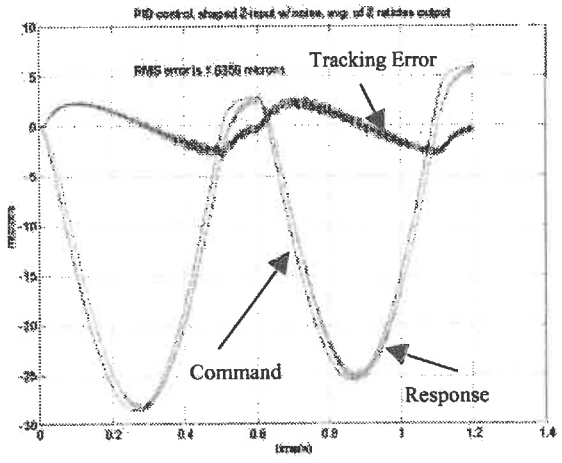

Fig. 9: Response to shaped input, PID control only

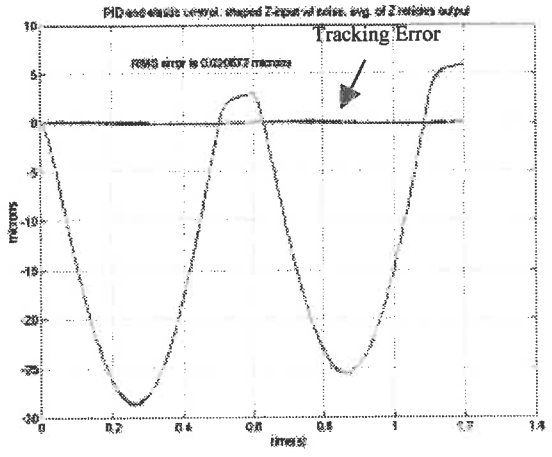

Fig. 10: Response to shaped input, PID and elastic control

V. Conclusions

The use of order reduction techniques to derive a low-order, state-space representation of critical system dynamics from a large FE model has been successfully applied to a simulated lithography stage. A FE model of over 60,000 elements was reduced to a 36-state state-space model. The dynamic response of both models was compared, and the validity of the reduced-order state-space model demonstrated.

A straightforward PID design of the vertical positioning servo was demonstrated to be difficult due to the lightly damped modes in the servo control band. Furthermore, the stage shows considerable flexibility in the Y direction, potentially requiring unacceptably long settling times. A set of elastic actuators was designed to attenuate both vertical (bending, twisting), and horizontal (Y-axis) vibrations. These actuators were simulated in the FE model, and formed a subset of the inputs into the state-space model.

A set of characteristic disturbance inputs was generated, and a simple Z servo-positioning control loop designed and implemented. A fully coupled MIMO linear quadratic Gaussian compensator was designed for the vibration control loop. This compensator was shown to be very effective in reducing both vertical and horizontal plane vibrations in the stage structure. The resulting actively damped stage structure was shown by simulation to meet the servo positioning requirements even with non-optimal servo control architecture.

References

1. Karpel, M. and Newman, M., "Accelerated Convergence for Vibration Modes Using the Substructure Coupling Method and Fictitious Coupling Masses", Israel Journal of Technology, Vol.13, 1975, pp. 55-62.
2. Karpel, M. and Raveh, D., "Fictitious Mass Element in Structural Dynamics", AIAA Journal, Vol. 34, No. 3, 1996, pp. 607-613.

HIGH GAIN CONTROL FOR HIGH PERFORMANCE – DUSTING OFF THE CLASSICS

Dale E. Schinstock and Zhouhong Wei
Mechanical Engineering Dept, University of Tulsa, Tulsa, OK

INTRODUCTION

In most modern machine tools excellent tracking control can be achieved through the proper application of classical loop shaping design methods. Although these methods are not new, modern interpretations and applications of these techniques are often the best solution to control problems for machines required to move with high speeds and high accelerations. However, if we are not careful classical loop shaping design techniques may soon become a lost art. It is difficult to find anything but a cursory treatment of the subject in the modern texts used to educate our young engineers. Despite the fact that these methods have been widely employed in the past with good success, they are not well understood by many modern controls experts. Therefore, when they are used, they are often not used optimally.

Tracking control for linear motors is used in this paper as a context for a modern interpretation of classical loop shaping control design methods. The techniques presented are directly applicable to the common PID controller structure employed in the majority of machine motion controllers. The methods are also pertinent to many servo actuators other than linear motors. The techniques and results should be important to the controls practitioner in optimizing PID controller designs for tracking and in comparing results from classical designs to modern techniques. The methods stress high-gain controller design and interpret what this means for PID control.

The theoretical basis for the methods presented here is drawn from classical SISO frequency response techniques, which have received little attention in the past four decades. It is also drawn from a few modern extensions of the classical work. To mention a couple of influential examples the reader is referred to [1], [2], and [3]. While the theory behind these methods is not new, their application to modern systems is starkly lacking in the research literature, despite the fact they are still the preferred methods of most practitioners.

HIGH GAIN DESIGN

In the context of this discussion high gain refers to a large open-loop transfer function (TF) gain (magnitude) at low frequencies. For a unity feedback system, like that shown in the upper right corner of Fig. 1, the low-frequency gain of the open-loop TF, G, can be directly related to the error response. Therefore, when applied correctly, loop shaping design techniques are very effective in obtaining a classical feedback controller that gives good tracking and disturbance rejection. They are directly applicable to the common PID controller. In loop shaping design the magnitude of the open-loop TF is manipulated by changing the controller to obtain a desirable "shape" for the overall open-loop magnitude.

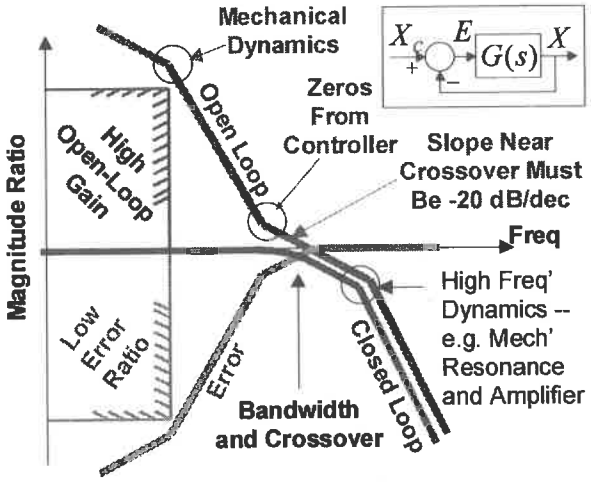

Fig. 1 – Desirable shapes for TF magnitudes

In servo applications the open-loop TF is the ratio of the output to the error signal.

$$G(s) = \frac{X(s)}{E(s)} \tag{1}$$

The block diagram in Fig. 1 can be manipulated to show that the TF relating the error response to the command input is

$$S(s) \equiv \frac{E(s)}{X_c(s)} = \frac{1}{1+G(s)} \tag{2}$$

S is sometimes referred to as the "sensitivity" function. In (2) it can be seen that where G is large the error ratio is small. In fact the error magnitude is approximately the inverse of the open-loop gain.

$$|S(s)| \cong \frac{1}{|G(s)|} \quad \text{for} \quad |G(s)| >> 1 \tag{3}$$

A similar result can be demonstrated using the closed-loop TF,

$$T(s) \equiv \frac{X(s)}{X_c(s)} = \frac{G(s)}{1+G(s)} \tag{4}$$

Where the magnitude of G is large, the magnitude of T should be approximately one (0 dB). Ideally T would have a magnitude of one for all frequencies.

Figure 1 shows the desirable shape of the open-loop magnitude. Since high-speed, high-acceleration moves have a high "frequency content," it is important to keep the open-loop gain as large as possible over a wide range of frequencies. Increased low frequency gain is achieved by pushing the crossover frequency (and bandwidth) out, and by increasing the rate of decent of G before the crossover. However, for stability reasons, the slope of the asymptotic open-loop magnitude must be –20 dB/dec in the region near the crossover. This is necessary for a satisfactory phase margin. Therefore, in all practical systems, the bandwidth is limited by higher frequency dynamics such as amplifier dynamics and mechanical modes other than the nominal dynamics. These higher frequency dynamics increase the decent of the magnitude, coinciding with a larger phase lag. While it is theoretically possible to compensate for these higher frequency dynamics with additional controller dynamics, in practice this is difficult without additional sensors that can be used to directly sense their affects. Maximizing the open-loop gain becomes a balancing act between performance and stability.

The following properties are desirable for the shape of the open-loop magnitude:

- high-gain over a broad range of low frequencies
- a –20 dB/dec slope in region around the zero dB crossover frequency, and
- a zero dB crossover frequency equal to the desired closed-loop bandwidth.

Linear Motor Test System

A linear motor (LM) motion stage is used as an example to demonstrate the concepts discussed in the previous section. This system is shown in Fig. 2. The picture shows two linear motors coupled with a flexible beam to model a gantry style machine axis. However, in this work only one of the motors is used, decoupled from the other. The LM has a 3-phase coil assembly surrounding a permanent magnet (PM) rod assembly. It is analogous to a rotary PM brushless motor with a sinusoidal back emf. The stage has a linear optical encoder with a resolution of $1\,\mu m\,(3.94\times10^{-5}$ in) for position feedback and motor commutation. The servo drive (motor amplifier) is operated in a closed-loop current/force mode with an analog voltage input from a motion-control digital-signal-processor (DSP) card. The position controller is implemented on the floating-point DSP card with a servo update rate of 5 KHz.

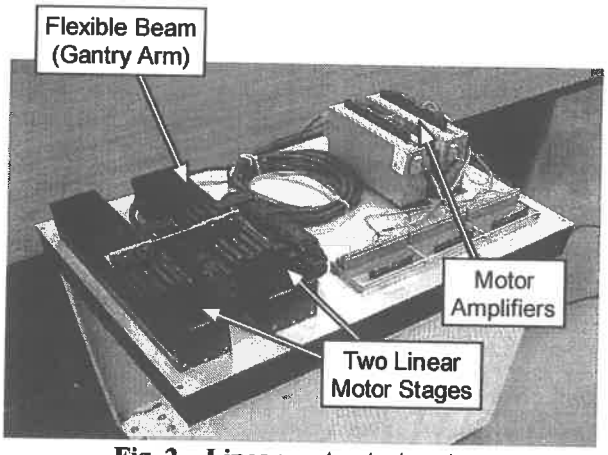

Fig. 2 – Linear motor test system

The system is controlled with a traditional PID feedback controller, depicted by G_c in Fig. 3. The PID TF is given in (4). The product of the other three TFs in Fig. 3 is considered the plant for detailed analysis. The nominal plant G_p accounts for typical second order mechanical dynamics.

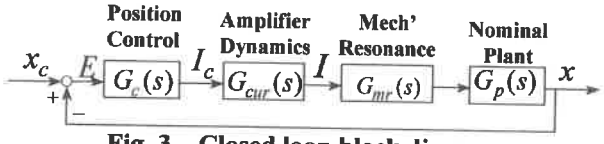

Fig. 3 – Closed loop block diagram

$$G_c(s) = \frac{k_d s^2 + k_p s + k_i}{s} = \frac{k_d (s+z_1)(s+z_2)}{s} \tag{4}$$

The nominal plant, given in (5), includes the mass, m, and a viscous approximation of the friction, b, for the LM stage. It also includes the motor force constant, k_f, and a constant of proportionality, k_a, relating the output voltage from the DSP to the steady-state current in the motor.

$$G_p(s) = \frac{k_a k_f}{ms^2 + bs} \tag{5}$$

This nominal plant is a second order, type 1, system structure common in many electromechanical servo applications.

A good controller can be designed using only estimates of the nominal plant's parameters. The occurrence of higher frequency dynamics can be found through experimentation or rough estimation. However, for the sake of completeness and for research purposes the higher frequency dynamics of the system have been identified.

In testing of the closed-loop current response it was found that a combination of two lightly damped modes with resonant frequencies of 1 kHz and 2.5 kHz was found to be a good model of the closed-loop current dynamics. This model is given in (6).

$$G_{cur}(s) = \frac{\omega_{c1}^2}{s^2 + 2\zeta_{c1}\omega_{c1}s + \omega_{c1}^2} \cdot \frac{\omega_{c2}^2}{s^2 + 2\zeta_{c2}\omega_{c2}s + \omega_{c2}^2} \quad (6)$$

The open-loop frequency response indicated a mechanical resonance around 800 Hz. This resonant mode contributes an additional 180 deg. phase shift at high frequencies, indicating that the mode is a non-collocated mode as given in (7).

$$G_{mr}(s) = \frac{\omega_m^2}{s^2 + 2\zeta_m\omega_m s + \omega_m^2} \quad (7)$$

Estimates of the values for the parameters of the plant are as follows: $k_a = 1\,Amp/V$, $k_f = 4.2\,lb/Amp$, $m = 0.0128\ lb\cdot s^2/in$, $b = 0.121\,lb\cdot s/in$, $\omega_{c1} = 6283\,rad/s$, $\zeta_{c1} = 0.6$, $\omega_{c2} = 15{,}708\,rad/s$, $\zeta_{c2} = 0.2$, $\omega_m = 5027\,rad/s$, $\zeta_m = 0.15$.

Controller Design

Two different PID controllers are used to demonstrate the affect of open-loop gain. The target bandwidth chosen for both controllers is 200 Hz. This target was chosen using the limitation imposed by the 800 Hz mechanical resonance. The bandwidth is one fourth the frequency of the lightly-damped high-frequency mechanical mode. This is a fairly aggressive design. It results in small stability gain margins. The controller, G_c, is chosen using the "shape" of the following open-loop TF.

$$G(s) = G_c(s)\cdot G_{cur}(s)\cdot G_{mr}(s)\cdot G_p(s) \quad (8)$$

For a PID controller, the open-loop gain is maximized at low frequency by pushing the zeros from the controller to as high a frequency as possible. As shown in (4), G_c can be factored into two zeros, z_1 and z_2, a free integrator in the denominator, and the derivative gain. The zeros are used to compensate the negative slope (and corresponding phase lag) of the plant and the controller integrator. Therfore, they must be placed significantly before the crossover, where the slope should be –20 dB/dec. This is necessary to allow the open-loop phase to come up towards –90 deg. It approaches this value asymptotically in regions where the slope is –20 dB/dec. For the high-gain controller the PID zeros are placed at 40 Hz ($z_1 = z_2 = 40\cdot 2\pi$ rad/s). For the lower gain controller they are placed at 5 Hz ($z_1 = z_2 = 5\cdot 2\pi$ rad/s).

With the zeros of the controller known, the only unknown parameter in G is k_d. This gain is chosen to set the open-loop magnitude to one at the desired crossover frequency (bandwidth).

$$\frac{1}{k_d} = \left|\frac{G(j\omega)}{k_d}\right|_{\omega=200\cdot 2\pi} \quad (9)$$

Figure 4 shows the theoretical open-loop frequency responses resulting from these two controllers.

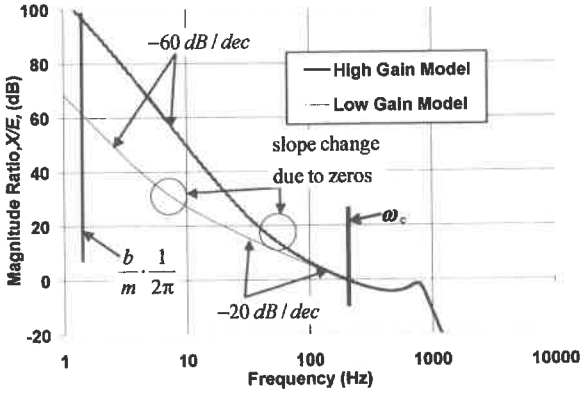

Fig. 4 – Theoretical open-loop frequency response

The higher gain controller has the following gains: $k_p = 1712.6\ V/in$, $k_i = 215208\ V/in\cdot s$, $k_d = 3.4070\ V\cdot s/in$. The lower gain controller has the following gains: $k_p = 222.49\ V/in$, $k_i = 3494.9\ V/in\cdot s$, $k_d = 3.5411\ V\cdot s/in$.

Experimental Results

Figures 5 shows the theoretical closed-loop magnitude resulting from the two controllers along with experimental data for the high-gain controller. Figure 6 shows the magnitude of the theoretical error responses

along with experimental data for the high-gain controller. A large peak in the closed loop response near the open-loop mechanical resonance frequency results in both systems because of the aggressive choice for crossover. Figure 6 demonstrates the effectiveness of using large open-loop gains in reducing the tracking error. While both controllers have good low-frequency gain, the controller that optimizes this gain by pushing the zeros out to higher frequencies gives a much better error response, even though it has the same approximate bandwidth as the lower gain controller.

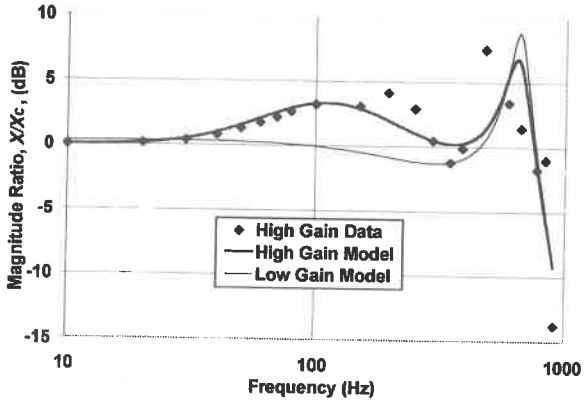

Fig. 5 – Closed-loop magnitude

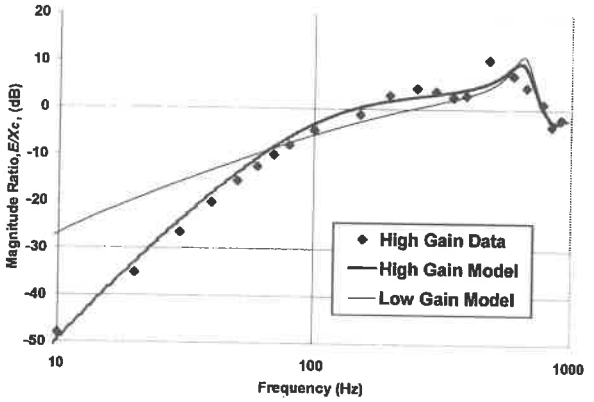

Fig. 6 – Error magnitude

A more meaningful demonstration of tracking control might use a motion other than the sinusoids used in the generation of frequency response. For example, a trapezoidal velocity profile in a point-to-point move might be used. Figure 7 shows one such profile that was run on the LM system. It uses a 3g acceleration limit in a two-inch move. The error during this move is shown for both controllers in Fig. 8.

The error for the high-gain system is significantly reduced and reaches a maximum of about 2 thousandths of an inch. This performance is very good for such high acceleration moves.

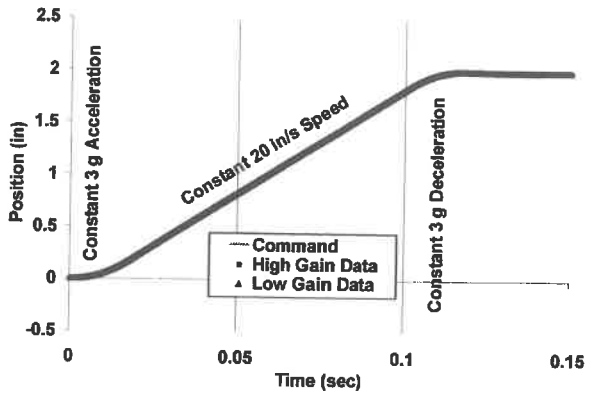

Fig. 7 – Position data for a 3-g-acceleration, point-to-point, move

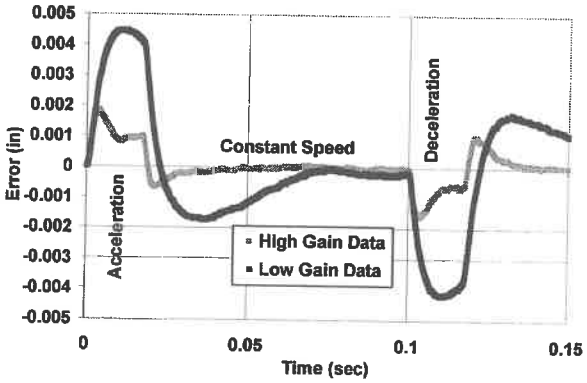

Fig. 8 – Error data for a 3-g-acceleration, point-to-point move

ACKNOWLEDGEMENTS

This work was conducted in the Electromechanical Systems Laboratory (EMSyL) at the University of Tulsa and was supported in part by a grant from the United States' National Science Foundation (NSF Grant No. 9977661) through the EPSCoR program. TU EMSyL is part of a larger EMSyL group involving several universities and industrial, state, and federal partners.

REFERENCES

[1] I. Horowitz, "Optimum Loop Transfer Function in Single-Loop Minimum-Phase Feedback Systems," *International Journal of Control*, pp 97-113, vol 18, no 1, 1973.

[2] G.F. Franklin, J.D. Powell, and A. Emami-Naeini, *Feedback Control of Dynamical Systems*, Addison – Wesley Publishing Co., Reading, MA, 1986, Ch. 5.

[3] S. Skogestad, and I. Postlethwaite, *Multivariable Feedback Control*, John Wiley & Sons, New York, NY, 1996, Ch. 2.

A Six Degree of Freedom, Piezoelectrically Actuated Translation Stage

Richard M. Seugling, Roy H.R. Jacobs[♠], Stuart T. Smith, Lowell P. Howard[♣], Thomas LeBrun[*]

Center for Precision Metrology, UNC Charlotte, NC 28223, [♠]Technical University of Eindhoven, Department of Mechanical Engineering, Precision Engineering Section, Netherlands, [♣]YafoNetworks Inc., MD, [*]Precision Engineering Division, NIST, Gaithersburg, MD 20899.

Summary

This paper discusses the design, manufacture, and testing of a piezo-electrically actuated, six degree of freedom, fine motion translation stage having a translation range of 1.7 μm with 10 pm resolution and a maximum rotation of 30 μrad in all freedoms. To reduce susceptibility to vibrations and to enable dynamic error compensation, the stage system it is desired to have a lowest mode resonant frequency above 500 Hz with a settling time of 10 ms under closed loop control. In particular, the reasons for using a three orthogonal actuator pair design, finite element analysis, individual actuator testing and an initial evaluation of the complete translation stage are outlined.

1.0 Introduction

The initial motivation behind the development of this stage was to increase the range of an x-ray interferometer[1,2] while, in the process, developing an instrument subsystem to position specimens or probes for future pursuits in biological/medical[3] studies and the fabrication and testing of nanodevices[4]. To produce nanometer level positioning over long translation ranges, this fine motion stage will be mounted onto a coarser long-range slide and used to dynamically remove motion errors. For current applications it is envisaged that stacked, closed-loop controlled systems (i.e. a fine-motion stage mounted upon a long-range slide) will be used for precise positioning to provide long-range, single degree of freedom linear translations ranging from 50 mm to 1 m with nanometer-level error compensation.

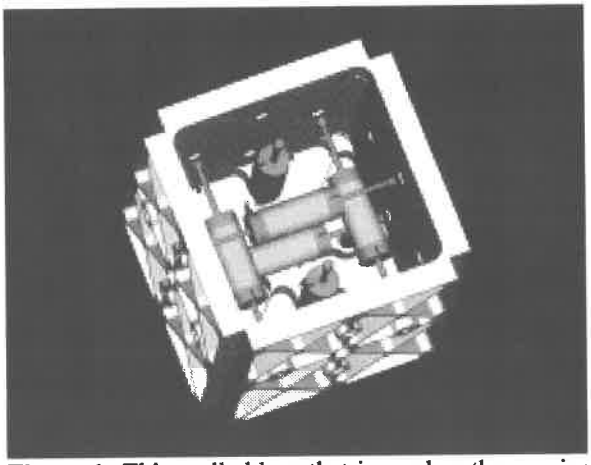

Figure 1: Thin-walled box that is used as the moving platform viewed from the inside and showing the 2-2-2 strut design using three orthogonal actuator pairs.

2.0 Instrument Design

The current stage consists of a monolithic moving platform attached to a rigid base via three actuator pairs positioned orthogonally with each pair producing a translation in the plane, and directed along, the actuator axes plus a rotation perpendicular to this plane. The 2-2-2 strut design has been chosen in order to decouple the system enabling translation or rotation in any single plane of motion using a single actuator pair, see Figure 1. Maintaining the symmetry of the system around the center of gravity of the stage required that the length of the actuators be approximately as long as the dimensions of the stage shell.

The actuators comprise 12.7 mm diameter, 25.4 mm long and 1.6 mm thick piezoelectric (EDO EC64) tubes that produce a maximum translation of 1.7 μm with an excitation of 1,000 V. In practice motion control resolution is limited by the precision of the drive system, which is of the order 1 part in 10,000. With the voltage amplifier used for these experiments a broad bandwidth noise of amplitude of around 18 mV $Hz^{-1/2}$ superposed with a 60 Hz carrier of amplitude 17 mV. Each actuator consists of two, brass, rod-type flexures bonded to each end of the tube with all axes collinear. These flexures produce a high stiffness in the axial direction and low stiffness in the off-axis directions. The actuators are mounted by small collets to the moving platform while the other end is mounted using squeeze clamps to a base structure. The previously mentioned mounting techniques were employed for easy interchange of actuators.

Due to the complexity of the system and the large number of interfaces between the mounting base and the stage supporting shell, it is not possible to assess the manufacture and assembly errors in terms of the residual forces in the actuators after assembly. To evaluate performance, a test fixture[5] was designed and built to test the actuators through a full range of motion. The test fixture incorporates the same collet and squeeze clamp mounts along with a preload mechanism to simulate the effects of the counteracting stiffness of the other five actuators and off-axis deformations of assembly due to the cumulative effects of manufacturing tolerances along with payload. The test fixture employs one capacitance-based displacement gage (Lion Precision, MN) for measuring the axial displacement of the actuator and two LVDTs to measure respectively the applied off-axis deformation of the actuator and axial preload. Figure 2 is a schematic representation of the parameters being evaluated. The test fixture allows for low stiffness in the actuator displacement direction while providing the opportunity for lateral translation of the actuator simulating the motion of other axes. The system was also designed to

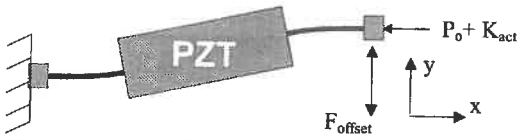

Figure 2: Actuator test parameters.

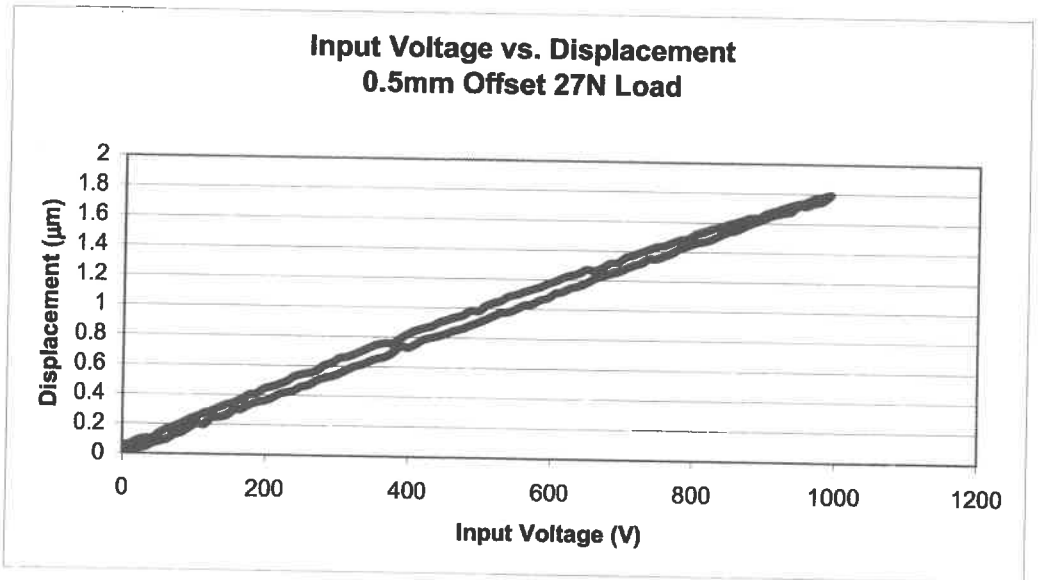

Figure 3: Initial actuator prototype test results for a 27.4 N axial load and a 0.5 mm lateral offset. Actuator tested through a full range of motion (0-1000 V).

incorporate a variable preload mechanism to simulate different payload capacities. The initial tests of a prototype actuator under a 27.4 N load, $2.74 \cdot 10^4$ N m^{-1} stiffness and a 0.5 mm lateral distortion yielded a displacement of 1.6 μm representing roughly a 6 % less than that obtained during a 'free' translation. For this particular PZT material, the hysteresis of the actuator was found to be 10 %, which is considerably lower than that usually observed with material having longer displacement ranges. A plot of the displacement as a function of input voltage is shown in Figure 3.

The upper platform is a thin-walled cubic shell using reinforcing ribs to increase the natural frequency and overall stiffness of the stage platform. To limit the mass of the moving platform a wall thickness of 1 mm was used throughout the shell. Finite element analysis was utilized for the verification of the design concept. To simplify the modeling process, a finite element model was constructed from plate elements. The utilization of plate elements required the development of a modeling technique that would account for the stiffer areas created by the fillets during the machining process[6]. The subsequent technique was employed to model the stage platform with the purpose of determining the resonant frequencies and mode shapes as shown in Figure 4. A comparison between the finite element model and the machined platform yielded results of 1101 Hz and 1184 Hz respectively. Finite element models of the actuators have also been developed for the evaluation of the system performance results of which will be published in the near future.

Figure 4: Finite element model of the first resonant mode at 1101 Hz of the moving platform.

A full set of six actuators was assembled and tested utilizing the same techniques previously mentioned. The base structure consists of five interlocking members that are bolted together to form a rigid foundation for the stage system and has been designed in a modular fashion such that the system can be assembled from the inside out. A picture of the stage components prior to assembly is shown in Figure 5.

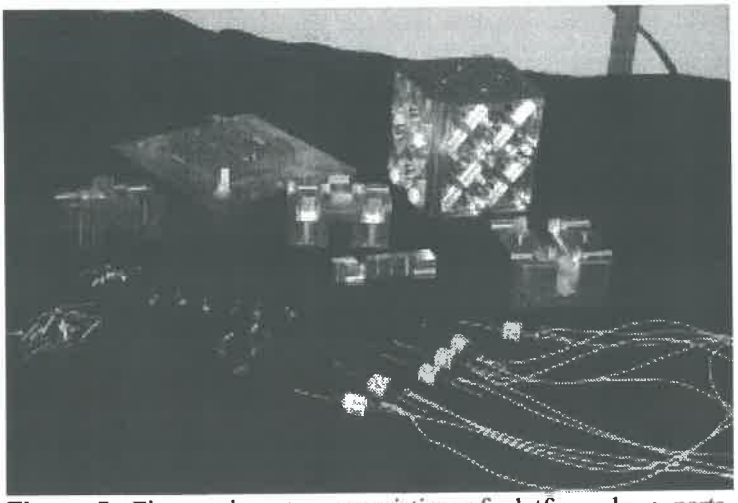

Figure 5: Fine-motion stage consisting of platform, base parts, actuators, collets, and squeeze clamps prior to assembly.

3.0 Results

After assembly, the fine-motion stage was evaluated by rigidly mounting a 50.8 mm (2 inch) aluminum cube to the top of the moving platform to serve as a target for six Lion Precision™ capacitance gages. The capacitances gages had a sensitivity of 2 V μm^{-1} and a measurement

Figure 6: Capacitance gages monitoring aluminum cube rigidly fixed on the top of the moving platform of the fine-motion stage.

uncertainty of ± 5 nm. The gage pairs were mounted in an aluminum bridge and oriented to be colinear with the placement of the actuator pairs, as seen in Figure 6. During the translation and rotation tests all six capacitance gages were monitored over the full range of motion (0-1000 V) for all actuators in translation and rotation. The goals of these evaluation tests were to verify the range of motion and dynamic response of the complete stage.

To test translation of the stage, equal voltage was applied to one actuator pair while the other two were left open-circuit. The same tests were performed for each

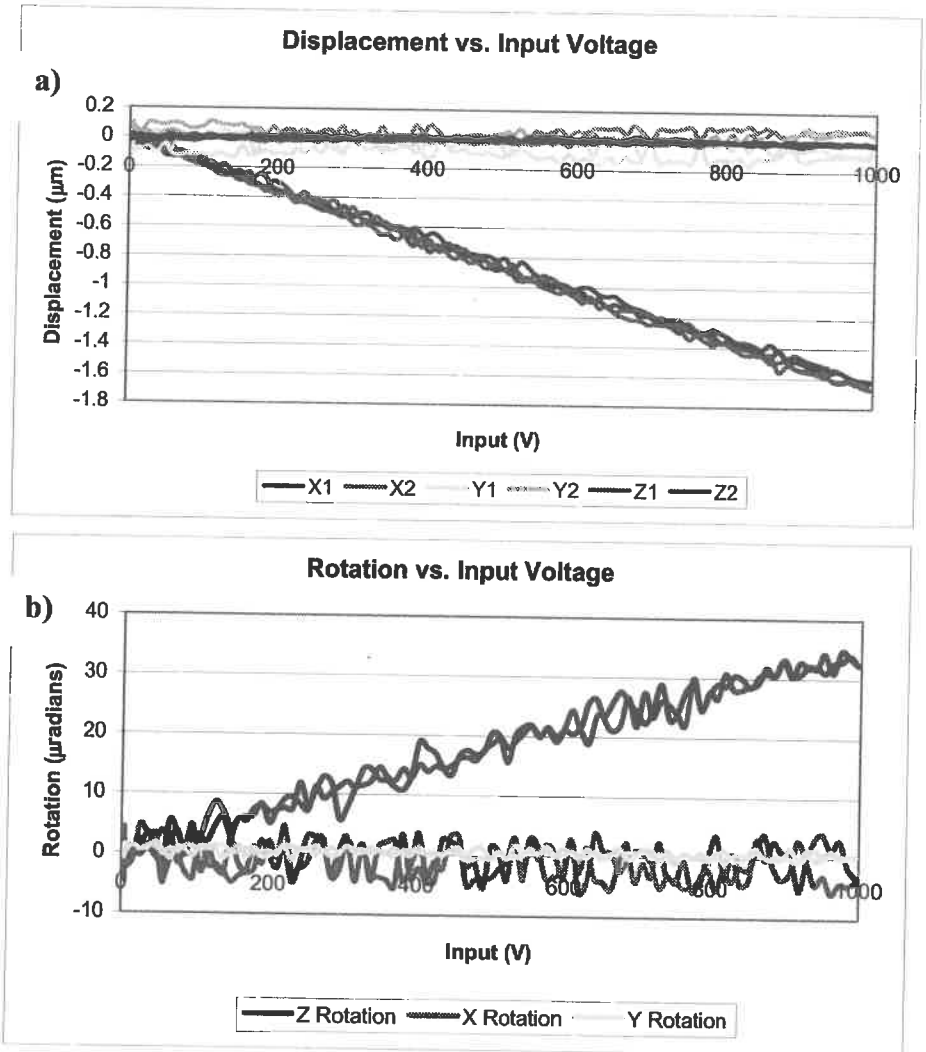

Figure 7: Results from measurement of translation and rotation produced by a single actuator pair, a) Plot of the displacement of the x-axis. b) Plot of the rotation about the z-axis.

plane of motion. In these translation tests the stage displaced approximately 1.6 μm with small amounts of cross-coupling in the other axes as shown in Figure 7a. A similar evaluation process was used for rotations. A single actuator was displaced causing a subsequent rotation about the actuator in parallel. A rotation angle of approximately 35 μrad, again with only small amounts of cross-coupling seen in the other axes, is shown in Figure 7b.

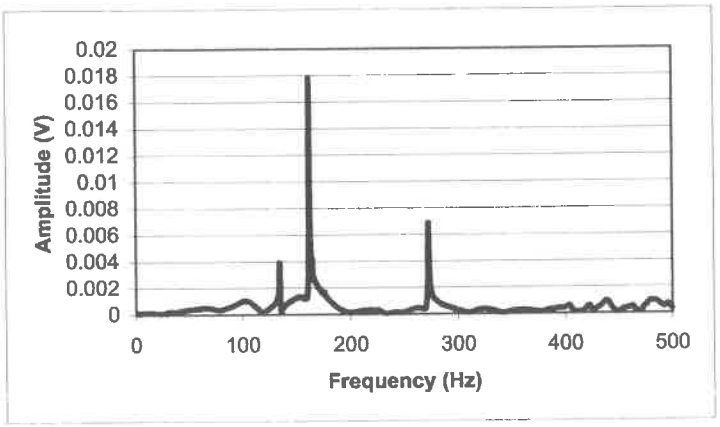

Figure 8: Dynamic response of the stage system with a fundamental resonant frequency at 162 Hz with a relatively large 0.650 kg payload.

Utilizing the same experimental setup, the dynamic response of the system was evaluated. The fine-motion stage was excited by an impact force, and the subsequent motion of the stage was recorded. The fundamental resonant frequency was found to be at approximately 162 Hz as shown in Figure 8. The payload of the aluminum target structure was measured to be 0.650 kg, which, combined with a platform mass of around 0.350 kg, would explain the low resonant frequency.

4.0 Work Ongoing

Currently the fine-motion stage is undergoing evaluation at NIST. To increase precision, a control system using laser interferometry as the prime feedback source is being developed. Future developments include; an assessment of optimal controller strategies to achieve sub-nanometer control, design and implementation of vacuum compatible passive damping treatments and design of thin-walled structures to optimize stiffness and dynamic response. A mechanism for evaluating the properties of some inherently damped elements is currently being undertaken. It is envisaged that results from this work will be used to produce a second prototype translation stage towards the end of this year.

References

[1] U. Bonse and M. Hart, 1965, An x-ray interferometer, *Appl. Phys. Lett.*, **6**, 155-156

[2] M. Hart, 1968, An Ångstrom ruler, *Brit. J. Appl. Phys., (J. Phys. D.)*, **1**(2), 1405-1408

[3] Freitas, Robert E., 1999, *Nanomedicine, Volume 1: Basic Capabilities,* Landes Bioscience, 509 pgs., ISBN: 157059645X.

[4] DOE report: Nanoscale Science, Engineering and Technology Research Directions, pg 41, 57.

[5] Roy H.R. Jacobs, 1999, Design process of the PZT-Flexure Testing Device,report no. PE99-040, Technische Universiteit Eindhoven, Department of Mechanical Engineering, Precision Engineering section, The Netherlands

[6] Seugling, R. M. and Brown, A. M., 2001, Modeling of Fillets in Thin-Walled Structures for Dynamic Analysis, *Proc. International Modal Analysis Conference*, Vol. **19**, 379-384.

Methods and Results of Reducing Following Error in the LLNL Large Optic Diamond Turning Machine

D. J. Hopkins
Lawrence Livermore National Laboratory
7000 East Ave MS/L-792
Livermore, CA. 94550

The USAF Integrated Flight Experiment (IFX) Project is part of the development of the Space Based Laser (SBL) Program. The LLNL Large Optics Diamond Turning Machine (LODTM) is responsible for diamond turning the aspheric laser cavity mirrors. These large optics must be manufactured to micro-inch tolerances. The optics are made of silicon to minimize cooling requirements and weight in the SBL. Diamond turning silicon presents many challenges to the LODTM; one of which is silicon's anisotropic property. When cutting these cones shaped optics, the machine sees many different crystallographic planes of the silicon. These planes present different degrees of material hardness. The tool is held in position but it experiences a force variation as it cuts across the different crystallographic planes. This force variation is reflected back into the machine control system and presents a dynamic disturbance that increases the servo system following error. The affect of this error is to cut a part that is not round but "squareish", i.e. at the micro-inch level.

Two methods were used to reduce the following error or increase the machine dynamic stiffness. Each method relies on the fact that the cutting process is cyclic. The two methods are described below.

- Method one increases the machine dynamic stiffness and reduces the following error by increasing the servo system bandwidth and the loop gain at the disturbance frequency. The paper discusses how the servo compensation filters were designed to accomplish this goal. The reduction of following error by this method proved very successful and is reported in the paper.

- Method two uses an adaptation of a proprietary controller developed by the Structural Dynamics group of the Lockheed Martin Corporation (LM). The system, know as the DECS controller, works in addition to the present LODTM control system. It observes the LODTM following error and generates a correction signal that adaptively removes any cyclic following error. The DECS controller was originally developed for dither control of telescope IR secondary mirrors. (The Keck telescope and some other observatory telescopes use this system.) The particular DECS algorithm is not discussed in the paper, as it is a proprietary algorithm of LM, however, the results of applying this technology to the LODTM is presented in the paper.

Together, both of these methods have reduced the LODTM position following error to the required micro-inch tolerances. The following error reduction has been shown even at relatively high disturbance frequencies with respect to the servo system bandwidth. Applying these two methods to the LODTM, the machine control system [2] following error is reduced to a level that no longer contributes to part contour error. With essentially no control system error, additional process issues and machine error sources have been identified.

[1] Donaldson, R.R. and Patterson, S. R., "Design and Construction of a Large Vertical Axis Diamond Turning Machine", SPIE's 27th Annual International Technical Symposium and Instrument Display; Aug. 1983

[2] McCue, Howard K., "The Motion Control System for the Large Optics Diamond Turning Machine (LODTM)", SPIE's 27th Annual International Technical Symposium and Instrument Display; Aug. 1983

Key words: diamond turning, following error, servo system, dynamic disturbance

The design of the Kolibri DVD-actuator.

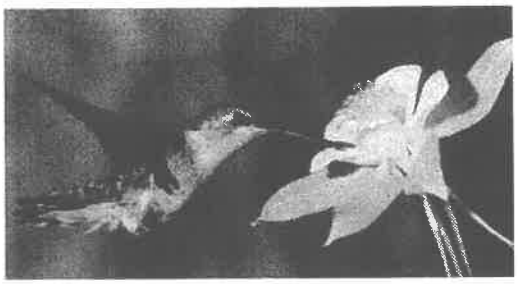

F.G.A. Homburg.
Philips Optical Storage
Optical Recording Development.

21-10-1998
VVR-42-AH-98004

Introduction.
In any optical drive a laser beam is focused on to the disc trough an objective lens. As the disk is far from perfect the lens has to be actuated in two directions, the focus (vertical) direction and the tracking direction (horizontal). From the reflected laser beam both the data signal and servo signals are derived. A rough indication about the required accuracy's is 1 μm in focus direction and 100 nm in tracking direction. The servo loops used to position the lens have a typical bandwidth in the order of 1 to 5 KHz. The device to actuate the lens is the 2D lens actuator. In this article a number of main design decisions are described in the process of defining a new generation of lens actuators. It will be only a small part of the story, however most important, manufacturing and process aspects are not addressed here.

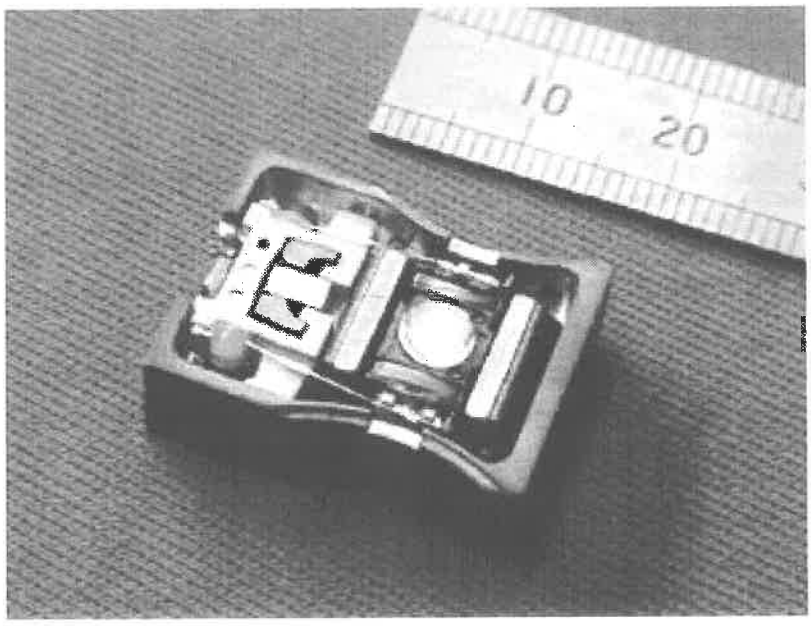

Fig. 1 The Kolibri actuator

The current design.

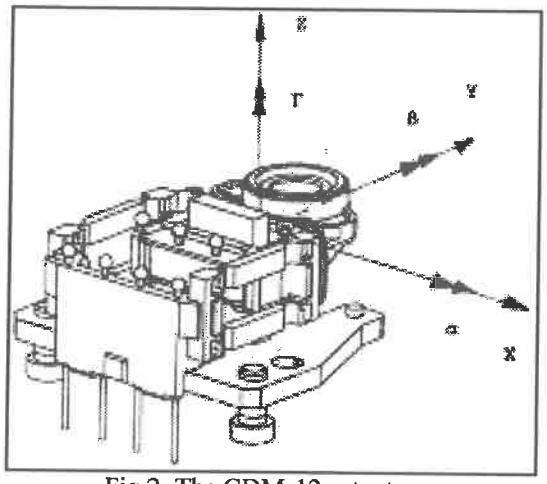

Fig.2 The CDM-12 actuator

The basis of our current actuators is the CDM-12 actuator. It's design is from about 1991. In that time it was meant to be a low cost, low spec actuator for cheap audio applications.
The actuator is based on a electro dynamic drive system with a single magnet and two coil sets for the two actuation directions. The coils are connected to the lens. This moving part is suspended with plastic hinges to the stationary world.
The CDM-12 has an asymmetric design: There is a single drive system and the lens is not near the center of gravity. This makes a cheap solution but also gives the optical designer great accessibility of the lens in various directions. The electrical connections to the coils are made with four separate litze wires. Two adjustment screws are present to adjust the lens tilt angles with respect to the beam direction. A typical height of this actuator is 12 mm calculated from the bottom of the disk to the bottom of the base plate. From this design several ancestors are derived, notably for high speed CD-ROM and CD-Recordable/Rewritable applications. The current level of production is now about 20 million units a year.

Limitations of the current design.
Several limitations of the current design became apparent in the more demanding newer applications. These limitations should be addressed in a new design.

Size.
In the market is a clear trend towards flatter designs, mainly to accommodate for notebook ROM applications. This meant that for new designs a maximum building height of 7 mm.

Bandwidth.
The current actuator design is suitable up to a bandwidth of 3 KHz. The limitation of the bandwidth is found in modes of the lens holder in the frequency range of 10 KHz.
In the newest CD-ROM drives disk speeds are reached of 40 times the normal audio CD speed, approximately 7000 RPM. For DVD disk speeds are not as high but the track pitch on the disk is halved, requiring a much smaller servo error. For both cases the obtainable bandwidth should be increased above 5 KHz.

Tilt sensitivity.
A major problem in optical drive design is lens tilt An objective lens must be kept parallel with respect to the disk surface. If not so the light spot on the becomes 'blurred' and quality of the resulting signals from the optical system is detoriated. For normal CD the allowed angle error is in the order of ± 5 milliradians, for DVD ±1 mrad is required!
Power consumption
The requirement for a high bandwidth also leads to a high power dissipation in the actuator and the power driver. A level of 0.5 to 1 Watt is possible, leading to an undesirable temperature rise. Problems arise mainly in the focus loop.

Yaw sensitivity
A more obscure problem is the yaw sensitivity. Fig. 3 shows a top view of a part of the drive. The actuator is suspended elastically on a sledge. That sledge is guided on a shaft with sliding bearings with a certain amount of play.

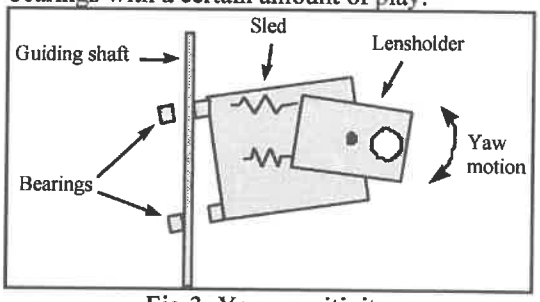

Fig 3. Yaw sensitivity.

If for some reason the sledge rotates instantaneously through the play the actuator *yaw* mode is excited. The lens holder starts to rate about a vertical axis through the center of gravity. If the play in the bearings is about 20 µm (a rather tight fit in our technology) and the distance between the bearings is 20 mm the rotation of the lens holder is excited with a step of 1 mrad. The lens holder starts to oscillate with the eigenfrequency of the yaw mode of

about 1 KHz and an amplitude of 1 mrad. The distance of the center of gravity and the lens is 5 mm so the lens oscillates with an amplitude of 5 μm. This error is so large that the servo system loses track. In practice this phenomenon is seldom encountered. In a read-only system a recovery procedure is started and the user will never notice the problem. If one is writing a recordable disk, the disk is damaged and data may be lost.

Stability.
The CDM-12 actuator has plastic suspension hinges. This makes the actuator extremely robust. Also the designer has a lot of possibilities to influence the performance by changing the position of the films and the thickness of the films. However using plastic makes the design not inherently stable. For designs with small beam diameters and for DVD the stability must be improved.

Laws of scale applied to the current design.
As there is a trend in our world towards flatter designs (notebook CD-ROM) and higher specifications (DVD) the need for a new design became apparent. One of the ideas was just to make the current design smaller. By applying simple scale laws the performance of such a design can be easily calculated.
Four parameters are studied: Eigenfrequencies, efficiency, DC-power use and electrical time constant.

Eigenfrequencies are calculated with formulas like:

$$\omega_0 = \sqrt{\frac{c}{m}}$$

The mass m is proportional with the volume and scales with the third power of the scale factor x. The most simple equation for stiffness is the longitudinal stiffness of a bar.

$$c = \frac{E*A}{l}$$

The modulus of elasticity does not change, so the stiffness is proportional with length and scales with x.
Therefore the eigenfrequency is proportional to the inverse of the scale factor:

$$\omega_0 \approx \frac{1}{x}$$

This is favorable, by making the lens holder smaller one gets a stiffer coupling from driving coils to the lens.

The *efficiency* is a number indicating the amount of acceleration one gets for a certain electrical power level. It is expressed in g/√watt. The efficiency number is related to K^2/R of rotating DC-motors.

$$\eta = \frac{K}{m*g*\sqrt{R}}$$

K is the force constant in newton/ampère, m is the mass in kg, g is the gravitational acceleration and R the electrical resistance of the coil in. K can be written as:

$$K = B*n*l_{eff}$$

B is the magnetic flux density in tesla, n the number of windings l_{eff} de effective wire length in meter.
B is independent of the scale. With constant wire diameter the number of windings is proportional with the cross sectional area of the coil, so n is proportional with the square of x. For K can be written:

$$K \approx x^2*x = x^3$$

The electrical resistance is calculated with:

$$R = \rho*\frac{l*n}{A}$$

ρ is specific resistance in ohm/meter, A cross sectional area of a single wire, l the length of a single winding and the number of windings. A and ρ do not scale so:

$$R \approx x^3$$

Combining these formulas results in:

$$\eta \approx \frac{1}{\sqrt{x^3}}$$

Making the actuator smaller also improves the efficiency.

DC power is mainly dissipated to compensate for mechanical offsets an slowly varying disk errors.

the actuator displacement is given by:

$$z = U * \frac{K}{c * R}$$

U is the voltage over the actuator and c is the stiffness of the suspension.
The dissipated power is:

$$P = \frac{U^2}{R} = \frac{c^2 * z^2 * R^2}{K^2 * R} = \frac{c^2 * z^2 * R}{K^2}$$

The stiffness of the suspension is limited by practical considerations and cannot be made much lower so we keep it constant. Also z is determined by the drive and is kept constant.

$$P \approx \frac{1}{x^3}$$

DC-power is going in the wrong direction!

De *electrical time constant* is the quotient of inductance and resistance.

$$\tau = \frac{L}{R}$$

The inductance of a coil is given by:

$$L = \mu * \frac{n^2 * A}{l}$$

μ is the permeability, n the number of windings, A the enclosed area in the coil and l the length of the coil. Inductance is proportional with x^5. R was proportional with x^3.
So:

$$\tau \approx x^2$$

A small time constant gives less phase shift in the servo. Making the coil smaller is also an improvement.

Conclusion: Making the actuator smaller improves things, but you should take care for z-offsets because of the DC power.

Design decisions.
In a compact design as an actuator it is difficult to tackle a problem separated from other problems. A solution here will inevitably have drawbacks elsewhere.
Some of the design decisions are clarified next:

Bandwidth.
The current actuator design is suitable up to a bandwidth of 3 KHz. If one decreases the dimensions of the actuator with a factor of $\sqrt{2}$ the mass reduces with a factor of 0.36. This is a quit drastic measure, the current mass of 600 mg becomes 220 mg. The obtainable bandwidth increases only with a factor of 1.41=4.2 KHz. This gain in bandwidth is clearly not enough. Just scaling down the design will not give the required bandwidth.

Actuator suspension
A solution for the stability problem is the use of a metal suspension. If one uses a rather standard configuration with four thin parallel beams torsion stiffness will not be enough. A tapered design will improve this.
Metal beams can also be used to connect the coils electrically.
The mechanical damping of a metal spring suspension will be very small, so a separate damping system must be provided.
Furthermore, metal springs are much more fragile than its plastic counterparts.

Symmetry
In fig 3. the solution for the yaw sensitivity problem is easily been seen, just move the lens to the center of gravity. The system is becoming very robust for errors in the sledge guidance. Of course there is a drawback. An actuator should be driven with a force through the center of gravity to avoid unwanted rotations. With the lens at the center of gravity one needs a double magnet system to accomplish this. In a flat design the optical system is built not below but alongside of the actuator. A symmetric drive configuration generally blocks the light path. In the Kolibri design this is solved with the so called light gate.
Also a symmetric design has the possibility of a very close mechanical coupling between coils and objective lens resulting in a high possible bandwidth.

Moving coil vs. moving magnet
A system with a stationary coil set and moving magnet(s) looks the most simple design. In this case there is no need for a dynamic electrical connection with the moving part.
The efficiency of moving coil system is generally better than a moving magnet system.

Yoke system
In an actuator acceleration is generated with electro dynamic forces on the moving lens

holder. Reaction forces however are exerted on the stationary part of the actuator and from there in the rest of the drive. This may lead to stability problems due to unwanted mechanical feedback.
In the CDM-24 actuator the yoke is suspended elastically to filter out the disturbances. In practice this solution has tolerance problems in the production line.
If one chooses a symmetric design with multiple magnet systems the design of such a suspension becomes quite difficult.
However, if the moving mass of the actuator is small with respect to the rest of the mechanics the acceleration forces are relatively small and a yoke suspension will be superfluous.

Description of the Kolibri design.
The final design of the prototype is shown in the last figure.
The *objective lens* and a *dichroic diaphragm* are mounted in the *lens holder*. On the lens holder the *focus coil* and a set of *tracking coils* are wound. The focus coil is lifted in the front surface of the lens holder. This is the *light gate* and makes it possible to mount the rest of the optics in the same plane as the actuator.
The *suspension block* contains the *wire springs* and is made with an insert molding technique. The suspension block is connected with the lens holder with four laser welds making both a mechanical and an electrical connection.
At the back of the suspension block are four positions where a droplet of *damping gel* must be applied.
The suspension block has a special interface with a mating part of the *sledge*. With two adjustment *screws* the tilt of the actuator can be adjusted. The position of the lens remains the same during that movement. This reduces the required actuator stroke. A *spring clip* holds suspension block together with the sledge before the angles are fixed with glue.
From the bottom of the sledge the *yoke* with its *magnets* is mounted. One should expect a double yoke system, but because of the light gate the front and back yoke part had to be split and four little magnets are mounted.

Conclusion.
In this moment the first prototypes are tested and the underlying models are verified. the results are promising and it is believed that this design will be the base of the new generation of Philips actuators.

Acknowledgments.
The design of an actuator is rally the work of a team, but at the risk of doing short to the other team members I have to mention Ben Stinesen who has done a extremely fine job in making the total mechanical design of the Kolibri.

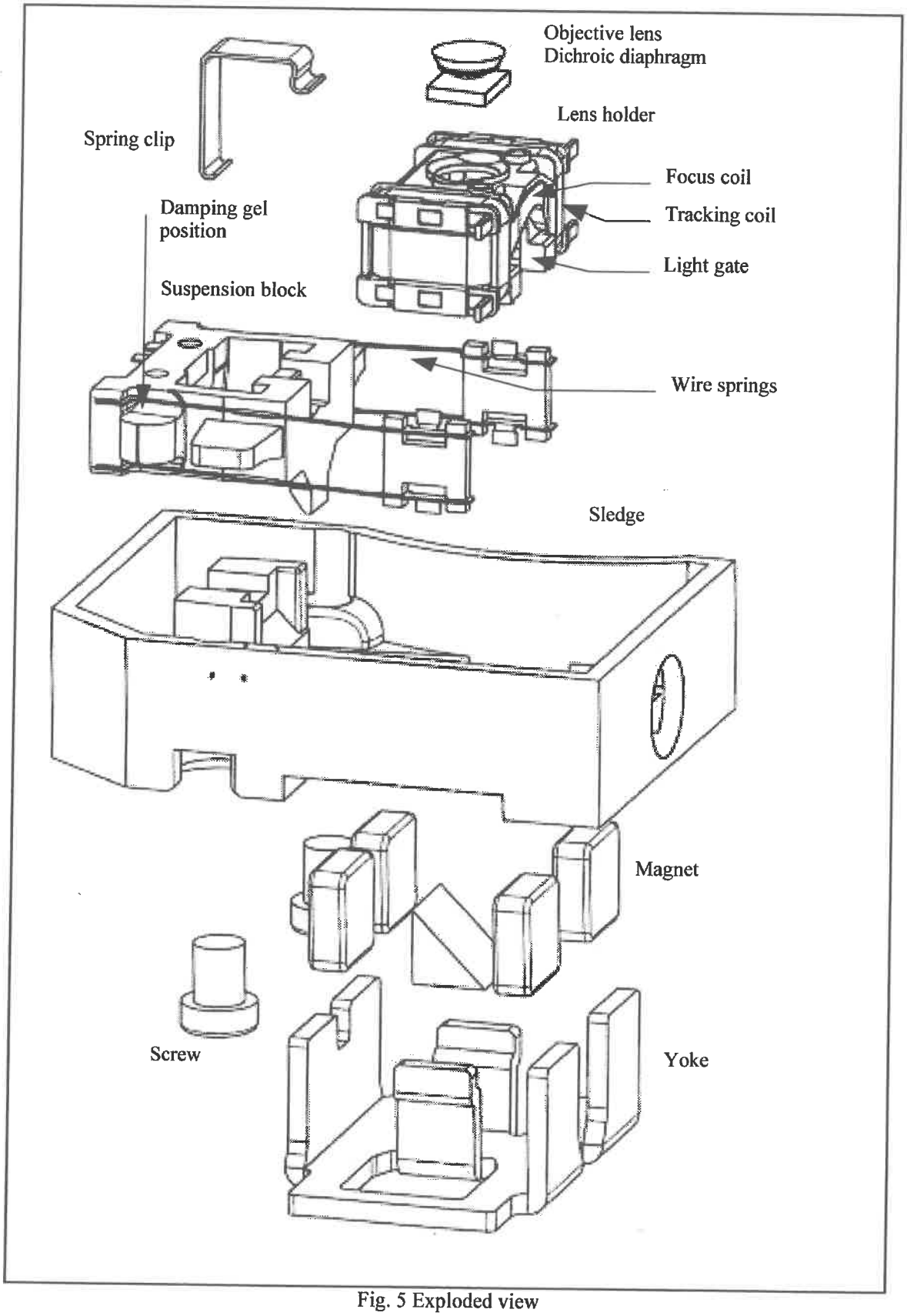

Fig. 5 Exploded view

SUBMICROMETER FRICTION COMPENSATION USING VARIABLE-GAIN SLIDING MODE CONTROL

Paul I. Ro
Precision Engineering Center, North Carolina State University, Box 7910, Raleigh, NC 27695 USA
Wonbo Shim
Seagate Corp

ABSTRACT

The paper discusses a sliding mode control suitable for compensation of nonlinear microdynamic friction and parameter changes in a ball-screw driven slide system. The conventional, fixed-gain sliding mode control has a limited range of performance in the presence of varying nonlinear friction in sub-micrometer trajectory tracking. In this work, an algorithm that effectively calculates variable switching gain based on the observation of parameter variation and friction disturbance is proposed. To verify the effectiveness of the proposed algorithm, the comparison with the conventional slide mode control is presented and experimentally verified. It is shown, from the result of this work, that a variable switching gain was critically important in compensating for varying nonlinear friction in the sub-micrometer motion range for ball-screw driven systems.

1. INTRODUCTION

Friction in mechanical system is a nonlinear phenomenon that complicates the control design process and reduces the positioning and tracking accuracy in motion control applications. Much work has been done to characterize and compensate for the nonlinear friction behavior (Armstrong-Helouvry et al., 1994).

As the requirement in positioning and tracking accuracy becomes more stringent, a need for a model that accurately predicts the behavior of friction in microdynamic range (usually below 1.0 micrometer for precision ball-screw systems) became apparent. Futami et al. identified the three dynamic regions (microdynamic, transition, and macrodynamic) of friction characteristic, using a single-axis stage mechanism and achieved nanometer positioning by designing a controller around each region (Futami et al., 1990). In Ro and Hubbel's work (1993), a piece-wise linear friction model taken from a hysteretic torque-displacement curve was used in devising a model reference adaptive control of a ball-screw driven system both in microdynamic and macrodynamic regions. Nanometer positioning under static loads was also achieved using a parallel mechanism of lead-screw driven table fitted with a secondary voice coil actuator (Awabdy, Shih, and Auslander, 1998). In the same work, the microdynamic behavior was modeled by a modified Dahl friction relationship and mainly dealt with a secondary voice coil actuator that has good linear input-output characteristic.

Canudas et al. proposed a new nonlinear analytic friction model that captures most of the frictional behaviors that have been observed experimentally (de Wit et al., 1995). The behaviors include Coulomb friction, Stribeck effect, hysteresis, and spring-like characteristic under microdynamic stiction region. Canudas and Lischinsky illustrated the application of adaptive friction compensation on a DC motor servomechanism based on their model (de Wit and Lischinsky, 1997). Submicrometer positioning and tracking for a ball-screw driven slide system was achieved by compensating for the friction using the new friction model (de Wit et al., 1995), with good results (Ro, Shim, and Jeong, in press; Awabdy, Shih, and Auslander, 1998).

For a typical mechanical system, inertial parameters are known only to a certain degree, and the change of actual friction is very difficult to be modeled accurately. In the current research, an algorithm that effectively calculates the switching gain based on observation of parameter variation and external disturbance is proposed. Nonlinear friction is modeled based on the friction model (de Wit et al., 1995), and sliding mode control with an effective algorithm to vary the switching gain is proposed for positioning and tracking for a ball-screw driven slide system. Performances of the proposed algorithm are verified through experiments.

The paper is organized as follows: In section 2, the experimental setup and preliminary tests for identifying the friction behavior of the system are described. The corresponding dynamic model of the system is described based on the friction behavior. Then, Section 3 shows the derivation of the sliding mode control based on the system model and the Canudas' friction model. The experimental results verifying the performance of the proposed control algorithm are shown in Section 4. The conclusions are then followed in Section 5.

2. SYSTEM MODEL

A simple conceptual model for the system was developed in Figure 1 that shows the idealized model of the mechanical components of the system. In the current system setup, as seen in Figure 1, the slide position, x_2, is the only state measured by a laser interferometer. The slide velocity, $\dot{x}_2$, is gathered digitally by first order difference of x_2. The nut position and its velocity, x_1 and $\dot{x}_1$, are not measurable. The built-in tachometer can be used for measuring the angular velocity of the ball-screw but the signal output is very noisy. The tachometer signal is usually good for motor speeds orders of magnitude greater than that used in submicrometer motion. The ball-screw rotation and its angular velocity, θ and $\dot{\theta}$, are thus estimated. The unmeasurable state variables, x_1 and $\dot{x}_1$, are estimated by a Kalman filter (Ro, Shim and Jeong, in press).

The significant parameters for the dynamic system are listed in Table 1.

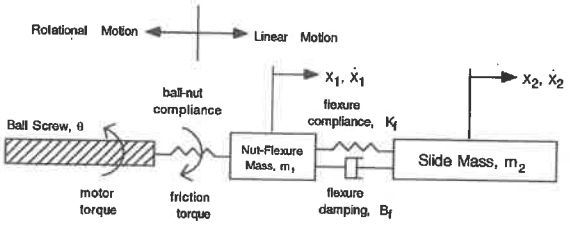

Fig. 1. Conceptual model of mechanical components in the system

The rotational dynamics of ball-screw may be describes as

$$(J_{rot} + (m_1 + m_2) l_P^{\,2}) \left(\frac{\ddot{x}_2}{l_P} \right) + F(\cdot) = u(t) \qquad (1)$$

where J_{rot} is the total rotational inertia of ball-screw and motor, l_P is the lead pitch of the ball-screw, $F(\cdot)$, is an equivalent frictional torque, and $u(t)$ is input torque to the system. Since the frictional torque on the ball-screw dominates the system and the motor torque transmission mechanism has high stiffness, the following reduced-order (nominal) model for the rotational motion is investigated for the controller design:

$$J\ddot{\theta}(t) + F(\cdot) = u(t) \qquad (2)$$

where J is an effective inertia of ball-screw, motor, and equivalent rotational inertia of the linear masses; $F(\cdot)$ is the equivalent friction torque caused by motor brushes, support bearing, and nut interfaces; and $u(t)$ is the motor toque generated by a current controlled servo-amplifier driven by voltage command from a DSP.

Table 1. Experimental system parameters

J_{rot}	Rotational Inertia	5.94×10^{-5} Kg·m^2
M_1	Nut-Flexure Mass	0.653 Kg
M_2	Slide Mass	11.79 Kg
l_P	Lead Pitch	7.958×10^{-4} m/rad
K_f	Flexure Stiffness	7.1×10^{6} N/m
B_f	Flexure Damping	41.59 N/(m/sec)
K_{Nut}	Nut Rigidity	8.828×10^{7} N/m

For the electromechanical system shown, friction in the ball-screw and nut interfaces is the major nonlinear disturbance that complicates the control design process. The static friction parameters can be estimated from the friction-velocity plot measured during constant velocity motions under a simple PI control. At each discrete point in Figure 2, the corresponding control voltage was measured under control velocity command. By incrementing the velocity command, a well-known static friction profile was obtained as shown in Figure 2. However, as indicated by Figure 2, the control voltage that would initiate the slide displacement has a bias toward the positive-input direction. Figure 3 shows there is a small displacement due to the control voltage of 100 mV, much below the threshold value of 400 mV as shown in Figure 2. Such spring-like behavior appears to result from elastic deformation of the contact patches on the balls (Futami el al., 1990; Ro and Hubbel, 1993). However, as the applied voltage increases, a friction breakaway is observed and the apparent slide displacement begins to occur under open-loop control. The friction behavior of this system is to be modeled as the bristle type friction proposed by (de Wit et al., 1995):

$$\begin{aligned} \frac{dz}{dt} &= v - \frac{|v|}{g(v)}\sigma_0 z \\ F &= \sigma_0 z + \sigma_1 \frac{dz}{dt} + \sigma_2 v \end{aligned} \qquad (3)$$

where σ_0 is the stiffness, σ_1 is a damping coefficient, and σ_2 is a viscous friction coefficient. Friction parameters for controller implementation were estimated based on the experimental result (Ro, Shim and Jeong, in press).

3. SLIDING MODE CONTROL WITH VARIABLE SWITCHING GAIN

The inertial parameter of the system is not perfectly known. Thus, the equation of motion is developed based on the nominal values of the system.

$$(\hat{J} + \tilde{J})\ddot{\theta} + F = u \qquad (4)$$

where $\hat{J}$ is the nominal inertia, $\tilde{J} = J - \hat{J}$ is the estimation error, and F is the equivalent friction torque on the system.

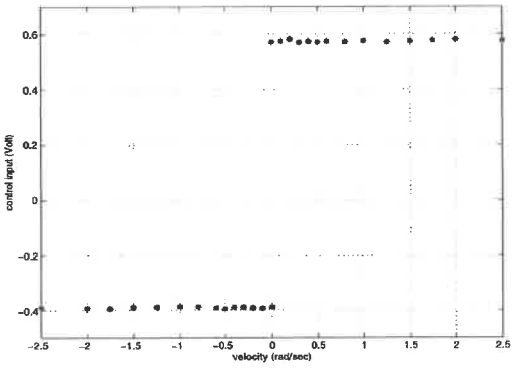

Fig. 2. Friction-Velocity map

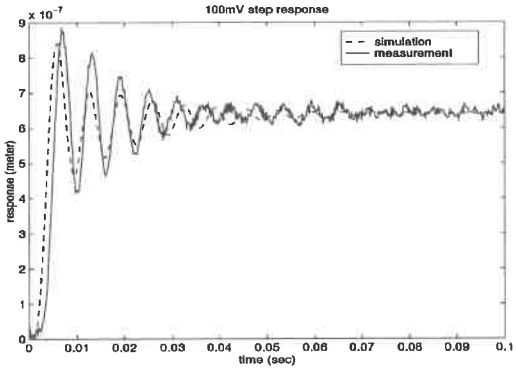

Fig. 3. Open-loop response to 100mV input

In order to have the system track the desired trajectories at the same time, a sliding surface, *S*, is defined as the weighted sum of the tracking error, *e*, and its derivative:

$$S = \hat{J}\left(\dot{e} + 2\lambda e + \lambda^2 \int e\, dt\right) \tag{5}$$

where $e = \theta_d - \theta$, $\dot{e} = \dot{\theta}_d - \dot{\theta}$, and $\ddot{\theta}_d$ is the desired reference displacement twice differentiated. While in sliding mode, the dynamics can be written as $\dot{S} = 0$. By solving the equation (5) formally for the control input, an expression so-called the equivalent control, u_{eq}, is obtained from the following procedure.

From equation (5),

$$\begin{aligned} \dot{S} &= \hat{J}\left(\ddot{e} + 2\lambda\dot{e} + \lambda^2 e\right) \\ &= \hat{J}\left(\ddot{\theta}_d - \ddot{\theta}\right) + \hat{J}\left(2\lambda\dot{e} + \lambda^2 e\right) \\ &= \hat{J}\ddot{\theta}_d - \left(u - F - \tilde{J}\ddot{\theta}\right) + \hat{J}\left(2\lambda\dot{e} + \lambda^2 e\right) \end{aligned} \tag{6}$$

The equivalent control, u_{eq}, that would achieve $\dot{S} = 0$ is thus

$$u_{eq} = \hat{J}\ddot{\theta}_d + \hat{F} + \hat{J}\left(2\lambda\dot{e} + \lambda^2 e\right) \tag{7}$$

where $\hat{F}$ is the friction estimate based on the bristle type friction model.

In order to satisfy sliding condition despite the uncertain dynamic disturbance, *F*, a term discontinuous along the surface, $S = 0$, is added to u_{eq}, and overall sliding mode control law is proposed as follows:

$$u = u_{eq} + K\,\mathrm{sgn}(S) \tag{8}$$

where *K* denotes the switching gain, used to guarantee sliding on the surface, *S(t)*.
From the sliding condition,

$$\frac{1}{2}\frac{d}{dt}S^2 = S\,\dot{S} \le 0 \tag{9}$$

substituting equations (6), (7), and (8) into (9) gives

$$\begin{aligned} S\,\dot{S} &= \left[\left(\tilde{J}\ddot{\theta} + \tilde{F}\right) - K\,\mathrm{sgn}(S)\right]S \\ &= \left(\tilde{J}\ddot{\theta} + \tilde{F}\right)S - K|S| \le 0 \end{aligned} \tag{10}$$

where $\tilde{F} = F - \hat{F}$ is the friction estimate error.
To maintain stability and guarantee certain performance bounds, the switching control gain in equation (10) must satisfy the following condition:

$$K \ge \left|\tilde{J}\ddot{\theta} + \tilde{F}\right| \tag{11}$$

That is, the switching gain must be larger than the absolute bound related to friction disturbance estimate error and parameter uncertainties. Typically, in the design process, it is critical to choose a suitable set of values for control parameters, such as switching gain, *K* and weighting factor, λ, to guarantee good performance. Because of the nonlinear nature of the problem, there is no straight-forward method to determine these values. And trial-and-error is usually the presiding norm (Liu and Handroos, 1999). In this work, an algorithm that effectively calculates switching gain based on the observation of changing inertia and friction estimation error is proposed.

Since a friction model that estimates the friction disturbance is obtained as in (de Wit el al., 1995; Ro, Shim, and Jeong, in press), the control for the nominal system model is calculated using,

$$\hat{J}\ddot{\theta} + \hat{F} = u_m \tag{12}$$

The control, u_m, for the system model is directly calculated from (12), where $\ddot{\theta}$ is calculated as $\ddot{\theta}(k) = \dfrac{\dot{\theta}(k) - \dot{\theta}(k-1)}{T}$, and *T* is a sampling period.
The bound for switching gain can be obtained by subtracting equation (12) from equation (2), which results in

$$\tilde{J}\ddot{\theta} + \tilde{F} = u - u_m \tag{13}$$

$$K \ge |u - u_m| \tag{14}$$

Therefore, if the switching gain is selected as the difference between the control input to the system and the calculated control input based on the nominal model (12), the value of switching gain changes according to the parameter variation and friction estimation error. In practical control implementation, there is always a computational delay in a digital control environment. The control signals can be

easily stored at each sampling period. So, the real implementation signal of equation (13) is given by

$$\Delta u(t) = u(t-T) - u_m(t-T) \qquad (15)$$

where T is the sampling period. A strictly positive constant, η, can be added to the equation (14) to account for the unstructured dynamics to equation (2) and decrease the time constant for reaching the sliding surface. Then, the sliding condition (9) results in (Slotine and Li, 1991),

$$\frac{1}{2}\frac{d}{dt}S^2 = S\dot{S} \le \eta|S| \qquad (16)$$

The control algorithm is serviced at a fast rate of 5 kHz. Therefore, the controlled system using equation (15) performs very close to the ideal case of using equation (13). The approach suggested here is inspired by (Ishiguro et al, 1992; Hsia and Jung, 1995).

4. EXPERIMENTAL RESULTS

The proposed controller was verified for positioning and tracking motion control for the ball-screw driven slide system. The tracking performance of the proposed control algorithm for 1 μm, 2 Hz sinusoidal tracking command is shown in Figure 4, and its corresponding control voltages during the implementation are shown in Figure 5. The control input does not have high frequency adverse effect of chattering. The variable switching gain of the proposed control algorithm is also gathered during implementation and is plotted in Figure 6. The measured control voltages illustrate that, under the proposed control, the control voltages have the approximate positive bound of 0.4 Volt while the negative bound is -0.3 Volt, which are less than the values shown in static friction-velocity relationship of Figure 2. In the work of (Iwasaki and Matsui, 1996; Iwasaki et al., 1999), it is claimed that the nonlinear friction behaved as the simple Coulomb friction under a dynamic table drive motion. However, the result in Figure 5 proves that the nonlinear friction under high precision motion control behaves as the bristle-type friction. The positioning performance of the proposed controller was tested for 1 μm step command, and its response is plotted in Figure 7. The response shows smooth transient behavior and no steady-state error. The step response for 2.5 μm is plotted in Figure 8. The proposed control algorithm shows consistent performances for tracking and positioning.

When the steady-state error is examined from Equations (4), (7), and (8), it can be rewritten as:

$$\hat{J}\left(\ddot{e} + 2\lambda\dot{e} + \lambda^2 e\right) = \left(\tilde{J}\ddot{\theta} + \tilde{F}\right) - K\,\mathrm{sgn}(S) \qquad (17)$$

With the proposed control algorithm, switching gain K is adjusted to compensate for parameter variation and friction estimation error. For instance, the sign of S in the tracking control is positive as seen in Figure 10, and adjusted switching gain K also has positive values seen in Figure 6. With the method in equation (13), the resulting error dynamics (17) can be rewritten as:

$$\ddot{e} + 2\lambda\dot{e} + \lambda^2 e \approx 0 \qquad (18)$$

The resulting steady-state error is expected to have a critically damped behavior. The step command responses show the critically damped behavior as seen in Figures 7 and 8.

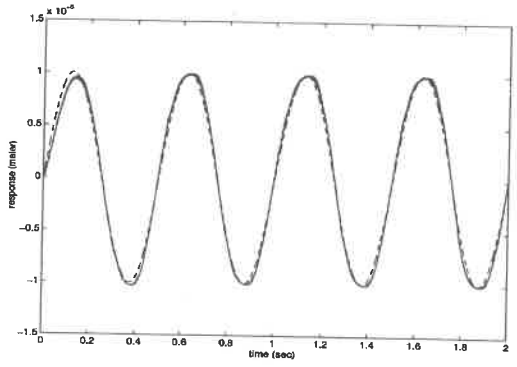

Fig. 4. Tracking performance of the proposed sliding mode control algorithm for 1 μm, 2Hz command (dashed : reference, solid : experiment)

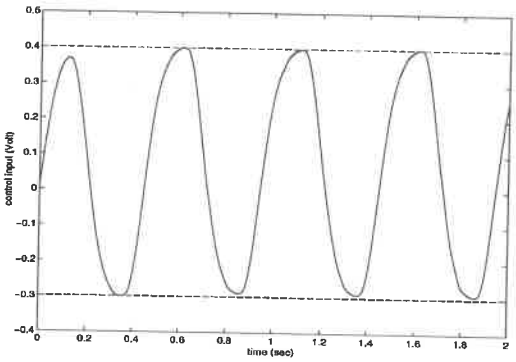

Fig. 5. Control voltages of proposed sliding mode controller with variable switching gain

In comparing with the conventional sliding mode, the appropriate selection of a fixed switching gain was not easy. Therefore, the averaged value of variable switching gains, K=0.1, was selected from the result of Figure 6. The performance of the conventional sliding mode controller with the selected switching gain value of 0.1 is shown for 1 μm, 2 Hz sinusoidal tracking command in Figure 9. The response shows poor behavior of tracking lag and steady state error. The response also shows poor transient behavior at the start of motion. The corresponding control voltages are shown in Figure 10. The highly biased responses in Figure 9 are attributed to the control peaks in Figure 10 when the control gets close to the friction threshold voltage, seen in Figure 2. The result suggests the separate switching gain for either direction be used for further improvement in conventional sliding mode control for the current experimental system. The response for the step command of 1 μm is shown in Figure 11 with the

same switching gain of 0.1. The step response for 2.5 μm command is shown in Figure 12. As in the tracking case, the responses show poor transient behavior and steady state error. For the increased gain of 0.2, experimental studies did not show any performance improvement.

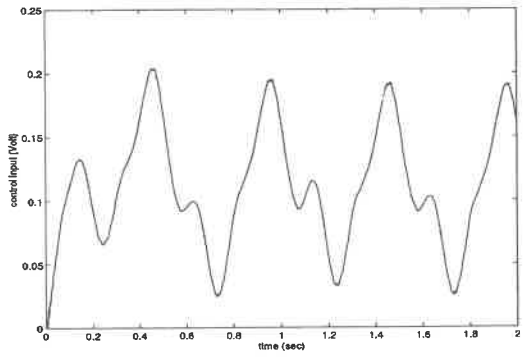

Fig. 6. Variable switching gain during the proposed control implementation

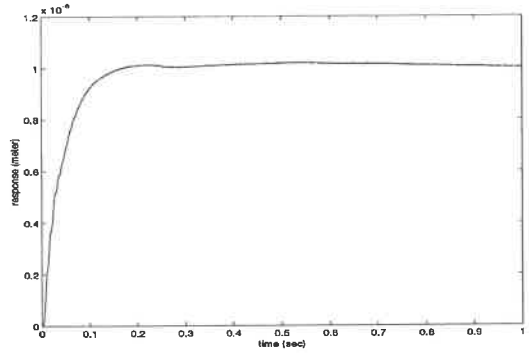

Fig. 7. Positioning response of the proposed controller for 1 μm step command

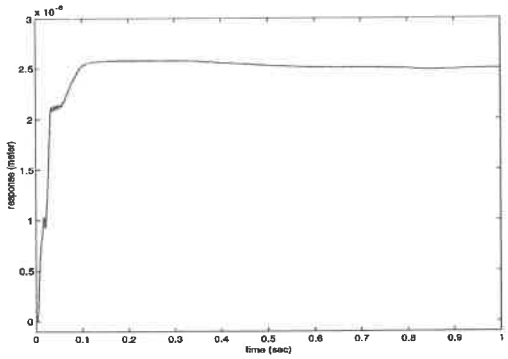

Fig. 8. Positioning response of the proposed controller for 2.5 μm step command

The control voltages of the conventional sliding mode control shown in Figure 10 can be compared with those in Figure 5. The varying switching gain in Figure 6 shows the compensation for the friction estimate error and inertial effect related to uncertain parameters. The positively biased values of the switching gain can also be attributed to the biased behavior of friction relationship of Figure 2.

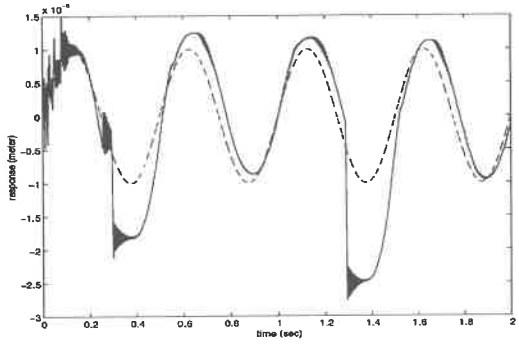

Fig. 9. Tracking performance of conventional sliding mode control for 1 μm, 2 Hz command (dashed : reference, solid : experiment)

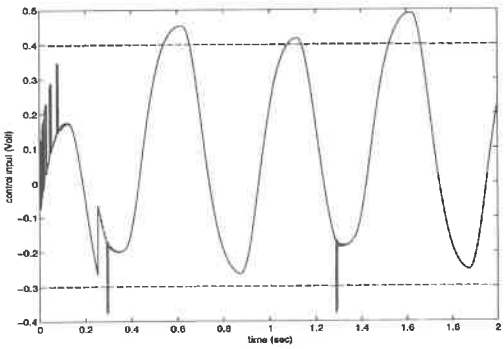

Fig. 10. Control voltages of conventional sliding mode control

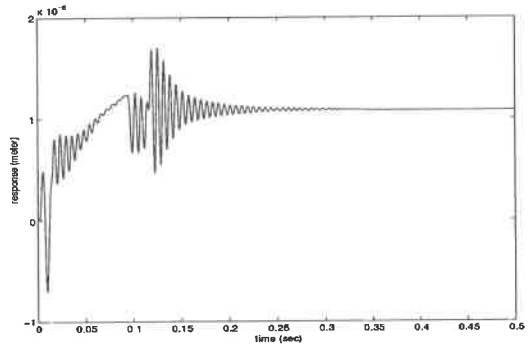

Fig. 11. Positioning response of the conventional sliding controller for 1 μm step command

5. CONCLUSION

To enhance the control performance of a ball-screw driven slide system, a sliding mode controller with a variable switching gain based on the observation of parameter change and friction estimation error was

proposed. Using the proposed algorithm, control action chatter was eliminated. Experimental results verified the effectiveness of the proposed controller compared with that of a fixed-gain conventional sliding mode control. The proposed controller demonstrates consistent performances with positioning and tracking motion control of the ball-screw driven slide system. The robustness issue of the proposed controller with large disturbance is under investigation.

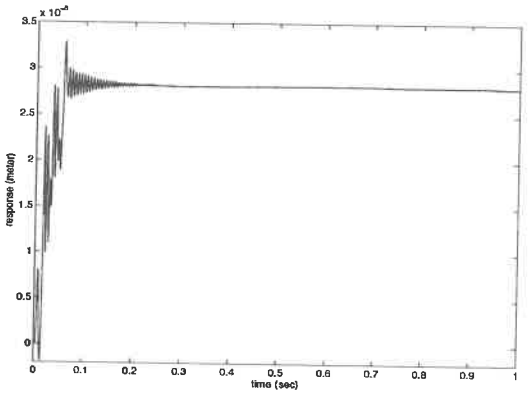

Fig. 12. Positioning response of the conventional sliding controller for 2.5 μm step command

REFERENCES

Armstrong-Hélouvry, B., P. Dupont, and C. Canudas de Wit (1994). A survey of models, analysis tools and compensation methods for the control of machines with friction. *Automatica*, vol. 30, no. 7, pp. 1083-1138.

Awabdy, B.A. W-C. Shih, and D. M. Auslander (1998). Nanometer positioning of a linear motion stage under static loads. *IEEE/ASME Trans. Mechatronics*, vol. 3, no. 2, pp. 113-119.

de Wit, C.C, et al. (1995). A new model for control of systems with friction. *IEEE Trans. Auto. Contr.*, vol. 40, no. 3, pp. 419-425.

de Wit, C.C. and P. Lischinsky (1997). Adaptive friction compensation with partially known dynamic friction model. *Int. J. Adaptive Control and Signal Processing*, vol. 11, pp. 65-80.

Fujimoto, Y. and A. Kawamura (1995). Robust servo system based on two degree-of-freedom control with sliding mode. *IEEE Trans. on Ind. Electr.*, vol. 42, no. 3, pp. 272-280.

Futami, D., A. Furutani, and S. Yoshida (1990). Nanometer positioning and its micro-dynamics. *Nanotechnology*, vol. 1, pp. 31-37.

Gutierrez, H.M. and Ro, P.I. (1998). Sliding-mode control of a nonlinear-input system. *IEEE Trans. on Ind. Elec.*, vol. 45, no. 6, pp. 921-927.

Hsia, T.C. and S. Jung (1995). A simple alternative to neural network control scheme for robot manipulator. *IEEE Trans. on Ind. Electr.*, vol. 42, no. 4, pp. 414-416.

Ishiguro, A. et al. (1992). A neural network compensator for uncertainties of robotics manipulators. *IEEE Trans. on Ind. Electr.*, vol. 39, no. 6, pp. 565-570.

Iwasaki, M. and N. Matsui (1996). Observer based nonliner friction compensation in servo drive system. *Int. Workshop on Advanced Motion Control-AMC*, vol. 1, pp. 344-348.

Iwasaki, M., T. Shibata, N. Matsui (1999). Disturbance observer-based nonlinear friction compensation in table drive system. *IEEE/ASME Trans. on Mechatronics*, vol. 4, no. 1, pp.3-8

Kawamura, A., H. Itoh, and K. Sakamoto (1994). Chattering reduction of disturbance observer based sliding mode control. *IEEE Trans. on Ind. Appl.*, vol. 30, no. 2, pp. 456-461.

Lee, H.S. and M. Tomizuka (1996). Robust motion controller design for high-accuracy positioning systems. *IEEE Trans. Ind. Electr.*, vol. 43, no. 1, pp. 48-55.

Liu, Y. and Handroos, H. (1999). Sliding mode control for a class of hydraulic position servo. *Mechatronics*, vol. 9, pp.111-123.

Ohnishi, K. (1987). A new servo method in mechatronics. *Trans. Japanese Society of Electrical Engineers*, vol. 107-D, pp. 83-86.

Ro, P. I., Shim, W., and Jeong, S. (2000). Robust friction compensation for submicrometer positioning and tracking for a ball screw driven slide system", **Precision Engineering**, Jour. of the Int'l societies for Precision Engineers and Nanotechnology, Vol. 24, No.2, pp 160-173

Ro, P.I. and P. I. Hubbel (1993). Model reference adaptive control of dual-mode micro/macro dynamics of ball screws for nanometer motion. *ASME J. Dyn. Sys. Meas. Contr.*, vol. 115, pp. 103-108.

Slotine, J.-J.E. and W. Li (1991). *Applied Nonlinear Control*, Prentice Hall.

Laminar Flow Actuation on Ultraprecision Stage Positioning

Hsueh-chieh Wu* and Daniel B. DeBra**
*Western Digital Corporation, San Jose, CA95138 and
**Stanford University, Stanford, CA94305

Key word: Quiet Hydraulics, Laminar Flow Actuation, Precision Stage Positioning

Introduction

Laminar flow actuation is a preferred method in Quiet Hydraulics. Quiet Hydraulics has several advantages in ultraprecision machine design. In ultraprecision machine design, every engineer has to face two main challenges. One is thermal stability and the other is vibration. For instance, temperature variation of 1 milli-degree C can easily lead to 10 nm dimensional changes for a machine larger than 1 m. Vibration is also one of the major factors that determine the precision of a machine. The most efficient temperature control for any machine tool is through liquid showering, which maintains temperature stability at least an order of magnitude better than any other means. Hydraulic components are the easiest to integrate with liquid showering system. However the turbulence in most orifice-restricted hydraulic components creates a potential source of vibration. Therefore we applied the quiet hydraulics principles to design hydraulic systems with low Reynolds number to assure laminar flow operation conditions.

At the Stanford Quiet Hydraulics Lab, we have successfully integrated a laminar flow flapper valve into our quiet hydraulics testbed as the actuation means of the carriages. The overall integration results showed the standard deviation of the carriage positioning is 11.7 nm. In this presentation, we will focus on the laminar flow actuation system. The laminar flow actuation system includes a customized laminar flow flapper valve, a newly designed manifold, and a stictionless piston. A mathematical model of the laminar flapper valve is proposed. From the model we can investigate the properties of laminar flow flapper valves. The differences between the model and the experimental data are discussed in detail. Although we had modeled the laminar flow valve at component level, system integration result showed the model is neither too complicated for the controller design nor oversimplified to leave out important dynamics.

Despite the fact that almost all hydraulic components have nonlinear dynamics, because of the way we design the actuation system, the overall system including the laminar flow actuation actually showed very little nonlinearity. We can close the control loop with a simple linear controller design. The results show that the laminar flow actuation has wide dynamic range, low disturbance. It is a very good candidate for ultraprecision actuation.

Laminar Flow Actuation

At the Stanford Quiet Hydraulics lab, we have developed an ultraprecision diamond turning machine as a testbed to implement precision engineering principles. The Quiet Hydraulics testbed has two carriages for tool post and spindle motor. Each carriage adopts Kraakman way design with built-in provision for straightness and yaw correction. Therefore, the carriage positioning system can assume a straight traveling path. In order to be free from stiction from the seals, we

have the hydraulic fluid run in open loop. By controlling the temperature of the fluid, the overall system is thermally stable, and the fluid can also take away heat generated from the inefficiency of hydraulic components.

The main components of the carriage positioning system are a laminar flow valve, a flow manifold, and a piston with hydrostatic bearings. The actuator we chose is a laminar flow flapper valve modified by Woodward HSC from one of their three-way flapper valves. The fundamental differences between most hydraulic valves and a laminar flow valve are the efficiency and the temperature sensitivity. Most hydraulic valve designs would minimize the viscous loss to increase their efficiency, therefore, they are designed to be operated in turbulent flow region with internal orifices to regulate the flow and sharp edges at the flapper area to induce turbulence. Because of the turbulent flow, the dependence on the viscosity of the fluid is reduced. Since viscosity of fluid is a function of temperature, by reducing the effect of viscosity, a turbulent flow valve can be more robust to environmental changes. However, in ultraprecision applications, the power consumption is not a concern but the precision is. With tight control on the liquid temperature, a laminar flow flapper valve that eliminates the possible vibration source from the turbulence of the liquid flow is a much better candidate for higher precision applications. The basic difference in design between an ordinary flapper valve and a laminar flow flapper valve is shown in figure 1.

Generally, the laminar flow at the flapper area can be characterized by the following equation,

$$R = \frac{\Delta p}{q} = \frac{6\mu \ln(D_o/d_i)}{\pi h^3} \tag{1}$$

where R is the flow resistance defined by the pressure difference, Δp, divided by the flow rate, q, μ is the viscosity of the fluid, D_o and d_i are the outer and inner diameter of the nozzle tubes, and h is the gap between the flapper to the nozzle. For laminar flow, the flow rate of the valve is proportional to the pressure drop, as we observed in figure 2. However, in experiments, we did not see the resistance change of the flapper valve varies as inverse proportional to h cubed. That is due to the viscous loss in the flow passages inside the valve is no longer negligible. The effective resistance of the valve will be,

$$R = R_p + (h_0/h)^3 R_0 \tag{2}$$

where R_p is the passage resistance, h_0 is the gap of flapper valve at the neutral position and the corresponding flapper resistance is R_0. If we define,

$$k = R_p/R_0 \tag{3}$$

we can have a better description of the resistance changes with command input shown in figure 3.

The model of flapper valve is further proven valid with the integral results done at system level. The physical model of the carriage positioning system is shown in figure 4. With the mathematical model of the flapper valve, we can simulate the open loop response. In figure 5, the comparison of the simulated response and the experimental data is presented. Note that the resonance at around 18 Hz is the structural resonance determined by the linkage stiffness.

The laminar flow flapper valve shows very good linearity. Therefore we can close the positioning loop with a simple controller design. A PID+Notch controller is employed. Figure 6 shows the step response of the closed-loop stage positioning system.

Discussion

There are several factors limiting the precision of stage positioning. The quiet hydraulics testbed has a wide dynamic range. The total travel is about 15 cm, while the precision target is at nanometer level. There are not a lot of sensors that can cover such a big dynamic range. The sensor output format also seems easier if we use A-quad-B signal. In this application, we have the choice of using A-quad-B, 32-bit digital words, or communication from PC's ISA bus. At the time of application, the A-quad-B signal is most ready to implement, as long as the controller allocates enough memory for decoder. But using A-quad-B signal prevents us using the finest resolution of the sensor, which is 0.3 nm. For this research the sensor resolution is about 5 nm.

The other limitation comes from the linkage stiffness. In this research, the mechanical design of the linkage is not optimized for its performance. A linear force transmission mechanism is a more important concern. Thus, limited by the structural stiffness at 18 Hz, we only tried to close the positioning loop at 4 Hz. From the steady-state error spectrum, we can see that the noise less than 20 Hz has great contribution to the overall noise level. Once the bandwidth is increase the precision of the stage positioning should improve.

The previous two effects are not hard to mend. We can upgrade the machine tool controller so that it can be installed in a stand-alone chassis with proper electric shield to reduce line noise. Furthermore we can upgrade the input interface of the machine tool controller to take 32-bit digital words directly from the sensor, we can both increase the loop update rate and sensor resolution. Thus, we can reduce the quantization error. We can also increase the bandwidth of the system by modifying the linkage design or modifying the controller. Therefore, the low frequency components of the error will be greatly reduced.

From the integration result, we are very confident about the laminar flow actuation in the applications of ultraprecision machines.

Reference

Chen, C. and DeBra, D.B., 1987 "A Laminar Flow Motor for Precision Machining", Annuals of the CIRP Vol. 36, No. 1. pp.385-390.
DeBra, D.B. and Peirce, S.B., 1993 "Quieter Than a Wet Whistle", Advances in Aerospace Sciences: A Tribute to Holt Ashley, Stanford University, pp.93-101.
DeBra, D.B., 1994 "Quiet Hydraulics", Proceedings of ASPE, Annual Meeting, Cincinnati, OH.
Huang, J-J. and DeBra, D.B., 1997 "Liquid Temperature Control for a Hydraulic Turning Machine", IEEE Control Systems, Aug., pp56-63.
Peirce, S.B. and DeBra, D.B., 1994, "Quiet Hydraulics for Ultraprecision Actuation", ASPE Spring Topical Meeting on Mechanism and Controls for Ultraprecision Motion, Tucson, AZ, pp.84-87.

Wu, H-C., 2000, 'Ultra-precision Carriage positioning of a Quiet Hydraulics Testbed', Ph.D. Dissertation, Stanford University, November.

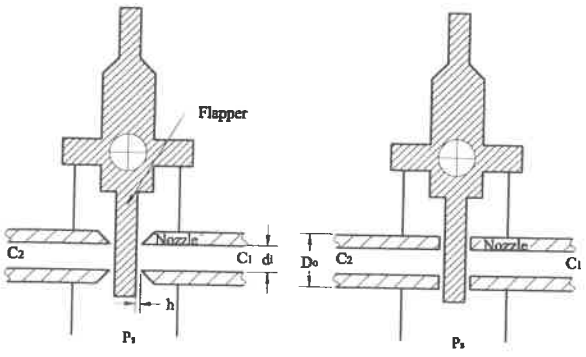

Figure 1. Turbulence flow flapper valve design vs. laminar flow flapper valve design

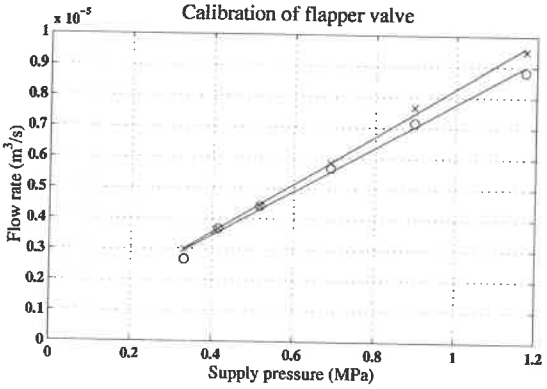

Figure 2. Nominal resistance of a laminar flow flapper valve

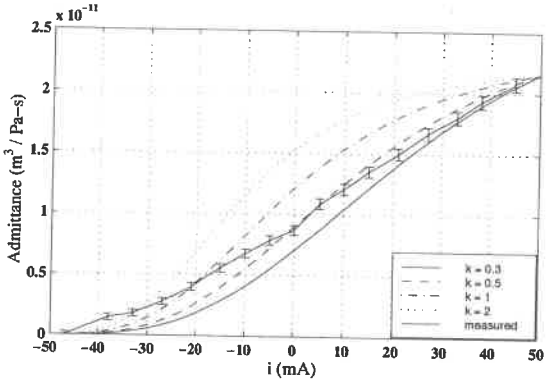

Figure 3. Effective admittance of the laminar flow flapper valve. Only one port is shown.

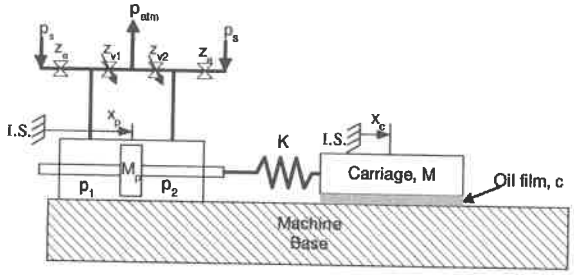

Figure 4. Stage positioning system

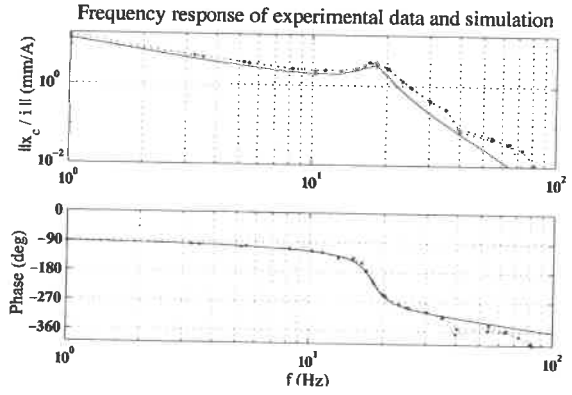

Figure 5. Open loop response of stage positioning system, simulation and experimental data

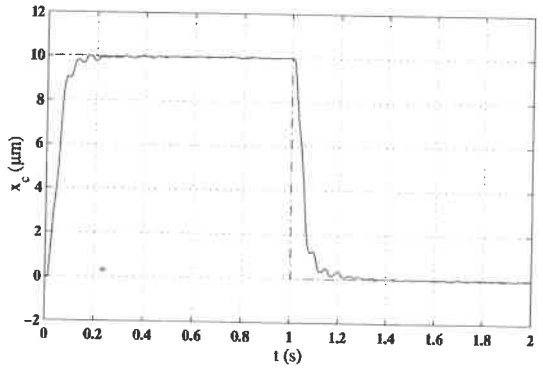

Figure 6. Step response of stage motion

Development of a High Bandwidth, High Power Linear Amplifier for a Precision Fast Tool Servo System

S. Rakuff[1], J. Cuttino[1], D. Schinstock[2]

[1]Dept. of Mechanical Engineering, The University of North Carolina at Charlotte, Charlotte, NC 28223
[2]Dept. of Mechanical Engineering, Tulsa University, Tulsa, OK 74104

1. Introduction

A "long-range" fast tool servo (FTS) has been developed at UNC-Charlotte that is currently able to deliver ±1mm linear motions at frequencies as high as 50 Hz. To date the accuracy is 0.1 μm for a ±250μm sinusoidal oscillatory motion at 20Hz. The FTS consists of a DSP-system, a voice coil driven flexure carrying the diamond cutting tool, and a laser interferometer, which is used for position feedback. A PID algorithm running on the DSP card is used for position control. The controller signal is amplified with a high performance analog amplifier to drive the voice coil.

The high power output and bandwidth requirements of the amplifier mean that it must be a carefully designed, integral part of the FTS system. The amplifier in this paper features the APEX PA03 linear operational amplifier. The paper describes the design techniques applied during development of the amplifier circuit and points out how classical control techniques can be used.

2. Design objective

The amplifier is designed to operate in a frequency span from DC up to 50Hz. This distinguishes the amplifier from commercially available audio amplifiers, which are typically designed as band pass filters. A requirement for the FTS was to be able to hold the flexure at a commanded fixed position with a constant force, which corresponds to a nominally constant current through the voice coil. However, typical signal frequencies will lie around40 Hz, which is close to the fundamental frequency of the flexure. Operating the system close to its natural frequency helps to conserve power but is also harder to control.

Because of the low pass filter characteristics of the amplifier, design techniques from classical controls may be optimally applied in the design process. In its simplest form, the voice coil can be modeled as a resistor in series with an inductance. This gives a transfer function between the load current and the load voltage of

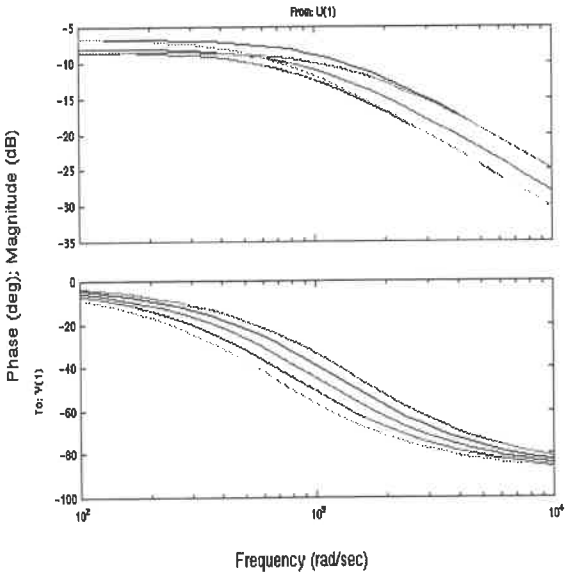

Figure 1: Frequency response of the voice coil

$$TF = \frac{I_L}{V} = \frac{1}{Ls + R_L} \tag{1}$$

where L=2.5mH ± 30% and R_L=2.4Ω ± 12.5% taken from the data sheet of the voice coil. Figure 1 shows the Bode plots of the voice coil for L and R varying within their uncertainties. The –3dB bandwidth is only about 1000rad/s (159Hz), which would also be the bandwidth of an open loop amplifier configuration. The bandwidth can be increased if a properly designed controller and feedback network is implemented.

3. Voltage controlled current sources

The amplifier is designed as a voltage controlled current source or VCCS. The amplifier converts the position command voltage from the DSP card into a current flow I_L through the voice coil to move the flexure. The voltage to current conversion factor is set to 2.2A/V. The voice coil is assumed to behave like an ideal actuator having a linear realationship betweenthe current and the output force. The force constant is

$$K_f = 21.3\frac{N}{A} \tag{2}$$

To generate a sinusoid force with an amplitude of 100N at a frequency of f=50Hz (ω=314.2rad/s), the required current amplitude I_L is 4.68A. From figure 2 it can be seen that the voltage across the load impedance R_L and L_L is the difference between v_L and v_S. If the feedback resistor R_f is large compared to the sense resistor R_S, then it can be assumed that all current flowing through the load will eventually flow to ground so that i_L is approximately equal to i_S. The voltage drop accross the load can then be written as

$$v_L \cong L\frac{di_L}{dt} + (R_L + R_S)i_L \tag{3}$$

where

$$\frac{d}{dt}i_L(t) = -\omega I_L \sin(\omega t) \tag{4}$$

The magnitude of di_L/dt is maximized at times $t = 0,\ \pi\omega,\ 2\pi\omega$, and so forth. The magnitude of the voltage is about 12V. As shown in figure 3, the voltage will lead the current by a phase angle ϕ.

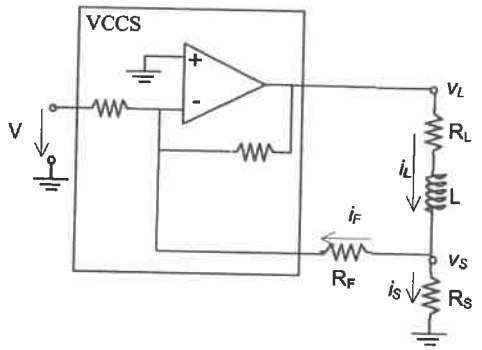

Figure 2: Voltage controlled current source (VCCS)

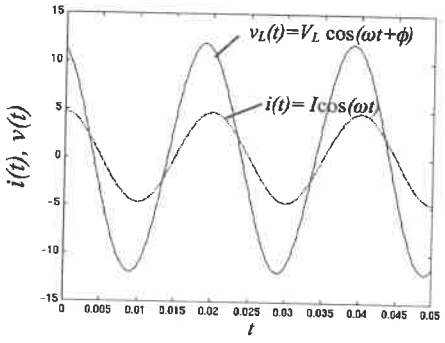

Figure 3: Current voltage relationship

If the frequency of the current increases, so does the magnitude of the phase angle. The varying phase angle between load voltage and load current does not affect the PID position controller of the FTS system because the load current is directly proportional to the force exerted by the voice coil and normally in phase with the controller signal going into the amplifier.

In equation (3) v_L consists of the inductive voltage drop and the voltage drop across the resistors R_L and R_S. At 50Hz the load is still more resistive than inductive and the phase shift is relatively small. The power dissipation in the load with small or zero phase angle is calculated by

$$\begin{aligned} P &= V_{L,rms} I_{rms} \cos(\phi) \\ &= \frac{V_L I}{2}\cos(\phi) = \frac{12V \cdot 4.68A}{2}\cos(0) = 28W \end{aligned} \tag{5}$$

where $V_{L,rms}$ and I_{rms} are the root mean square values of the load voltage and load current respectively. This amount is also a ballpark value for specifying the power supplies needed.

4. Sensitivity of the amplifier due to modeling errors

A good amplifier design should be relatively insensitive and robust to parameter variations. The resistance R_L and the inductance L of the load have high uncertainties of $\pm$10 and $\pm$30 percent respectively and the gains introduced by the op amps may change some when the system ages. These parameter variations can be modeled as

unstructured additive uncertainties. Another source of errors arises from unmodeled plant dynamics. If ΔG denotes the difference between the actual plant G and the nominal modeled plant G^* then

$$G(s) = G^*(s) + \Delta G(s) \tag{6}$$

Figure 4 shows a simple open loop amplifier with a proportional controller $K(s)$, input voltage $V(s)$ and output current $I_L(s)$. The plant $G(s)$ represents the voice coil and amplification gains of the amplifier. In the open loop configuration, the percentage error of the load current equals the percentage error of the model.

$$\frac{\Delta I_L(s)}{I_L^*(s)} = \frac{\Delta G(s)}{G^*(s)} \tag{7}$$

Equation (7) shows how sensitive the open-loop configuration is to modeling errors alone. If the modeling error is appreciable the resulting system output error might be unacceptably high. If information about I_L is fed back through a feedback gain H into the input terminal of the amplifier as indicated in figure 5, then the relationship between percentage output error and percentage modeling error is expressed by

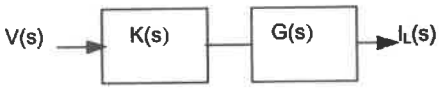

Figure 4: Open loop amplifier

$$\frac{\Delta I_L(s)}{I_L^*(s)} = \frac{1}{1 + H(s)G(s)K(s)} \cdot \frac{\Delta G(s)}{G^*(s)} \tag{8}$$

If the return difference $1+HGK$ were large, then a significant percentage error in modeling the plant would result only in a small percentage error in the output. Therefore, it is desired to maximize HGK in equation (8). It can be seen that with a feedback network installed command following is less sensitive to modeling errors.

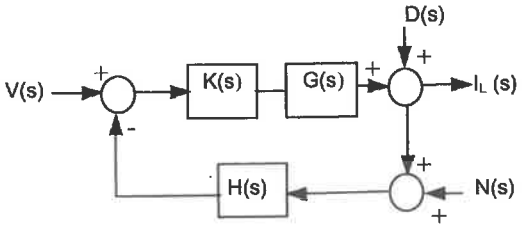

Figure 5: Closed loop amplifier with disturbance and noise

5. Disturbance rejection and noise response of the amplifier

The amplifier also has to be insensitive to internal noise N and compensate for external disturbances D as shown in figure 5. The expected disturbances are assumed to be low frequency signals representing mechanical input into the tool. Noise is generated in the circuit and is usually of high frequency. The output current I_L can be expressed in terms of input V, internal signal noise N, and external disturbances D by

$$I_L(s) = \frac{G(S)K(s)}{1 + H(s)G(s)K(s)} V(s) - \frac{H(s)G(s)K(s)}{1 + H(s)G(s)K(s)} N(s) + \frac{1}{1 + H(s)G(s)K(s)} D(s) \tag{9}$$

To investigate the influence of disturbances D on the amplifier assume that noise N and input V equal zero. Then I_L is related to D by

$$I_L(s) = \frac{1}{1 + H(s)G(s)K(s)} D(s) \tag{10}$$

For good disturbance rejection, the output I_L in equation (10) should be close to zero since the input V was assumed to be zero. This implies that the return difference $1+HGK$ has to be large at lower frequencies where the disturbances have their major energy content.

To analyze the effects of noise, assume that the disturbances D and the input voltage V are zero. From equation (9) the load current then equals

$$I_L(s) = -\frac{H(s)G(s)K(s)}{1 + H(s)G(s)K(s)} N(s) \tag{11}$$

Again, for good noise immunity the output I_L in equation (11) should be close to zero because the input was assumed to be zero. Since noise N is a signal with energy contents at high frequencies, the transfer function HGK has to be small at higher frequencies. Thus, the open-loop frequency response of the op amps used to build the amplifier should look like a low pass filter with high gain at low frequency and low gain at high frequency. Output

feedback in the amplifier is important to reduce the effects of noise and modeling errors as well as to increase command following properties.

6. Designing an integrator-type feedback controller

The amplifier's bandwidth is required to be higher than the open loop bandwidth of 160Hz determined by the voice coil. Two cascaded feedback networks are used to enhance the frequency response of the amplifier. A circuit diagram is given in figure6 and represented in block diagram form in figure7. The block diagram contains several transfer function blocks, which correspond to elements in the amplifier circuit. Table 1 summarizes the transfer functions of the various elements with a brief description.

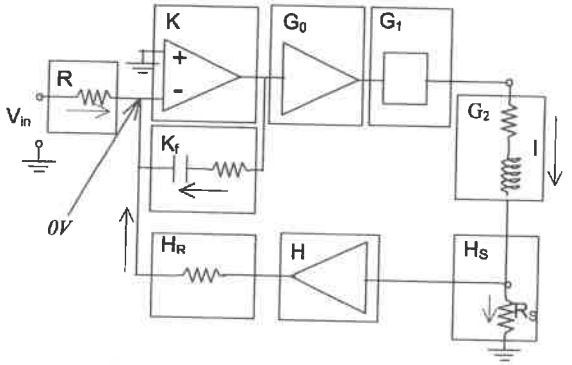

Figure 6: Circuit diagram divided up into TF blocks

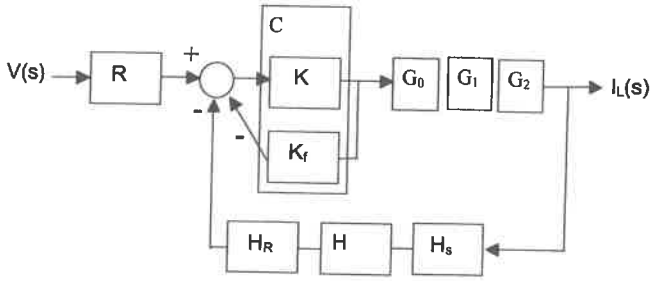

Figure 7: Block diagram representation of amplifier

Table 1: Transfer functions of various elements in the amplifier circuit

Name	Transfer function	Units	Description
R	$\frac{I_o}{V_i}=\frac{1}{5100}$	$\frac{A}{V}$	Input resistor of 5.1kΩ
K_{ol}	$\frac{V_o}{V_i}=\frac{76dB\cdot 12kHz}{s+12kHz}=\frac{6310\cdot 75400}{s+75400}$	$\frac{V}{V}$	Open loop TF of power op amp used to build the controller (AD826). Open loop response taken from data sheet.
G_0	$\frac{V_o}{V_i}=\frac{1.6\cdot 12kHz}{s+12kHz}=\frac{1.6\cdot 75400}{s+75400}$	$\frac{V}{V}$	Close loop TF of power op amp AD826 set to a gain of 1.6
G_1	$\frac{V_o}{V_i}=\frac{7.5\cdot 800000}{s+800000}$	$\frac{V}{V}$	Closed loop TF of power op amp PA03 set to a gain of 7.5
G_2	$\frac{I_L}{V_L}=\frac{1}{Ls+R}=\frac{1}{0.0025s+2.4}$	$\frac{A}{V}$	TF of the load (voice coil)
K_f	$\frac{I_o}{V_i}=\frac{1}{R+\frac{1}{Cs}}=\frac{Cs}{RCs+1}$	$\frac{A}{V}$	TF of the inner feedback path. The values of R and C are to be determined by tuning the controller
H_R	$\frac{I_o}{V_i}=\frac{1}{5100}$	$\frac{A}{V}$	Resistor of 5.1kΩ in the outer feedback path after op amp
H	$\frac{V_o}{V_i}=\frac{20.8\cdot 12kHz}{s+12kHz}=\frac{20.8\cdot 75400}{s+75400}$	$\frac{V}{V}$	Gain introduced by an op amp (AD826) in the outer feedback path set to a gain of 20.8
H_S	$\frac{V_o}{I_L}=0.02$	$\frac{V}{A}$	Sense resistor of 0.02Ω to convert the load current into a voltage

The closed loop frequency response G_1 and the open loop frequency response A_{POL} of the PA03 are shown in figure 8. G_1 has a pole at about 800000 rad/s. Since the gain is 7.5, the closed loop frequency response of the power op amp G_1 is

$$G_1=\frac{V_o}{V_i}=\frac{7.5\cdot 800000}{s+800000} \tag{12}$$

The open loop response of the AD826 is obtained the same way by noting that the open loop gain given in the data sheet is 76dB with a bandwidth of 12kHz. Hence, the open loop response can be expressed as

$$K_{ol} = \frac{V_o}{V_i} = \frac{76dB \cdot 12kHz}{s + 12kHz} = \frac{6310 \cdot 75400}{s + 75400} \qquad (13)$$

These fast poles of the op amps could be neglected in the calculations and K_{ol} set to 6310V/V. R, H_s, and H_R are resistors that convert voltages into currents in the block diagram representation. At the summing point all currents sum to zero according to Kirchhoff's current law.

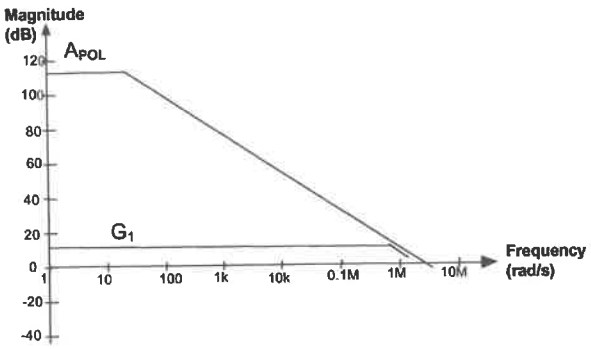

Figure 8: Open and closed loop response of the PA03

K and K_f in figure 7 can be combined to an equivalent block C containing a strictly proper third order transfer function. By selecting values for the resistor and capacitor contained in block K_f the amplifier can be tuned. The equivalent transfer function can be used to simulate the frequency response of the amplifier for different values of the capacitor and resistor in the integral-type feedback controller. Figure 9 shows an array of Bode plots for a constant capacitance of 0F and R ranging from 5kΩ to 500kΩ.

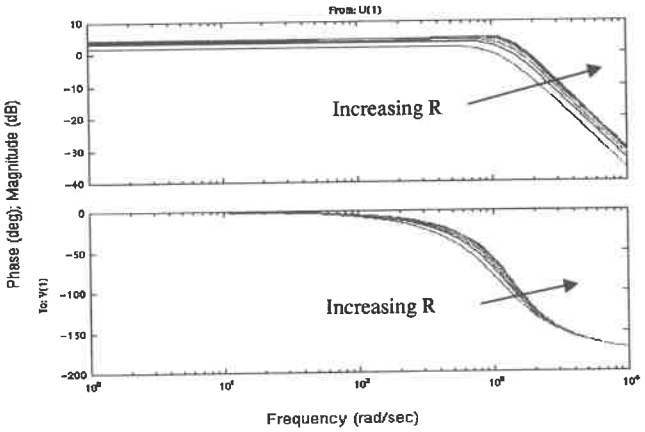

Figure 9: Response of the model for increasing R and C=0

7. Frequency response measurements of the amplifier

The actual frequency response of the amplifier with no integral gain was measured with a signal analyzer. The frequency response was computed by dividing the cross spectrum between the input signal sequence and the output signal sequence by the power series spectrum of the input signal sequence. Therefore, the frequency response is a direct representation of the characteristics of the true system.

Figure 10 shows the frequency response of the amplifier/voice coil assembly resulting from a sinusoidal input voltage with amplitude 0.5V. Unfortunately, the maximum frequency of the measurements was limited by the bandwidth of the current probe that was used to measure the output of the amplifier.

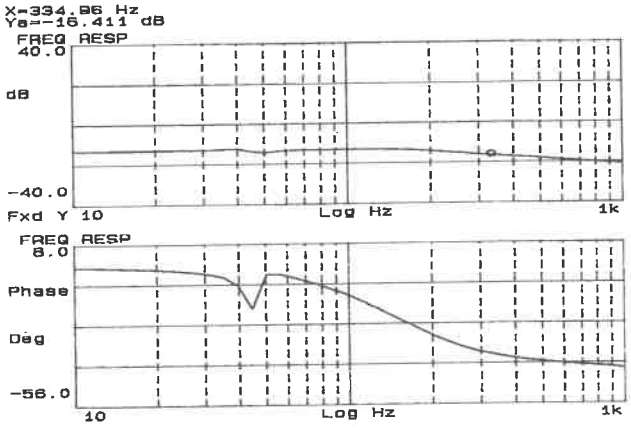

Figure 10: Frequency response of actual amplifie

There are still some discrepancies between the experimental and the theoretical models. Figure 10 shows some dynamics in the real system that have not yet been identified. For example, the dynamics at 48Hz are apparently caused by the first mode of the flexure that is attached to the voice coil. The bode plot shows the presence of multiple poles and zeros interacting with each other, as evidenced by the dip at 45 Hz, rise shortly thereafter (indicating a pole/zero pair), followed by a gentle –10 db/decade slope that begins to roll off further at 1 kHz. It is believed that the response will reach a –40 db/decade slope and –180 degree phase beyond 1 kHz, but the discrepancies are still being investigated.

8. Non-linearities

During the process of tuning the PID controller for the FTS system, the amplifier sometimes saturated because of very large and fast controller output signals. This means that the FTS system represents a difficult non linear system. One possibility to describe nonlinearities is to fit a higher order linear transfer function to nonlinear frequency response data about some operating point. These transfer functions may be used to design the PID controller for the FTS system.

Matlab and Simulink were used to create an amplifier model (figure 11) that contains slew rate limits, saturation blocks, and back-emf (figure 12). The back-emf subsystem calculates the velocity of the flexure by differentiation of the displacement and a constant relationship between velocityand back-emf voltage generated. Virtual test inputs equivalent to those from the signal analyzerwere fed into the model to calculate the frequency response in the linear region. Efforts are currently under way to verify the model.

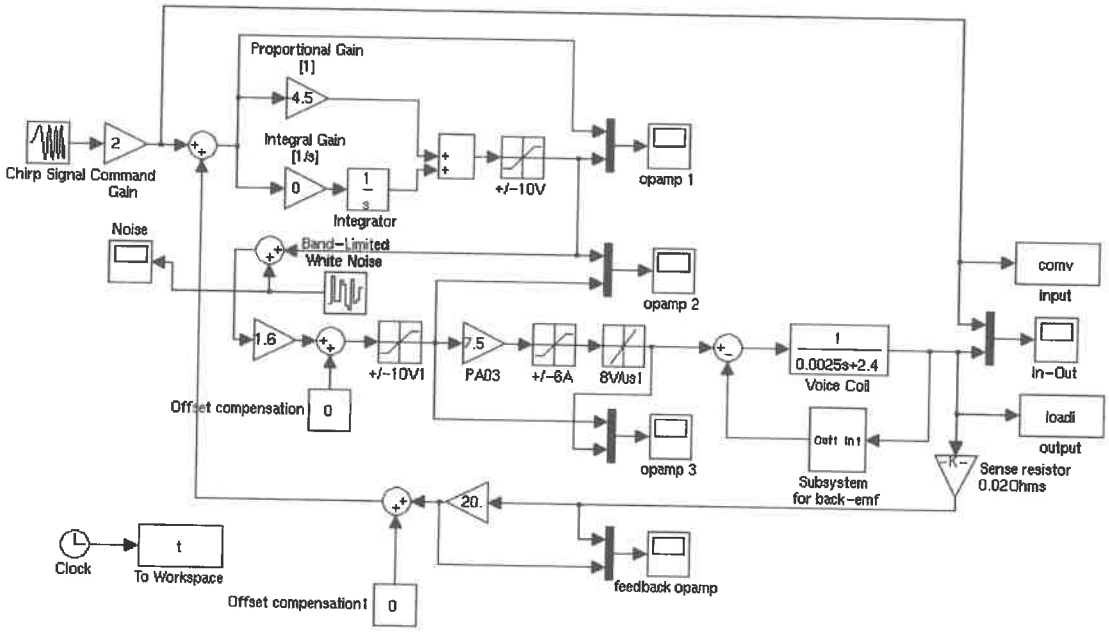

Figure 11: Simulink block diagram of actual amplifier

9. Conclusion

This work shows how techniques from classical control theory can be applied to design and analyze the performance of an amplifier for a precision motion mechanism utilizing a voice coilIt also points out many of the difficulties in getting the theory to accurately model the actual response. Work is continuing to identify the principal components required to develop accurate models of amplifiers used for precision applications.

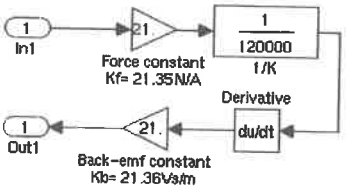

Figure 12: Back-emf subsystem for mode

10. References

1. Zia A. Yamayee, Juan L. Bala, Jr., 'Electromechanical Energy Devices and Power Systems", John Wiley & Sons, Inc., 1994
2. Richard C. Dorf, Robert H. Bishop, "Modern Control Systems", 7th edition, Addison Wesley, 1995
3. APEX Microtechnology catalog v8.5, Application notes, 1999
4. WilliamJ. Palm III, "Modeling, Analysis, and Control of Dynamic Systems", 2nd edition, John Wiley and sons, Inc

Repetitive Control of a Rotary Fast Tool Servo

Joseph A. Calzaretta

Stephen J. Ludwick

Marten F. Byl

David L. Trumper

Massachusetts Institute of Technology
Cambridge, MA 02139

1 Introduction

We have built a prototype diamond turning machine, intended for the production of rotationally asymmetric spectacle lenses. The peak-to-peak amplitude of the asymmetric features can be as much as 1 cm at the outside of the part. While tracing such a part at 1200 RPM, accelerations at the tool tip exceed 300 m/s^2. In order to meet the accuracy requirements of the spectacle lens industry, the tool tip must follow this path with errors of less than 1 μm. Our prototype machine features a rotary fast tool servo axis, designed to achieve accelerations of up to 500 m/s^2.

The prototype 3DOF diamond turning machine is shown schematically in cross-section in Figure 1, and in a photograph in Figure 2. As shown on the right side of Figure 1, the machine includes a conventional cross-feed slideway and spindle, which carry the workpiece (lens). Both the spindle and cross-slide are air-bearing systems. The cross-slide is driven by a linear motor. The novel aspect of our machine is the rotary fast-tool servo, shown in the left side of Figure 1. The rotary configuration results in an inertia ratio between the tool axis and machine base on the order of 10^{-5} compared to 10^{-2} for conventional diamond turning machines. The design of this machine is presented in detail in [2] and [4].

Since the tracking performance requirements are so strict, we cannot tolerate significant errors at harmonics of the spindle frequency due to peri-

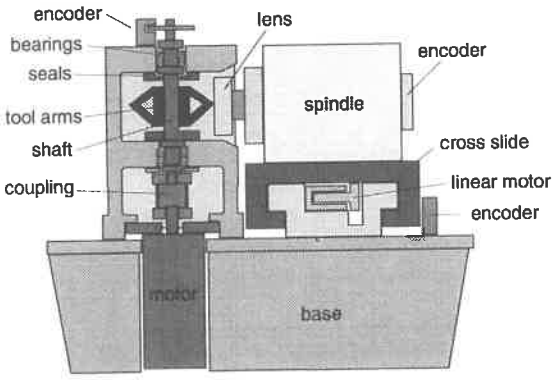

Figure 1: Schematic cross-section of the prototype spectacle lens turning machine using the rotary fast tool servo design.

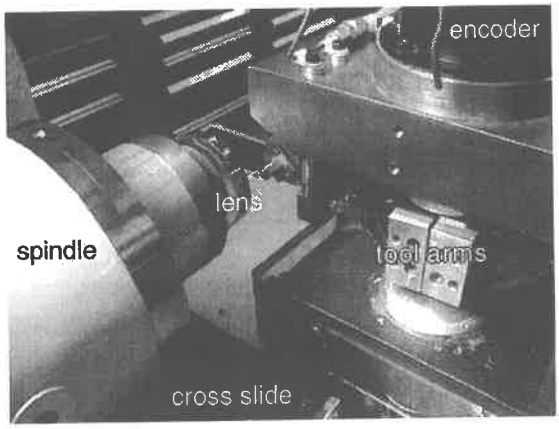

Figure 2: Photograph of the prototype spectacle lens turning machine.

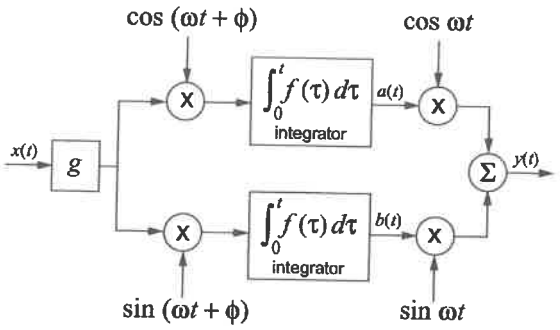

Figure 3: Basic AFC controller.

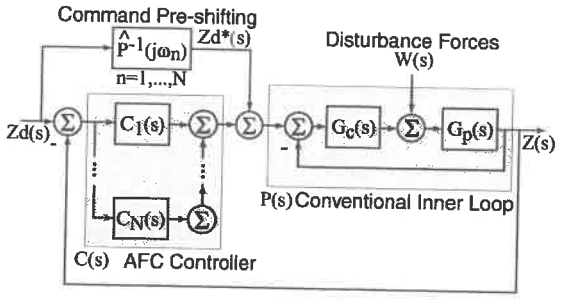

Figure 4: Overall control system design for the fast tool servo.

odic disturbances such as cutting forces and plant model uncertainty. The controller we developed attempts to null these periodic disturbances with a form of repetitive control known as Adaptive Feedforward Cancellation (AFC), see [3]. This algorithm places resonators at the frequencies of interest ω_n. The canonical form of such a resonator is depicted in Figure 3; however, it can be shown that the entire resonator is an LTI system of the form

$$\frac{Y(s)}{X(s)} = g\frac{s\cos\phi + \omega\sin\phi}{s^2+\omega^2}, \qquad (1)$$

where gains g_n and phase advance parameters ϕ_n are constants to be determined for each value of n.

This control scheme, with an appropriate choice of phase advance parameters and gains can errors greatly in the presence of constant-amplitude sinusoidal disturbances. The selection of phase advance parameters ϕ_n have been shown to have optimal values as shown in [2], but no corresponding values for the gains g_n has been detailed. We will present a heuristic method for tuning the gains based on error criteria and desired gain margin.

The entire control system for our machine is pictured in Figure 4. The controller consist of three components, a conventional lead-lag inner-loop controller, a command pre-shifting feedforward path, and a multi-resonator AFC control block. Figure 5 shows the closed-loop frequency response of the conventional system. For our rotary fast-tool servo machining sinusiodal asymetric lenses in polycarbonate, system errors are 20%

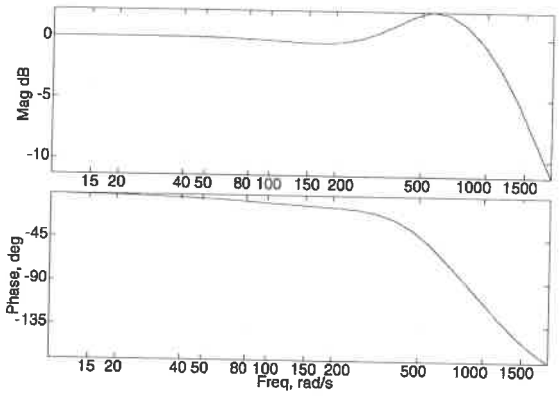

Figure 5: An example inner-loop plant frequency response $P(j\omega)$ from the diamond-turning machine.

with only the inner-loop controller, 1.2% combining command pre-shifting with the inner-loop control, and 0.1% with all three control blocks. Figure 6 shows the tool path error during a sinusoidal air-cut at 20 Hz under conventional control. Figure 7 shows the tool path error during the same sinusoidal air-cut at 20 Hz under conventional control with the addition of a single AFC resonator at 20 Hz. The addition of the AFC resonator drops the error from 20% to 0.003%. The design of the lead-lag inner-loop controller and command pre-shifting outer-loop are presented in detail in [2] and [4].

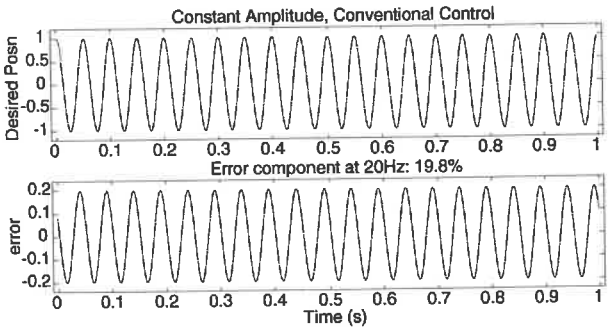

Figure 6: Tool path error to a constant-amplitude 20-Hz sinusoidal under conventional control only. Position is in mm.

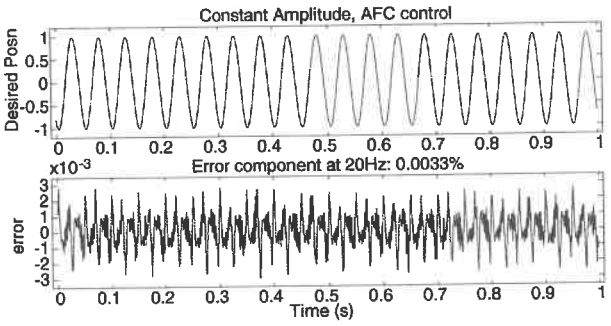

Figure 7: Error to a constant-amplitude 20-Hz sinusoidal toolpath under both standard AFC and conventional control. Position is in mm.

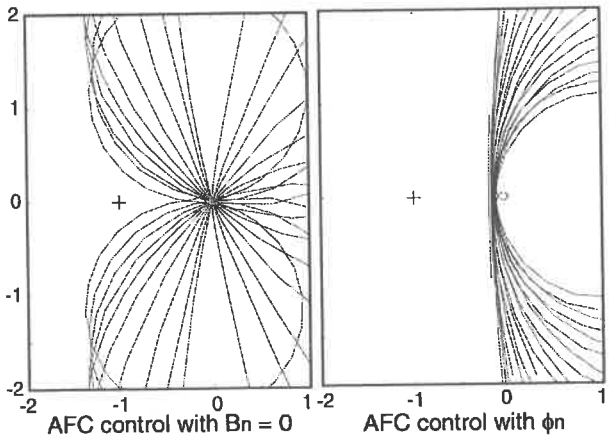

Figure 8: Nyquist diagrams of $C(s)P(s)$ for two different AFC controllers.

2 Choice of Phase Advance Parameter ϕ_n

The form of the AFC controller (1) contains only one resonator. A more general AFC controller can contain multiple resonators in parallel and may be expressed as:

$$\begin{aligned} C(s) &= \sum_{n=1}^{N} C_n(s), \\ C_n(s) &= \frac{A_n s + B_n}{s^2 + \omega_n^2}, \end{aligned} \tag{2}$$

where we have chosen A_n and B_n to be:

$$\begin{aligned} A_n &\equiv g_n \cos\phi_n \\ B_n &\equiv g_n \omega_n \sin\phi_n. \end{aligned} \tag{3}$$

Here ϕ_n is the phase advance independently specified for each resonator. It can be shown that for maximum phase margin, we should set $\phi_n \equiv \angle P(j\omega_n)$, where $\angle P(j\omega_n)$ is the phase of the plant at $j\omega_n$.

Figure 4 illustrates the control structure for a system with multiple resonators. The N AFC blocks $C_n(s)$ are combined in parallel to form $C(s)$, and act on the plant $P(s)$. Figure 8 depicts Nyquist diagrams for two different AFC controllers. The left half diagram represents a controller of the form (2) with $B_n = 0$ for each n, thus not taking into account the plant phase at each resonator frequency ($\phi_n = 0$). This system significantly penetrates the left half plane and exhibits a worst-case phase margin of 15°. The right diagram represents a controller where A_n and B_n have been determined using $\phi_n = \angle P(j\omega_n)$. This system exhibits a phase margin of 85°.

3 Choosing Gains g_n for N Parallel Resonators

We haved developed a heuristic method for selecting the gains, g_n, for N parallel resonators. Space precludes presenting the full details, but the method uses three principle steps to determine the

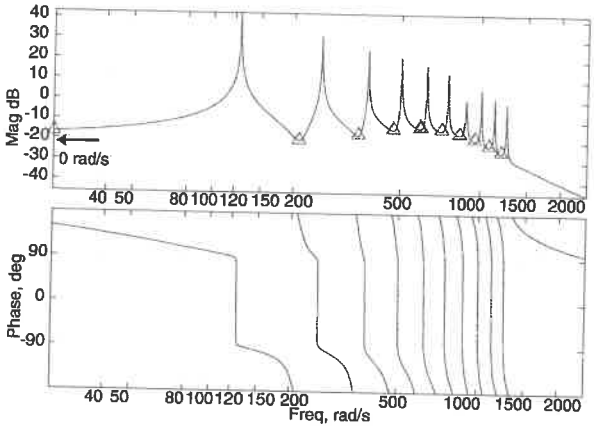

Figure 9: The negative of the AFC loop transmission $-L(j\omega)$ for the rotary fast-tool servo with 10 resonators.

system gains. First, we can determine the general magnitudes of the gains based upon the desired error at the principle disturbance frequency. Secondly, we scale the N resonator gains based on the magnitude of each frequency component of the repetitive disturbance relative to the magnitude of the principle disturbance frequency. Lastly, we scale the gains to achieve a desired system gain margin. Our heuristic method contains variables allowing us to fix system performance at specific resonators. The details of this method will be presented in the full paper now under preparation.

Figure 9 shows the negative of the AFC loop transmission for the rotary fast-tool servo system with a 10 resonator AFC control block. In addition to the heuristic method, we have developed some guidelines for hand tuning the system gains without calculating system error or designing to a desired gain margin. First, to avoid unstable systems, the magnitude of the local minima must be kept below 0 dB on the AFC negative loop transmission plot. Secondly, the error in the vicinity of each ω_n is inversely proportional to the corresponding g_n (i.e. the greater g_n, the smaller resulting error in the vicinity of ω_n). Lastly, the positions of the local minima can be partially tuned by varying the magnitudes of the surrounding maxima. The local minima will bias towards the lower magnitude peak. This rule breaks down at the higher order terms, where the local maxima and minima are close together on the log scale.

4 Conclusions

The heuristic method we have developed for choosing resonator gains has significantly simplified the process of selecting the gains for multi-resonator systems. The method allows the designer to minimize system errors while maintaining an acceptable gain margin. There are a number of weaknesses with this heuristic method, thus research is continuing to further simplify the gain selection process and to add features to more optimally follow disturbances with slowly varying amplitude. For machines performing periodic motions, AFC control is an essential and promising strategy for improving tracking performance.

References

[1] B. A. Francis and W. M. Wonham. The internal model principle of control theory. *Automatica*, volume 12, no. 5, pages 457–465, 1976.

[2] Stephen J. Ludwick. A rotary fast tool servo for diamond turning of asymmetric optics. Ph.D. Thesis, Department of Mechanical Engineering, Massachusetts Institute of Technology, Cambridge, MA, 1999.

[3] William Messner and Marc Bodson. Design of adaptive feedforward algorithms using internal model equivalence. *International Journal of Adaptive Control and Signal Processing*, 9:199–212, 1995.

[4] Joseph A. Calzaretta, Stephen J. Ludwick, Marten F. Byl, and David L. Trumper. Repetitive control of a fast-tool servo for asymmetric diamond turning. *Mechatronics*, 2000.

Author Index

Alamo, Brian J. . . . 23
Allen, Graham S. . . . 43
Andeen, Gerry B. . . . 23
Arelavo, Victor M. . . . 13
Byl, M.F. . . . 94
Calzaretta, J.A. . . . 94
Carlisle, Keith . . . 33
Cuttino, James F. . . . 88
DeBra, Daniel B. . . . 3, 43, 84
Dorn, Huck . . . 56
Gao, Yongsheng . . . 29
Hardham, Corwin T. . . . 43
Hill, Eric . . . 51
Homburg, F. G. A. . . . 72
Hopkins, David J. . . . 33, 71*
Howard, Lowell P. . . . 66
Hua, W. . . . 43
Jabben, Leon . . . 39
Jacobs, Roy H. R. . . . 66
Karpel, Mordechai . . . 56
Kraner, Emil . . . 55*
Lantz, Brian T. . . . 43
LeBrun, Thomas . . . 66
Liebman, Michael K. . . . 47
Ludwick, S. J. . . . 94
McCoy, John . . . 23
Molenaar, Alexander . . . 39
Moudgal, Vivek . . . 51
Nelson, Peter G. . . . 55*
Nichol, Jamie G. . . . 43
Overschie, Peter M. . . . 39
Pletner, Baruch . . . 56
Rakuff, Stefan . . . 88
Ro, Paul I. . . . 78
Schinstock, Dale E. . . . 62, 88
Seugling, Richard M. . . . 66
Shim, Wonbo . . . 78
Smith, Stuart T. . . . 17, 66
Trumper, David L. . . . 47, 94
Van Beek, H. Frank. . . . 39
Venugopal, Ravinder . . . 51
Wei, Zhouhong . . . 62
Wilson, Curtis S. . . . 9
Woody, Shane C. . . . 17
Wu, Hsueh-Chieh . . . 84
Wulff, Timm A. . . . 33
Yang, Pai-Hsueh. . . . 23
Yu, Chi Wai . . . 29
Zhang, Dawei . . . 29

* Extended abstract not available at printing.